HAL
open science

In-situ transmission electron microscopy studies of metal-Ge nanowire solid-state reactions

Khalil El Hajraoui

To cite this version:

Khalil El Hajraoui. In-situ transmission electron microscopy studies of metal-Ge nanowire solid-state reactions. Instrumentation and Detectors [physics.ins-det]. Université Grenoble Alpes, 2017. English. NNT : 2017GREAY012 . tel-01645553v2

HAL Id: tel-01645553

https://theses.hal.science/tel-01645553v2

Submitted on 12 Dec 2017

HAL is a multi-disciplinary open access archive for the deposit and dissemination of scientific research documents, whether they are published or not. The documents may come from teaching and research institutions in France or abroad, or from public or private research centers.

L'archive ouverte pluridisciplinaire **HAL**, est destinée au dépôt et à la diffusion de documents scientifiques de niveau recherche, publiés ou non, émanant des établissements d'enseignement et de recherche français ou étrangers, des laboratoires publics ou privés.

Communauté UNIVERSITÉ Grenoble Alpes

THÈSE

Pour obtenir le grade de

DOCTEUR DE la Communauté UNIVERSITÉ GRENOBLE ALPES

Spécialité : **Physique**

Arrêté ministériel : 25 Mai 2016

Présentée par

Khalil EL HAJRAOUI

Thèse dirigée par **Jean-Luc ROUVIÈRE**
et codirigée par **Martien DEN HERTOG**

préparée au sein **de l'Institut Néel - CNRS - Grenoble**
et de **l'Université Grenoble Alpes**

Études in-situ dans un microscope électronique en transmission des réactions à l'état solide entre métal et nanofil de Ge

Thèse soutenue publiquement le **17 Mars 2017**,
devant le jury composé de :

Monsieur Joël Cibert
Directeur de Recherches CNRS, Université Grenoble Alpes, Président
Monsieur Antonius T. J. van Helvoort
Professeur à Norwegian University of Science and Technology, Rapporteur
Monsieur Thierry Epicier
Directeur de Recherches CNRS, Université de Lyon, Rapporteur
Monsieur Martial Duchamp
Professeur Assistant à Nanyang Technological University, Examinateur

Contents

Acknowledgements vii

List of Figures ix

List of Tables xv

Abstract xvii

1 Introduction 1

2 Metal-Semiconductor Solid-State Reaction 5
- 2.1 Metal-Semiconductor Solid-State Reaction . . . 5
  - 2.1.1 Electrical Characterization of Metal-Semiconductor Contact . . 6
- 2.2 Copper-Germanium System . . . 8
  - 2.2.1 Phase diagram & Literature . . . 9
- 2.3 Aluminum-Germanium System . . . 12
  - 2.3.1 Phase diagram . . . 13
- 2.4 Platinum-Silicium System . . . 14
  - 2.4.1 Phase diagram . . . 14
  - 2.4.2 Pt-Si (NW) Solid-State Reaction . . . 14
  - 2.4.3 Conclusion . . . 16
- 2.5 Diffusion . . . 17
  - 2.5.1 Fick's Law . . . 17
  - 2.5.2 Thermodynamic description of diffusion . . . 19
  - 2.5.3 The Deal and Grove Model . . . 20
  - 2.5.4 Original Model . . . 20
  - 2.5.5 Application to Thin-films . . . 22
  - 2.5.6 Application to Nanowires . . . 23
  - 2.5.7 Model applied to NWs used in this Phd . . . 25

3 Samples 31
- 3.1 Nanowire Growth . . . 31
- 3.2 Sample Preparation . . . 32
  - 3.2.1 Membrane Fabrication . . . 33
  - 3.2.2 Optical Lithography of Large Contacts . . . 33

3.2.3 E-beam Lithography to Contact NWs 35

4 Electron Microscopy **39**
4.1 Transmission Electron Microscope 39
4.1.1 Principle Components of the Transmission Electron Microscope 41
4.2 Scanning Transmission Electron Microscopy 42
4.3 Electron Energy Dispersive X-ray Spectroscopy 43
4.3.1 X-ray Quantification Analysis 47

5 Experimental Setup **53**
5.1 Introduction 53
5.2 In-situ TEM Heating Setup 55
5.2.1 Uncalibrated Temperature Direct Joule Heating [H_a] 55
5.2.2 Calibrated Temperature Joule Heating [H_b] 56

6 TEM Study of Cu-Ge (NW) Solid-State Reaction **59**
6.1 In-situ Phase Propagation of Cu-Ge Nanowire System 59
6.2 Kinetic of Cu-Ge Phase Formation 60
6.2.1 Direct Joule Heating 61
6.2.2 Membrane-substrate Joule heating 63
6.2.3 Influence of the Cu-Ge interface on reaction initiation 65
6.3 Structural Analysis of the Germanide Phase 67
6.3.1 Nanobeam Electron Diffraction 68
6.3.2 Electron Diffraction Tomography 69
6.4 Chemical Analysis of The Germanide Phase 71
6.4.1 EDX Quantification and Modeling 71
6.5 Comparison of Both Joule heating Techniques and Heat Flow Simulations 74
6.5.1 Comsol Multiphysics Software 76
6.6 Discussion and Modeling 79
6.6.1 Kinetic study 79
6.6.1.1 Calculation exchanged Cu and Ge atoms 80
6.6.2 Interpretation of Diffusion model 81
6.6.2.1 Additional EDX analysis 83
6.6.3 Discussion 85
6.7 Conclusion 87

7 TEM Study of Al-Ge (NW) Solid-State Reaction **89**
7.1 In-situ Phase Propagation of The Al-Ge (NW) System 90
7.2 Kinetic study of the Al-Ge Exchange Reaction 90
7.2.1 Al-Ge (NW) at Low Temperature 90
7.2.2 Al-Ge (NW) at High Temperature 93
7.3 Structural Analysis of the Al-Ge (NW) System 96
7.3.1 Electron Diffraction 96
7.3.2 High Resolution Transmission Electron Microscopy 97
7.4 Chemical Analysis of The Al-Ge System 99

7.4.1 EDX Quantification and Modeling 99
7.5 Electrical Measurements on the Al/Ge/Al System 102
7.6 Discussion and Modeling 106
7.7 Outlook: Electrical potential of Al/Ge heterostructures 110
7.8 Conclusion 111

8 Conclusion **113**
8.1 The Cu-Ge system 114
8.2 The Al-Ge system 115
8.3 Outlook 117

9 Résumé en Français **119**
9.1 Plan Du Manuscrit 120

Bibliography **125**

Acknowledgements

As a final part in the PhD. writing exercise, I would like to thank all the people who helped and supported me during the last 3 years and half of my thesis. The prophet Mohammed (peace be on him) said : *He who does not thank people, does not thank Allah* (narrated by Ahmad and Tirmidhi).

First, I would like to express my sincere thanks to my supervisor Martien Den Hertog for her time and patience deployed during all these years teaching me all the different techniques and helping me obtain and understand the different results shown in this PhD. manuscrit. I thank my thesis director Jean Luc Rouviére for his help understanding all the experimental data and the physics behind them. I really appreciate his sense of criticism dealing with any scientific result, whether it was for a publication or a presentation, or a report obtained after an experiment.

I'm really lucky to have the opportunity to have you both as supervisors, I will never forget all your advices given to provide clear and sustained scientific work.

I would like also to thank Eric Robin for giving his time to analyze and discuss with me on the energy dispersive X-ray (EDX) data that helped to understand the different phenomena observed during our in-situ TEM experiments.

I'm also thankful to the microscopists in the Néel Institute : Christophe Lepoittevin, Holger Klein, and specially, Stéphanie Kodjikian for their help when using the transmission electron microscope, which need to be handled very gently (I got it Stéphanie).

I'm happy to acknowledge our collaborators in Austria Prof. Alois Lugstein and his group members : Clemens Zeiner, Florian Brunbauer, etc. For providing the Germanium nanowires and for their well fabricated devices used in this study. Moreover, I would like to thank them for the fruitful discussions that helped a lot to improve the fabrication process.

I would definitely not forget to thank Bruno Fernandez, Thierry Crozes, Jean-Francois Motte, and Thierry Fournier, who are members of the team Nanofab in the Institute that helped and taught me a lot of nano-fabrication techniques that allowed to achieve working samples presented in this manuscript.

I really appreciate the atmosphere in the Physique LUmiére Matiére (PLUM) department where I spent the last 3 years and half thanks to a lot of friendly and kind people. Before going through the names, I know for sure that I will forget to mention some names that helped or supported me during this period spent in the department. So please do not feel ignored, you were a great support! I'm very thankful to Serge Huant for his kind encouragement during the (my thesis) writing which helped

a lot in finishing this manuscript. I would like to thank Sabine Douillet for her help to solve the problems faced in the software used in my experiments. A special thanks to Alain Prat for his help in the simulation presented in this manuscrit. I want also to thank Pierre Bordet, Céline Darie, Marie Claire, Eric Mossang, and Nassira Boudjada for all your support and the interesting discussions that we had. I thank also Farid Fettar and Yves Joly for all the good moments spent in the cafeteria or in a football pitch (with Farid and Yves always shouting "Khalil lâche la balle" or "Khalil fait des passes"). Those were great moments.
Thanks to Elodie, Pauline, Christophe, and Cyril for the nice moments that we spent and all the activities that we shared (where I generally came late or where I didn't show up, I know I'm horrible). Thanks to the Team : Xueying Hai, Meriam Ben Khedim, and Justin Janneau, for all the good moments and the support that you guys provided when things didn't go well. I will never forget you guys. You are the best.
I would like to acknowledge all my wonderful friends, who I met here in Grenoble. The list is very long, you will know yourselves. Thanks to my family who came to help me managing all the defense preparation that helped a lot. Above all, I am eternally in debt to my parents who stand beside me during the hard moments (specially my mother) and for always believing in me and for their financial support that allows me to continue my studies abroad. If it wasn't for their unfailing love and support I couldn't have finished this long journey.

List of Figures

2.1 Illustration of the near-interface region of a metal-semiconductor junction, interaction with the metal causes electronic states to appear in the bandgap of the semiconductor: associated with these states is a charge neutrality level denoted by the green line. In general, the metal Fermi level will not be at the charge neutrality level and a local band bending can occur in the semiconductor to pin the Fermi level there. Adapted from [1]. 6
2.2 Schematic of a Field effect transistor (FET) based on a Ge nanowire with a germanide formed phases. 7
2.3 The Cu-Ge phase diagram.[2] 10
2.4 Copper structure with the respective (111) planes. 11
2.5 Illustration of both Cu_3Ge(hatched) and the Cu_5Ge showing the transition from the orthorhombic to the hcp structure. [3] 12
2.6 The Al-Ge phase diagram. [4] 13
2.7 The Pt-Si phase diagram. [5] 15
2.8 Examples of single raw images from a movie sequence in which a Pt-Si phase is propagating in a silicon nanowire. Notice the area of growth indicated by the circle in the first image. [6] 16
2.9 Illustartion of the flux in steady-state condition where the flux is the same in different regions (dashed lines) along the slope. 18
2.10 One-dimensional model for the oxidation of silicon. [7] 21
2.11 Schematic model for Cu germanide growth process during thermal annealing. 26

3.1 Illustration of the vapor liquid solid (VLS) growth process of Si NWs. The same process describes the Ge NW growth. The VLS growth mechanism consists of three different steps: 1) Incorporation and enrichment of the Au-Si droplet by Si atoms. 2) Supersaturation of the droplets by Si. 3) Precipitation of Si atoms at the liquid/solid interface and growth of the monocrystalline nanowire.[8] 32
3.2 Illustration of the UV lithography process for the membrane fabrication. 2) The layer of resist is exposed to an UV-LED (optical lithography) using a mask (metal on quartz). The development 3) in a suitable solution removes resist in the unexposed areas. 4) Reactive ion etching using SF_6 plasma to remove the silicon nitride layer. 5) Silicon etch in KOH along the Si (111) planes to open the membrane window. 34

3.3 Photograph of the lithography side during the membrane fabrication after KOH etching. 34
3.4 a) Photograph of the patterned large contacts made by laser lithography. b) SEM image of the small markers on a single membrane, where the NWs are dispersed on the silicon nitride membrane. 35
3.5 Illustration of the process followed in both laser and electron beam lithography. 36
3.6 a) SEM images of NWs contacted by e-beam lithography. b) Large contacts defined by laser lithography are also visible. 37
3.7 a) Photograph of microfabricated commercial membrane from DENSsolutions calibrated in temperature and used during H_b heating experiments. b) SEM image showing a Mo spiral buried in two SiN layers with different windows spanned with 20 nm thick Si_3N_4 layer for electron transparency. c) SEM image on a window showing an electron lithography contacted Ge NW by a Cu metal. 37

4.1 The X-ray spectrum displayed by the Energy Dispersive system comprises characteristic X-ray peaks superimposed on the continuum (Bremsstrahlung X-rays). [9]. 45
4.2 A schematic of an infinite flat sample with its respective thickness **t** representing the X-ray absorption phenomenon. [10] 48
4.3 A schematic of an infinite flat sample with its respective thickness **t** representing the X-ray absorption phenomenon. [**?**] 49

5.1 a) Schematic of a heating sample holder that accommodates full-size TEM grids commercially available from Gatan [11]. b) Schematic of a four pins double tilt heating sample holder commercially available from DENSsolution [12]. c) Photograph of double tilt heating sample holder commercially available from Protochips Inc [13]. 54
5.2 Illustration of the direct Joule heating technique [H_a] allowing the germanide formation. (a) Schematic of a cross-sectional view representing a contacted Ge NW on a silicon nitride membrane. The Ge NW is contacted by Copper metal pads which are connected to the sample holder via Ti/Au pads contacted by small needles. (b) High angle annular dark field (HAADF) STEM image showing a top view of a connected Ge NW by two Cu metal strip lines. Cu contacts are heated one at a time via a heating current $I_{heating}$ driven by the voltage difference $(V^+ - V^-)$ while measuring the current I_{NW} through the GeNW. (c) Photograph of microfabricated membrane loaded on a 6 contact biasing sample holder from DENS solution. 56
5.3 Photograph of the system (the two current generators and the picoampermeter) connected to the TEM sample holder through an interconnect box. A labwindows program allows to monitor both heating and biasing process. 57

5.4 a) Photograph of microfabricated commercial membrane from DENSsolution calibrated in temperature used during H_b heating experiments. b) The 4 point-probe configuration where 2 contacts deliver the current (A) and 2 contacts measure the resistance (V). c) Represent the linear relation of the Mo spiral resistance over the temperature range which proves the resistance thermometer accuracy with respect to the temperature range where it's used. 58
5.5 Design drawing of the main components of the DENSsolutions double-tilt heating system. 58

6.1 In-situ copper-germanium phase propagation experiments using both in situ direct Joule heating H_a. a, c) TEM image showing the sample heated using in-situ H_a. b) The length of germanide segment versus time at $\Delta V = 0,75V$ using in-situ H_a for both opposite propagation directions L_{side1} (∘ ; fit (—)) and L_{side2}(△; fit (—)). d) The length of germanide segment versus time at $\Delta V = 0,625V$ using in-situ H_a, L (∘ ; fit (—)). 62
6.2 In-situ copper-germanium phase propagation experiments using membrane-substrate Joule heating H_b. a) TEM image showing the sample heated at 360 °C using in-situ H_b. b) The length of germanide segment versus time at 360°C for L_{side1} (∘ ; fit (—)) c, e) TEM images of in-situ heating experiments H_b at 410°C and 600°C, respectively. d) The length of germanide segment versus time at 410°C for both opposite propagation directions L_{side1}∘ ; fit (—)) and L_{side2}(△; fit (—)) f) The length of germanide segment versus time at 600°C for both opposite propagation directions L_{side1} (• ; fit (—)) and L_{side2}(▲; fit (—)). The sample reveals an influence of the NW diameter on the reaction speed. 64
6.3 TEM images before and after heating at 410°C showing the propagation taking place in a Ge NW without been contacted to the Cu pad. 65
6.4 TEM images after thermal annealing [H_b] at 600°C. a), b) TEM images taken after the in-situ [H_b] heating at 600°C where the NWs appear to be detached from the metal with or without formation of the germanide phase in the Ge NW. c), d) TEM image of the Cu contact after the heating experiment showing a degradation of the metal contact. . . 67
6.5 (S)TEM images of a Cu-Ge (NW) solid-state reaction after H_a heating process. (a),(b) HAADF STEM images of copper-germanium phase propagation after H_a heating process showing the exchanged segment length and Cu_3Ge/Ge interface, respectively. The inset image in *a* shows the shape of the protruding crystals. (c) Nano Electron beam diffraction patterns on both the Ge and Cu_3Ge part at two different orientations. . 68
6.6 (a) TEM image of a Cu-Ge (NW) solid-state reaction after [H_b] heating at 600°C showing the exchanged segment of the Cu_5Ge. (b) A diffraction pattern that is indexed as an hexagonal Cu_5Ge phase. 70
6.7 EDT slices of the reciprocal space at (hkl : l = 2n) compatible with the $P6_3$/mmc space group. 70

6.8 (S)TEM images and EDX quantification (line scan & hypermap) of different elements (O, Cu, Ge) in the NW after $H_a(V_{heat} = 0.775V)$ and $H_b(T = 600°C)$ experiments. (a) HAADF STEM image of a copper-germanium sample heated using H_a. The inset shows an EDX hypermap of the Cu_3Ge region. (b) Cu, Ge and O average concentration (at%) and local thickness profiles along the line shown in the inset in *a*. (c) schematic of the NW cross-section composed of different core-shell layers after heating. (d) TEM image of a heated sample at ($T = 600°C$) using H_b. Inset images show a HAADF-STEM image and an EDX hypermap of the crystal formed after heating at $T = 600°C$. (e) Line scan of Cu, Ge and O concentration in atom % along the defined region in the inset image in *d*. (f) Local concentration in atom % of both Cu and Ge in the crystal. 72
6.9 STEM image and EDX hypermap of Cu and Ge elements present in Cu metal after phase propagation using $H_a(V_{heat} = 1.15V)$. The Ge atoms appear to diffuse in the metal grain boundaries. 73
6.10 (S)TEM images and EDX quantification (line scan & hypermap) of different elements (O, Cu, Ge) in the NW after $H_a(V_{heat} = 0.625V)$ experiment. (a) HAADF STEM image of a copper-germanium sample heated using H_a. The inset shows an EDX hypermap of the Cu_3Ge region with the protruding crystals. (b) Cu, Ge and O average concentration (at%) and local thickness profiles along the line shown in the inset. (c) schematic of the NW cross-section composed of different core-shell layers after heating. 74
6.11 Schematic representing a silicon nitride membrane on top of a silicon substrate where a Ge nanowire is contacted from both sides by a Cu metal. 77
6.12 Temperature distribution in the heated device during *direct* Joule heating. a) The heat distribution when a heating current $I_{heating} = 0.0143$ A flows through the Cu metal and rises the temperature to a $T_{max} = 240°C$ in the contact area between the Cu metal and Ge NW. b) Zoom to represent the temperature gradient along the Ge NW. 78
6.13 Temperature profile starting from the end of the heated side to the end of the Cu contact on the other side ($I_{heating} = 0.0143$ A) in [H_a] heating experiment. 79
6.14 Schematic illustrating the section of the transformed Ge NW before and after H_a and H_b heating experiments. 80
6.15 High magnification HAADF STEM image of Cu_3Ge - Ge interface in HAADF-STEM with schematic indicating both Cu and Ge surface diffusion. 82
6.16 STEM image showing grain boundaries present in the protruding crystals after phase propagation using H_a ($V_{heat} = 0.625$ V). 83

6.17 EDX hypermap and quantification of different elements (O, Cu, Ge) in the NW after $H_a(V_{heat} = 0.625V)$ experiment. a) EDX hypermap of the germanide NW, the yellow box shows the reconstructed cross-section. b) Local thickness calculated from the detected signal (black line) and corresponding profile (brown line) simulated for hexagonal cross-section. c, b, d) Cu, Ge and O average concentration (at%) distributed along the different layers representing the reconstructed Cu_3Ge cross-section. . 84

7.1 In-situ aluminum-germanium propagation experiments using either in situ H_a and H_b. a) TEM image showing the sample heated using in-situ H_a, the 2 sides have different NW diameters. b) The length of transformed segment versus time at $\Delta V = 0.575V$ using in-situ H_a for both opposite propagation directions L_{side1} (□ ; fit (—)) and L_{side2}(∘; fit (—)). c, e) TEM images of in-situ heating experiments H_b at two different temperatures (250 - 280°C) and 330°C, respectively. The NWs in these images have different NW diameters. d, f) The length of the transformed segment versus time at two different temperatures 250°C and 330°C. d) The length of the segment versus time at 250°C in the curved NW L_{side1} (△ and fit (—)), L_{side2} (□ ; fit (—)) and L_{side3} (∘ ; fit (—)). f) The length of the transformed segment at 330°C on the big NW L (□; fit (—)). Profiles in *b*, *d* and *f* can be well fitted with a square root function eq.(2.17). 91

7.2 TEM images during an in-situ TEM H_a heating experiments where we see clearly the multiple nucleation sites of the formed heterostructure in the Ge NW. 93

7.3 In-situ aluminum-germanium propagation experiments using Joule heating [H_b]. a) TEM image showing the sample heated using in-situ [H_b] at 400°C. b) The length of the segment versus time at 400°C in the straight NW L showing a stepwise growth. 94

7.4 Different snapshots taken from the video M_3 - H_b - 380°C during the in-situ H_b heating at 380°C where we can observe the appearance of the double interface. 95

7.5 HAADF-STEM image showing the heated sample using H_b at 380°C where we can see that the Al-Ge exchange occurs only in one side of the contacted NWs. The inset is a STEM image showing clearly the double interface formed during the heating process. 96

7.6 a) TEM image of a Ge NW completely transformed to Al after being heated in a furnace at 350°C. b) A diffraction pattern on the transformed NW indexed as an FCC Al crystal oriented along the [-112] ZA. 97

7.7 a) HAADF-STEM image the bright and darker sides corresponds to Ge and Al, respectively. b) HRTEM image of the Ge/Al interface and c) the respective indexed FFT patterns of the Ge and d) Al segments. (e-h) EDX mapping of the Al/Ge interface, presenting e) RGB elemental map of Ge, Al, and O and f) the Ge, g) the Al, and h) the O map, respectively. [14] 98

7.8 EDX quantification (line scan & hypermap) of different elements (O, Al, Ge) in the NW after a $H_a(V_{heat} = 0.575V)$ experiment.(left) EDX hypermap on the NW after a H_a heating experiment indicating the different elements (O, Al and Ge). (right) Line profiles obtained along the exchanged, lower, part of the NW. Average concentration (at%) and local thickness profiles along the NW cross-section as well as a schematic representing the NW cross-section using a quantitative 3D chemical reconstruction are shown. 100
7.9 STEM image and EDX hypermaps at the interface of the formed heterostructure after H_b at 380°C. a) HAADF-STEM image of the contacted NW after the heating experiment. b) and d) HAADF-STEM zoom images of the fully exchanged NW and the double interface formed during the in-situ TEM H_b experiment. c) and e) EDX hypermaps of the corresponding regions where additional to the former detected entities Al and Ge present in the formed heterostructures, Si was found at the Al/Ge interface. 101
7.10 STEM image and EDX hypermap of Al and Ge elements present in Al metal after phase propagation using H_b heating technique at 380°C. The Ge atoms appeared to dissolved in the Al pad. An EDX spectrum integrated over the boxed region is shown in the inset, demonstrating both Al and Ge x-ray lines. 102
7.11 a) TEM image of a Ge NW contacted from both sides by an Al striplines. b) TEM image of the contacted NW after been heated using H_a technique from the both sides at $V_{heat} = 0.425 - 0.525V$ decreasing the length of the Ge segment to L = 1.46 μm. c) TEM image of the contacted NW after been damaged after a 3rd heating to decrease the resulting Ge segment length. 103
7.12 a) TEM image of a Ge NW contacted from both sides by an Al striplines. b) TEM image of the contacted NW after been heated using H_a technique from one side (showed with a yellow arrow) at $V_{heat} = 0.375-0.525V$ decreasing the length of the Ge segment to L = 1.32 μm. c) TEM image of the contacted NW after a 2nd heating from the opposite side at the same heating voltage to decrease the Ge segment length to L = 282 nm. d) TEM image of the contacted NW after been heated from both sides to decrease the Ge segment length to L = 225 nm. 104
7.13 TEM image of Al and Ge, d_{NW} = 36.5 nm, melted during H_a heating experiment. 105
7.14 (a) I-V characteristics of Al/Ge/Al segment with a diameter $d_{Ge} = 37nm$ in a two-point configuration. The red plot correspond to a Ge segment length L = 282 nm and the black plot to a Ge segment length L = 225 nm. 106
7.15 Comparison of failure current density (ampacity) and conductivity of common metals, nanocarbons, carbon nanotube-copper composites and c-Al NWs. Both carbon nanotube-copper composites and c-Al NWs clearly exceed the ampacity recom- mended for conductors by the ITRS. Figure adapted with permission from Subramaniam et al [15] copyright 2013. [16] 110

List of Tables

2.1 Summary of the resistivities of different silicide and germanide phases. [17] 8
2.2 Estimation of the substitutional Cu solubility in the Ge NW at the heating temperatures. 9
2.3 Parameter of different formed heterostructures during Cu-Ge reaction. 10
2.4 Summary of the different regimes governing the germanide phase propagation deduced from Eq.(2.30). 29

6.1 A summary of all contacted NWs showing the number of activated NWs during the solid-state reaction using the thermal heating [H_b] at 410°C. Only 4 NWs out of 42 contacted NWs were activated and gave rise to the germanide phase formation at 410°C. Hole (xx) indicates the window on the DENS chip where the NWs were located. 66
6.2 A summary of all contacted NWs showing the number of activated NWs during the solid-state reaction using the thermal heating [H_b] at 600°C. 17 NWs out of 42 contacted NWs were activated after the second heating at 600°C and were completely transformed into a Cu_5Ge phase structure. Hole (xx) indicates the window on the DENS chip where the NWs were located 67
6.3 Summary of different experiments performed on copper-germanium samples using both H_a and H_b heating techniques. All the samples show a square root evolution of the reaction interface as a function of time except at high temperature were the evolution is linear. A size dependence is clearly visible in the fit-coefficient of the length-curves reported for different diameter NWs heated with both techniques. 75
6.4 Material characteristics used for the Comsol Simulation. 77
6.5 Experimental data of the heated samples during direct Joule heating experiments [H_a]. 78
6.6 Diffusion coefficients of Cu and Ge systems at 500°C. 86
6.7 Calculated surface-diffusion coefficients 86

7.1 Summary of different experiments performed on Aluminum-germanium samples using both H_a and H_b heating techniques at low temperature. All the samples show a square root evolution of the reaction interface as a function of time. 107
7.2 Activation energy and diffusion coefficients [18, 19] for Ge and Al, and resulting diffusion constant at the annealing temperature of 330°C . . 108

7.3 Calculated Al self-diffusion coefficients 108

Abstract

The goal of this thesis is to provide a better understanding of metal incorporation in semiconducting NWs by performing in-situ heating experiments in a transmission electron microscope, with the ultimate aim to achieve a Field Effect Transistor (FET). A better understanding of the different phenomena occurring during the metal-semiconductor solid state reaction and correlation of their electrical properties to their structural characteristics can allow improved device fabrication and performance. We study two different metal-semiconductor(NW) couples : Cu-Ge and Al-Ge, due to the interesting electrical properties of their respective intermetallics in bulk, thin films and NWs systems. To provide a better electrical contact between metal and semiconductor, we thermally activate a solid-state reaction resulting in intermetallic heterostructure phase formation: the NW is transformed to a metal/intermetallic/semiconductor heterostructure. Since the NW is contacted from two sides, a similar configuration can be achieved from the opposite NW end and this can result in a semiconducting channel of nm size between two metallic contacts. We used in-situ heating and biasing experiments in a TEM to provide nm spatial resolution in order to follow all the phenomena occurring during these metal-Ge NW reactions. We used two different Joule heating techniques. The first method is referred to as H_b, is based on a membrane-substrate Joule heating where a current is passed through a Mo spiral buried in the substrate leading to an uniform heat distribution along the membrane. The second method is a new heating technique developed by Mongillo et al [20] from Silvano de Franceschi's group. We refer to it as *direct* Joule heating H_a as a current is passed through a metal stripline that partly cover the NW, leading to a very local heating. We study the kinetics of the reaction interface propagation and compare with a diffusion model. Furthermore, detailed structural and chemical characterizations were performed.

Résumé

Le but de cette thèse est de comprendre les différents phénomènes qui se produisent lors de l'incorporation d'un métal dans un nanofil semi-conducteur, lors d'un chauffage réalisé in-situ dans un microscope électronique en transmission (MET) ayant pour but de former un transistor à effet de champ (FET). Comprendre l'ensemble des phénomènes qui se produisent durant la réaction à l'état solide entre un métal et un semi-conducteur ainsi la corrélation de l'ensemble des propriétés structuraux et électriques des phases formés, pour permettre d'améliorer le processus de fabrication ainsi que le rendement des dispositifs résultants.

Au cours de cette thèse, on a étudié deux différents systémes : Cu-Ge et Al-Ge, le choix de ces derniers est dû aux propriétés électriques des phases résultantes révélés très prometteuses en bulk, couche mince et nanofil. Pour améliorer le contact électrique entre un métal et un semi-conducteur, nous chauffons le système pour activer une réaction à l'état solide permettant de créer une phase intermétallique entre le métal et le semi-conducteur, ce qui résulte en un dispositif du type métal/intermétallique/semi-conducteur. Comme le nanofil utilisé dans notre dispositif est contacté par un métal des deux côtés, une configuration similaire est réalisé du côté opposé, ce qui permet de réduire la taille du segment semi-conducteur à l'ordre de quelques nanomètre. Les expériences de chauffage et mesure électrique ont été réalisés in-situ dans le MET pour pouvoir suivre avec une résolution spatiale à l'échelle nanométrique l'ensemble des phénomènes qui se produisent durant la réaction à l'état solide entre le métal et le nanofil de Ge. Deux différentes techniques de chauffage à effet Joule ont été utilisés. La première méthode, nommé H_b, où une membrane est chauffé par effet Joule par l'intermédiaire d'un courant qui circule le long d'une spirale de Pt ou Mo enterré dans le substrat, permet une distribution de chaleur homogène dans toute la membrane. La deuxième méthode est une nouvelle technique développé par Mongillo et al [20] du groupe de Silvano de Franceschi. Dans la suite, nous avons optés à nommer cette technique par chauffage directe par effet Joule H_a où un courant électrique circule à travers du métal de contact qui couvre le nanofil partiellement, permettant un chauffage très locale au niveau du contact. Nous étudions la cinétique de la propagation en suivant l'évolution de l'interface de réaction et en la comparant à des modèles de diffusion.

Chapter 1

Introduction

In the last decades, reducing the size of devices has been an important goal in many research fields ranging from material science, microelectronics to life science. In microelectronics, the size reduction of devices has been particularly successful. In 1971, the size of transistors in state-of-the-art-chips was 10 μm. Nowadays, their size decreased to nanometers scale with a gate length of about 14 nm, which allows a huge improvement on circuits efficiency. Moore's law, a prediction made by the co-founder of the semiconductor giant Intel, predicts doubling the number of transistors in an integrated circuit every two years. With the present technologies, size reduction of the planar bulk MOSFET should reach its limits in a few years and Moore's law will no longer be viable. So, other alternatives should be propose to replace these conventional planar bulk MOSFETs with the aim to follow this law and reach the transistor scale predicted in 2020. One of the alternatives that has been targeted in the last few years are semiconductor nanowires (NWs) appearing to be a logic evolution of the conventional planar bulk MOSFET channel. Many NW systems can be grown using different materials for example the III-V, II-VI and IV. This latter group IV compounds (Si and Ge) attracted a lot of attention due to the compatibility with the CMOS technology. In chapter 2 we will discuss in details on these nano-materials: growth, shape, orientation, ... Furthermore, to allow successful incorporation of these semiconducting NWs in applications, low Ohmic resistance contacts need to be achieved, potentially using a silicidation process in Si, or germanide process in Ge, to efficiently inject and extract current from the device. A silicide (or germanide) is a intermetallic compound formed after a solid-state reaction between a metal and silicon (or germanium). The aim of the germanide phase is to lower the electrical contact resistance between the source/drain and in the gate

(by reducing the resistance of the poly-Si) in a MOSFET. Hence, many studies [20–39] have achieved electrical contacts between silicide or germanides and semiconductor NW systems either using Si NWs : Ni-Si, Pt-Si, Co-Si, Pd-Si, Ti-Si and Cu-Si or with Ge NWs : Ni-Ge, Cu-Ge, Al-Ge, Mn-Ge revealing interesting electrical contact properties and a versatile potential for applications in new nanoelectronic devices.
In this thesis, we will focus on the solid-state reaction carried out in-situ in a TEM, allowing the formation of such silicide and germanide heterostructures, with the aim to lower the contact resistance either by using a very localized Joule heating on a metal stripline deposited on the NW [20], or by using a membrane-substrate Joule heating [12]. In this latter, a current is passed through a buried Mo heating spiral, leading to a more conventional situation where the entire sample is heated. The first method is referred to as *direct* Joule heating H_a and the second method is referred to as membrane-substrate Joule heating H_b. The two heating techniques are compared and we can estimate diffusion constants by following the position of the germanide/Ge interface as a function of time. Two material couples were studied: Al-Ge and Cu-Ge systems. Electrical characterization of the devices was theoretically possible, but due to sample fabrication issues only very preliminary results will be shown. We focus on the formation mechanisms of metal-semiconductor heterostructures during heating due to diffusion of the contacted species. Initially the aim of the PhD was to study the Pt-Si system, but preliminary results were not promising. Therefore the PhD was reoriented to Cu-Ge and Al-Ge.

Outline of the manuscript

The **first chapter** is a brief introduction to this PhD work.

The **second Chapter** recalls the basic interest of intermetallic phases and the band arrangement when a metal and a semiconductor are in contact. We review different studies existing in literature, where we focus on the metal-semiconductor solid-state reaction with three different metals : Cu, Pt and Al, reacting either with Si or with Ge. We show the preliminary results obtained on Pt-Si and a comparison with literature. We finish the chapter with a section stating the general diffusion equations, and a model to explain the diffusion in NWs. In later chapters this model will be explained in more detail and used to interpret experimental results.

The **third Chapter** describe the fabrication of the studied samples. Firstly, the formation mechanism of the used nanowires is recalled. Then the protocol to achieve reliable samples for in-situ TEM measurements is described. Conventional cleanroom fabrication techniques were used for our fabrication process. Transparent electron Si_3N_4 membranes were fabricated where a Si or a Ge NW was deposited. The deposited NWs were individually contacted from both sides either by a Cu or Al metal, which are connected to an external electrical setup via the TEM sample holder.

In the **fourth Chapter**, the different electron microscopy instruments and techniques that were used during the experiments are presented. Our aim is to recall the characteristics of the different techniques used in transmission electron microscopy that provide information which allows a better understanding of the phenomena occurring during our heating experiments. We present also an EDX model providing a 3D reconstruction of the composition of the nanowire cross-section.

In the **fifth Chapter** we present the different equipment that allow to perform our in-situ experiments. We describe briefly the sample holder and the external electrical setup used for both H_a and H_b heating techniques. We show also the mounted setup as it is before an in-situ TEM heating experiment in both Joule heating methods.

In the **sixth Chapter** we present the results gathered during in-situ transmission electron microscopy heating experiments on a Cu-Ge NW system using two different methods of Joule heating (described in chapter 5). We performed a kinetic and structural study in order to explain the reaction mechanism and determine the resulting phases occurring using both Joule heating techniques. The kinetic study was achieved by following the location of the reaction interface as a function of time in the different heating experiments and the results are explained using a diffusion model presented in chapter 2. The structural analysis of the reacted NW part were performed by electron diffraction and energy dispersive X-ray analysis where a 3D chemical reconstruction of the reacted segment cross-section was realized. This reveals a double-core shell structure of the transformed segment with a Cu_3Ge core, surrounded by thin layers of Cu (1 nm), Ge (0.35 nm) and GeO_2 (4.5 nm) : an experimental observation of the surface diffusion layer. During the reaction, germanide crystals typically protrude from the reacted NW part. Their appearance does not modify the kinetics of the reaction and can be avoided using a shell around the initial Ge NW. By combining all these results and based on the presented diffusion model, we succeed to propose a mechanism that describes the formed phases both a at low and high temperatures.

In the **seventh Chapter** we present the results obtained during in-situ transmission electron microscopy on the solid-state reaction of Al and Ge NWs using both H_a and H_b heating experiments. We study the location of the interface as a function of time, and explain the observed behavior using a diffusion model. HRTEM and diffraction analysis showed a complete exchange of the Ge with Al in the reacted region after annealing using either H_a or H_b heating experiments resulting in an Al NW after a complete exchange. A model based EDX characterization confirms that the reacted part of the NW is pure Al and only very low Ge concentrations of a few atomic percent can be detected in a very thin (2 nm and less) radial shell around the pure Al core. By combining all these results and based on the diffusion model presented in chapter 2, we succeed to propose a mechanism that describes the formed phases both a low and high temperatures. Furthermore, we present the different electrical characteristic reported in [14, 16] in these formed samples to show that Al/Ge is a very promising system at low and ambient temperatures.

Author contributions

The Si and Ge NWs studied in this PhD were grown either in the SiNaPS group in CEA-Grenoble, or in the Technical University of Vienna. Samples for H_a heating experiments with Cu-Ge and Al-Ge were fabricated in Vienna by Clemens Zeiner, Florian Brunbauer and other students in the group of Alois Lugstein. Samples for H_b heating experiments, as well as preliminary samples for H_a heating on the Pt-Si system were fabricated by Khalil Elhajraoui. In-situ TEM was performed by Khalil Elhajraoui on the CM300 TEM. Experiments on the Titan Themis and Osiris for EDX analyses were performed in collaboration with Eric Robin and Miguel Lopez Haro. Experiments on the Titan for nanobeam diffraction were performed in collaboration with Jean-Luc Rouviere. Electron diffraction tomography was performed in collaboration with Stephanie Kodjikian. Martien den Hertog helped with sample fabrication, in-situ experiments and the global organisation of the work. Treatment of the data was performed by Khalil Elhajraoui with help from the respective collaborators. Results were discussed between all collaborators.

Chapter 2

Metal-Semiconductor Solid-State Reaction

2.1 Metal-Semiconductor Solid-State Reaction

A metal/semiconductor solid-state reaction consists in forming an intermediate phase between the metal and semiconductor due to the movement of the metal atoms through the semiconductor compound or by movement of both species. These formed heterostructures increase the contact quality due to two major characteristics [40]:

- their low resistivities ranging between $\mu\Omega$.cm up to hundreds of Ω.m
- their high temperature stability and good oxidation resistance based on the formation of a native oxide layer.

These properties were demonstrated in many publications either in bulk or thin film materials (NiSi, PtSi, Cu_3Ge, ...) [3, 39], and they were expected to be improved in NWs due to the excellent electrical and structural properties of NWs. Very abrupt interfaces between silicide and Si were formed in NWs, which might help to avoid Fermi-level pinning effects and interface states commonly reported in metal-semiconductor contacts [41].
Before going further, a brief introduction to metal/semiconductor junctions will be given

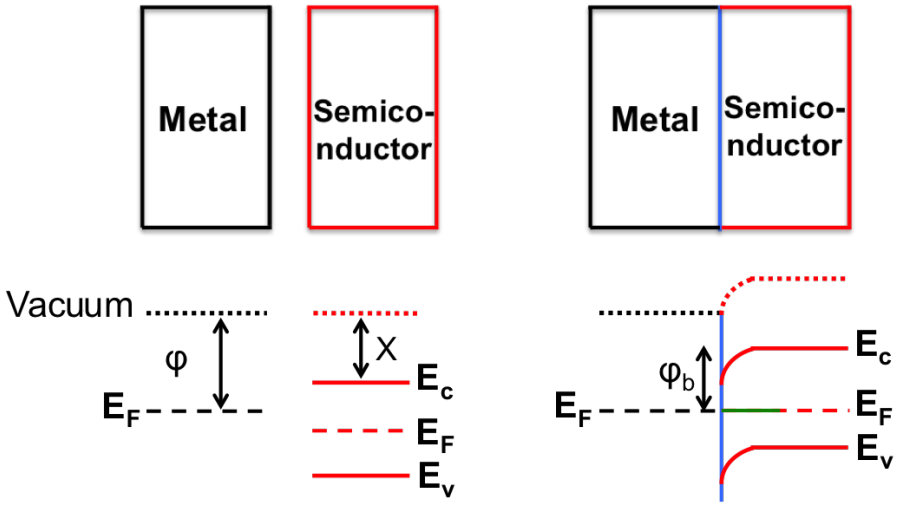

FIGURE 2.1: Illustration of the near-interface region of a metal-semiconductor junction, interaction with the metal causes electronic states to appear in the bandgap of the semiconductor: associated with these states is a charge neutrality level denoted by the green line. In general, the metal Fermi level will not be at the charge neutrality level and a local band bending can occur in the semiconductor to pin the Fermi level there. Adapted from [1].

2.1.1 Electrical Characterization of Metal-Semiconductor Contact

Generally, the interest in contacted semiconducting nanostructures is in the alignment of the Fermi level in the semiconductor with respect to the metal. Metal-semiconductor contacts are influenced by the difference in work function of both materials [42] creating a so-called Schottky contact. Moreover, in a bulk metal-semiconductor contact interface states are often induced in the semiconductor band-gap and a charge neutrality level is associated with these metal-induced gap states. In most cases, the Fermi level and the charge neutrality level are misaligned which induces a local charge in the semiconductor, thus, an image of this local charge is created in the metal. This dipole drives the valence and the conduction bands to bend near the interface which allows an alignment between the Fermi level and the charge neutrality level, a phenomenon called Fermi-level pinning (see Fig.(2.1)) [1]. One of the solutions to reduce this contact issue is the formation of a metal/semiconductor heterostructure called silicide or germanide phase in Si and Ge, respectively, with the aim to create an interface as perfect as possible (see Fig.(2.2). Indeed, these heterostructured NWs have been shown to form field effect transistors (FET) using the transformed regions as source/drain contact to the semiconducting channel [35]. Because the FET channel can be scaled by tuning the annealing time, the length of

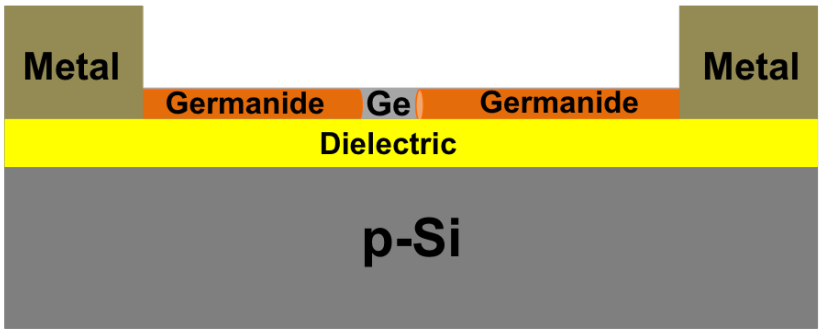

FIGURE 2.2: Schematic of a Field effect transistor (FET) based on a Ge nanowire with a germanide formed phases.

the semiconducting channel is independent of the spatial resolution of the lithography process. Many studies investigated the heterostructure phase formation in Si and Ge NWs using different metal contacts. Historically, titanium (Ti), cobalt (Co), nickel (Ni) and copper (Cu) metal contacts were studied extensively in Si and Ge thin films and these material couples have been extended to NWs due to their low electrical resistivities. Recently other metals like Mn [36, 37] and Pt [38], were used to form different heterostructures for new device applications. Especially Ni attracted a lot of attention due to the low resistivity values of its intermetallic phases in both Si and Ge thin films (see Table.2.2), especially NiSi and NiGe. Therefore, Ni/(Si or Ge NW) systems were identified as the best candidates to provide reliable electrical contacts and the Ni/Si NW system was extensively studied in the last decade. Si was more extensively studied with respect to Ge NWs because CMOS technology is based on Si. However, Ge is very attractive for many reasons, for instance, its high electron and hole mobilities which provide high device performance [34] and its large exciton Bohr radius allowing the observation of quantum confinement effects in relatively large structures and at high temperatures, making it a potential candidate for high speed quantum computing [45]. Therefore, we have focused on Ge NWs instead of Si NWs in the thesis.

Moreover, most studies on the Ni/Si NW system report the formation of several phases and sometimes the lowest resistivity NiSi phase is not present. It appears to form only in some special experiments such as point contact reactions [31] or using a Pt diffusion barrier insertion [32]. Similar observations were made on the Ni/Ge system were the NiGe heterostructure appears to be very difficult to form and control. Therefore, Cu metal appears to be a logic substitution to Ni contacts in Ge NWs due to the low resistivity of the formed heterostructure (see table.2.2).

TABLE 2.1: Summary of the resistivities of different silicide and germanide phases. [17]

	Phases	Resistivity ($\mu\Omega$.cm)		Temperature (° C)	
	Thin film	Nanowire	Thin film	Nanowire	
	Ni_2Ge	20 - 50	—		400 - 500 [41]
	NiGe	15 - 20	22 [41]	—	450 [41]
Ge	Cu_3Ge	5.5 - 24	34 [34]	—	310 [34]
	Co_2Ge	35	—	—	
	$TiGe_2$	20	—	—	
	$Ni_{31}Si_{12}$	90 - 150	51 [43]	—	425
	δ-Ni_2Si	24 - 30	20 [43]	200	—
	NiSi	10 - 18	~ 10 [43]	350 - 600	—
	$NiSi_2$	34 - 50	24 [43]	600 - 800	—
Si	PtSi	28 - 35	28.6 [38]	250 - 400	520 [38]
	$TiSi_2$	60 - 70	—	500 - 700	—
	Co_2Si	70	213	300 - 500	—
	CoSi	100 - 150	510	400 - 600	—
	$CoSi_2$	14-20	30 [33]	600 - 800	750
	Cu	3.5	1.7	—	—
	Al	0.13[16]	2.72 [44]	—	—

2.2 Copper-Germanium System

The use of Cu metal in semiconductor technology initiated extensive studies on its behavior in contact to Si or Ge systems. Although compared to Al, Cu is characterized by a low resistivity and a high resistance to electromigration. On the other hand, the high diffusivity of Cu in Ge and Si causes device failure of integrated circuits. Therefore, many studies were done to understand the diffusion of Cu atoms in the semiconducting systems with the aim to limit its incorporation in the active region of the device. These studies were well summarized by Bracht [46]. The Cu atoms were reported to be the fastest and dominant diffusing species in the Ge system compared to all other transition metals and other species, and tend to form a germanide phase [47]. The diffusion of Cu atoms in Ge appears mediated by positively charged Cu ions [48] diffusing through interstitial sites and under the solubility limit, Cu is incorporated by the dissociative mechanism, describing the inversion of the Cu_i atom from the interstitial site to the substitutional site via a vacancy [49].

$$Cu_i + V \rightleftharpoons Cu_s \tag{2.1}$$

Therefore, the diffusion mechanism of Cu in Ge is controlled by crystal defects. A maximum solubility was reported to be 4.10^{16} cm^{-3} at 880°C. Below the solubility limit the C_{Cu_s} was given by [46]:

$$C^{eq}_{Cu_s} = 3.44 \times 10^{23} \exp(\frac{-1.56}{k_B T})\, cm^{-3} \tag{2.2}$$

The Ge NWs are defect free [34]. If vacancies can be created, they will be present at or near the Ge/GeO_2 interface (presence of dangling bonds). Thus, we can assume that the substitutional Cu_s will be predominantly present at the NW surface until the limit of solubility of Cu atoms in the Ge NW. We can estimate a solubility limit of Cu_s atoms at different temperatures used in our experiments using the equation (4.2). However, in our experiments we cannot follow the diffusion of Cu atoms in their sol-

TABLE 2.2: Estimation of the substitutional Cu solubility in the Ge NW at the heating temperatures.

Temperatures	Solubility of Cu (atom/cm^3)
360°C	1.27×10^{11}
410°C	1.03×10^{12}
600°C	3.33×10^{14}

ubility limit. We will study the formation and growth rate of the germanide phase at different heating temperatures using different heating techniques. The interest of forming the germanide phases, specifically the ϵ_1-Cu_3Ge, is that additionally to its electrical characteristics already mentioned above, it has also been reported to be an excellent barrier to hinder the diffusion of Cu into Si, making the ϵ_1-Cu_3Ge an attractive material for applications as contacts and interconnects in Si devices [3].

2.2.1 Phase diagram & Literature

According to the Cu-Ge phase diagram published by Olesinski and Abbaschian, see Fig.(2.3), the Cu-Ge reaction gives rise to 5 different intermetallic presented in Table.(2.3). A study was carried out in thin films by Aboelfotoh in order to investigate the electrical resistivity of Cu-Ge thin films as a function of Ge atom% [50]. Only two intermetallic phases were reported to form in the Cu-Ge system with different Ge atom% ranging from 5 to 50. The ζ phase starts to form by adding 5 atom% of Ge and the ϵ_1- Cu_3Ge (orthorhombic) appears in the system after adding 20% and remains stable until 25 atom% of Ge. These two structures (ζ and ϵ_1) were reported to form

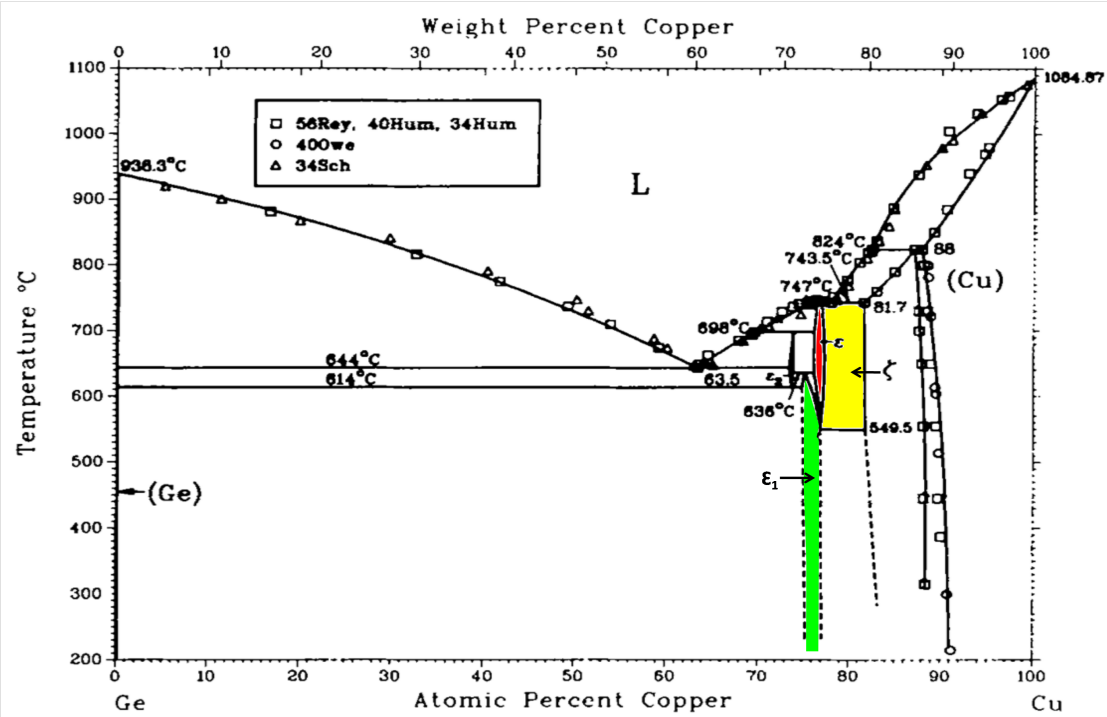

FIGURE 2.3: The Cu-Ge phase diagram.[2]

TABLE 2.3: Parameter of different formed heterostructures during Cu-Ge reaction.

Phases	Structure	Group	Lattice parameter (Å)	V (Å^3)	N (atom.Å^{-3})
ϵ_2– Cu_3Ge	Cubic	$Im3m$	a ≃5.15	–	–
ϵ_1– Cu_3Ge	Mono	$P21$	a = 2.63, b = 4.56, c = 4.20	50.36	0.044
ϵ_1– Cu_3Ge	Ortho	$Pmmn$	a = 5.29, b = 4.55, c = 4.20	101.4	0.044
ϵ– Cu_3Ge	Rhomb	—	a = 4.17, c = 5.00	–	–
ζ– Cu_5Ge	Hexa	$P6_3/mmc$	a = 2.58, c = 4.22	25	0.066

in the majority of Cu-Ge studies. Two different crystal structures were reported for the ϵ_1 phase. The only study reporting the formation of the ϵ_2 and the ϵ-Cu_3Ge structures, apart from the phase diagram [2], used an amorphous layer of Ge deposited on top of polycrystalline Cu and well controlled heating (3°C/min) [51]. On the other hand, both monoclinic and orthorhombic ϵ_1-Cu_3Ge were reported [51, 52] to form at low temperatures [180 - 210° C] and remain stable up to 540° C. The formation of this phase has been shown to be controlled by the diffusion of Cu atoms through the Ge layer. The ζ phase formation was reported to occur depending on the nature of the substrate used in the solid-state reaction. In an amorphous Ge layer in contact to an oriented (111) Cu layer, the ζ phase appeared to be the first phase to form. On the other hand, in crystalline Ge layers the ϵ_1-Cu_3Ge appeared to be the first formed phase.

The ζ phase has a much higher resistivity ($\rho_{Cu_5Ge} = 2\ \rho_{Cu_3Ge}$) than the ϵ_1 phase and

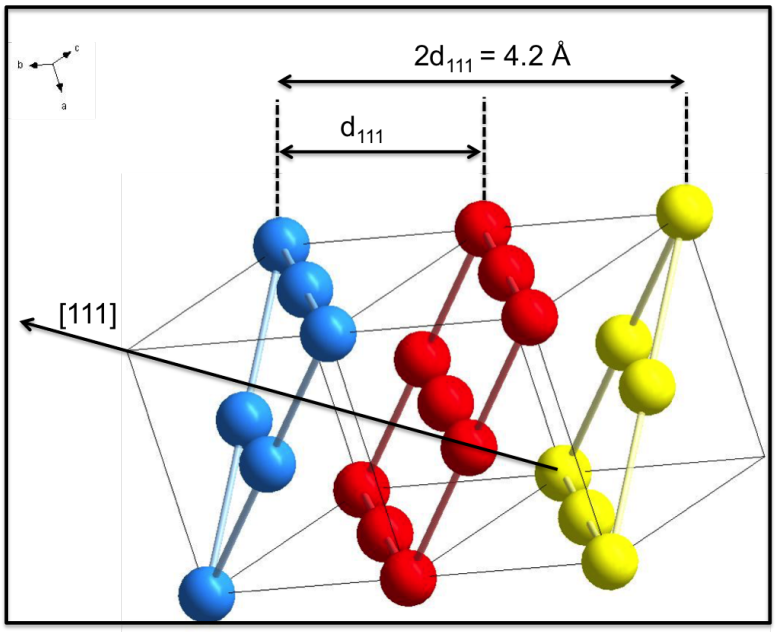

FIGURE 2.4: Copper structure with the respective (111) planes.

is therefore of minor interest [3].

Furthermore, a structural transition from the Cu structure to ζ and ϵ_1 phases is described in [3] see Fig.(2.5). Thus, the ϵ_1 and ζ appear to grow along the (111) planes of the Cu crystal and a relation of the lattice parameters $2d_{111} = b_{ortho} = c_{hcp}$ was found.

However, in NWs the only reported phase is the orthorhombic ϵ_1-Cu_3Ge phase appearing at low temperature (below 500°C)[30, 34]. The formation of these two different phases in thin films were reported to be limited by Cu diffusion in Cu_3Ge and by nucleation in Cu_5Ge. In the Cu-Si system a similar observation was made: Cu_3Si and $Cu_{15}Si_4$ were found respectively for temperatures below and above 600°C [29].

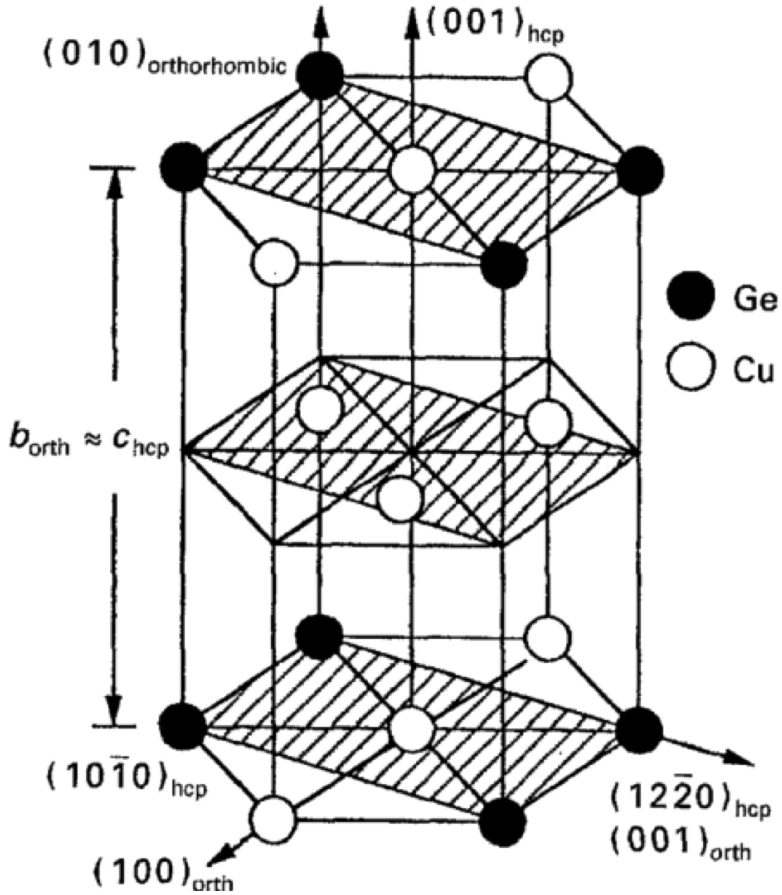

FIGURE 2.5: Illustration of both Cu_3Ge(hatched) and the Cu_5Ge showing the transition from the orthorhombic to the hcp structure. [3]

2.3 Aluminum-Germanium System

Aluminum (Al) metal, similar to Cu, was used historically as interconnection material in integrated circuits. The Al low-resistivity makes it a good candidate for Metal/NW contacts. In addition, the Al/Ge NW couple has not yet been extensively studied, which make it very interesting. The idea came from our collaborators, Alois Lugstein's group made for the first time a reliable Field Effect Transistor (FET) using the Al/Ge/Al NW system [14]. They tried, before achieving such devices, to build a FET based on the Al-Si(NW) system. No reaction occured between Al pads and Si NWs. Therefore, they tested the Al-Ge system in Ge NWs where the exchange reaction took place. However, the Al exchange with the Ge NW didn't occur in the first attempts, where the Al deposition was performed by e-beam evaporation. These samples didn't show any exchange reaction under annealing. Successful samples showing an Al-Ge exchange reaction were obtained after a metal deposition using either sputtering or

a combination of first sputtering followed by e-beam deposition, and using an annealing temperature of 350°C for NW diameters ≤ 150 nm.

2.3.1 Phase diagram

The Al/Ge system was studied by McAlister and Murray, see Fig. (2.6), where they present the phase diagram.

As it can be seen in the phase diagram, no intermetallic phases form during the

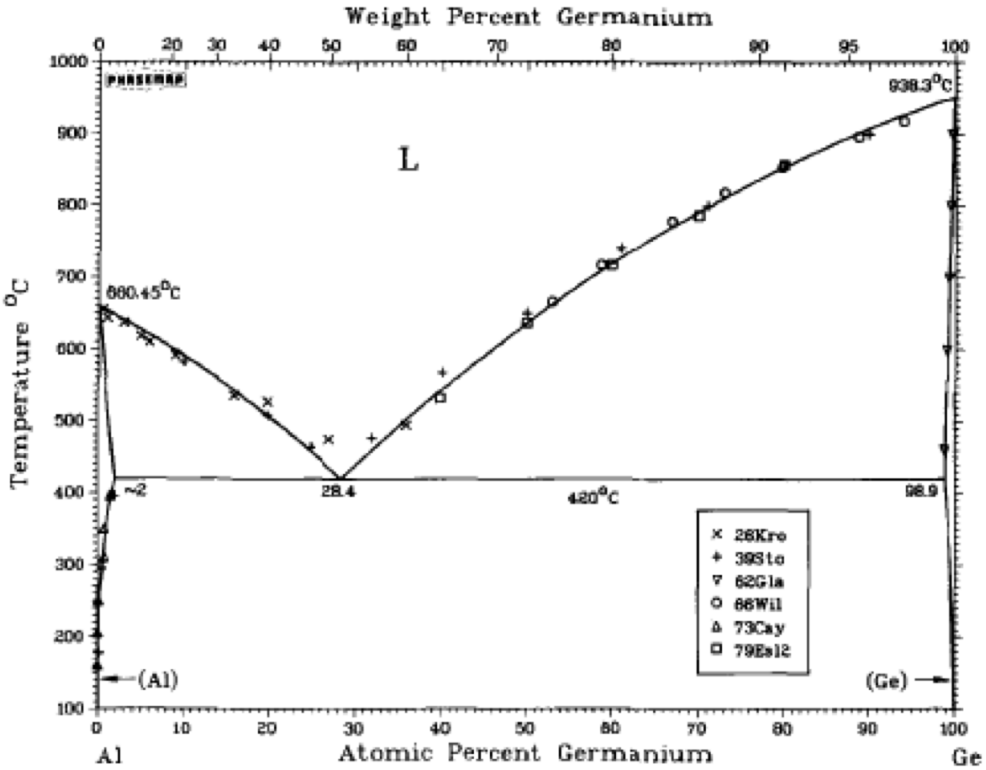

FIGURE 2.6: The Al-Ge phase diagram. [4]

solid-sate reaction between Al and Ge. A simple eutectic (L ⇌ Al + Ge) is present at 420°C. In addition, at the eutectic temperature, the solubility of Ge in Al and of Al in Ge is estimated to be ~ 2 atom% Ge and ~1 atom% Al, respectively.

The only intermetallic prepared in the Al-Ge system was the metastable $Al_{70}Ge_{30}$ phase made by quenching the Al-Ge melt [4]. Outside of these special conditions, no intermetallic phase appeared to form in the Al-Ge solid-state reaction.

2.4 Platinum-Silicium System

The Pt-Si couple attracted attention for its characteristics :

- In thin films, high quality ohmic contacts where reported on p-Si. [53–55]
- Defect free heterostructures were observed in NWs. [38]

In addition, the Pt-silicidation process in Si NWs has been reported to occur at low temperatures similar to the Cu-Ge system. Therefore, our motivation was first to trigger in-situ in the TEM the formation of the different silicides in Si NWs and perform a kinetic study, since no data are available on the kinetics of the platinum silicide in NWs. Another interest was the influence of the local Joule heating technique on the first formed phase or the sequence of the formed phases (since more than one silicide appears to form during the Pt-Si solid-state reaction). Second, we wanted to evaluate the electrical quality of the silicide/p-SiNW interface using holography (a TEM interference technique).

2.4.1 Phase diagram

The Pt/Si solid-state reaction was studied in bulk materials showing many formed silicides as we can notice in the Pt-Si phase diagram, see Fig.(2.7). The formation of these different silicides has been discussed in many studies with the aim to predict the first formed phase.
However in Si NWs different studies performed using Pt metal in contact with Si NWs reported the formation of two different silicides (Pt_2Si and PtSi) [28] or only one silicide (PtSi) [27, 38].

2.4.2 Pt-Si (NW) Solid-State Reaction

The solid-state reaction in the Pt/Si NW system where Pt is contacted to a Si NW is shown to form a silicide channel with an abrupt interface in few studies [26, 27, 38]. It was shown by [38] that the PtSi phase forms with an abrupt interface at the PtSi/Si interface. In addition, the electrical properties of the PtSi silicide show a low resistivity (~ 28.6 $\mu\Omega$.cm) better than the PtSi thin films (45 - 68 $\mu\Omega$.cm).

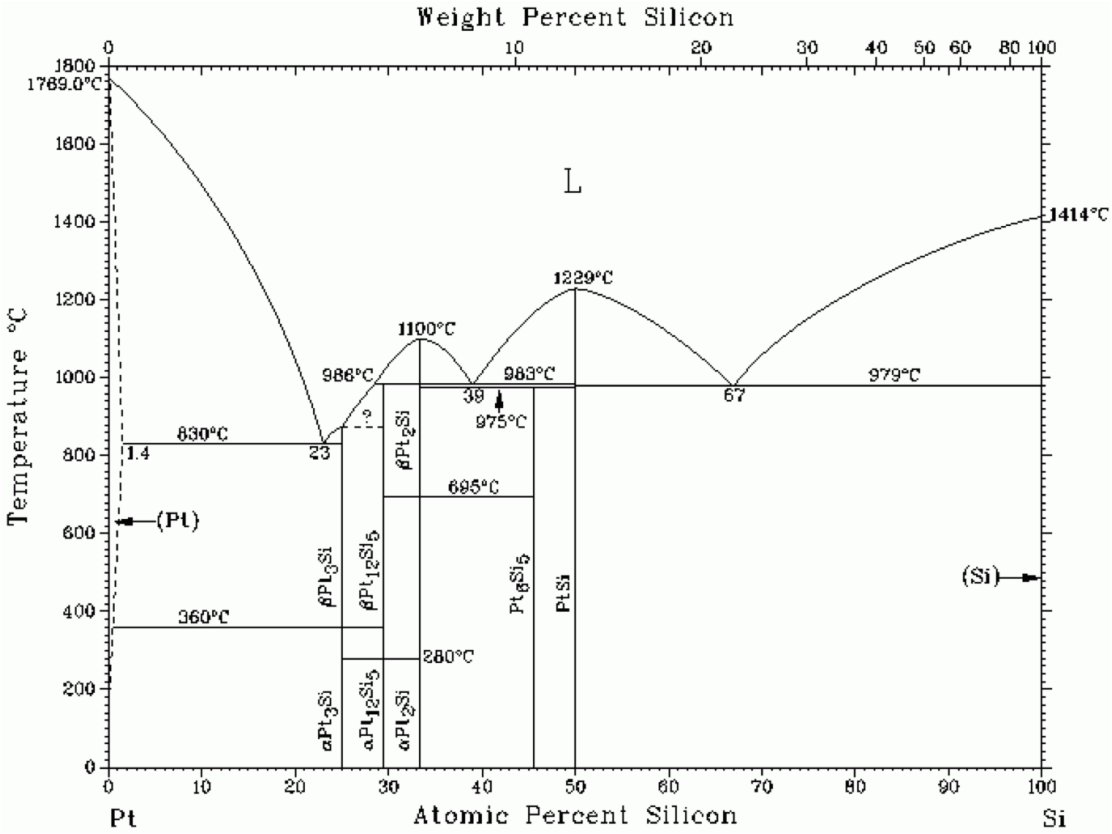

FIGURE 2.7: The Pt-Si phase diagram. [5]

An in-situ Joule heating experiments were performed on Si NWs (~50 nm) contacted by Pt metal (100 nm) on a silicon nitride membrane (~ 50 nm thick) (fabrication steps will be described in chapter 3) with the aim to form a PtSi silicide. However, fabrication issues hindered achieving reliable samples. The Pt adherence to the Si_3N_4 substrate limited the efficiency of the sample preparation. We used e-beam evaporation similar to [38] and sputtering for metal deposition.

Ultimately, we realized some Pt/Si NW samples. Though we could start the reaction in some NW samples, the NWs detached easily from the Pt strip during the Joule heating treatment or a gap is formed in the intermetallic part after propagation over some ten of nm's. The start of the reaction, where a nucleation of Pt_xSi_y appeared to take place in the Si NW is shown in Fig.(2.8).

These images were taken at low accelerating voltage (60 kV) using a p-n charged couple device (pnCCD) TEM camera at ERC Julich (carried out as an ESTEEM 2 project). The applied voltage difference on the Pt metal strip was raised to V_{heat} = 1 V. The images show the evolution of the Pt_xSi_y/Si interface during the growth process. They were recorded continuously with 1000 fps for over 30 minutes. The resulting high speed movie shows the growth process with millisecond time resolution. Various

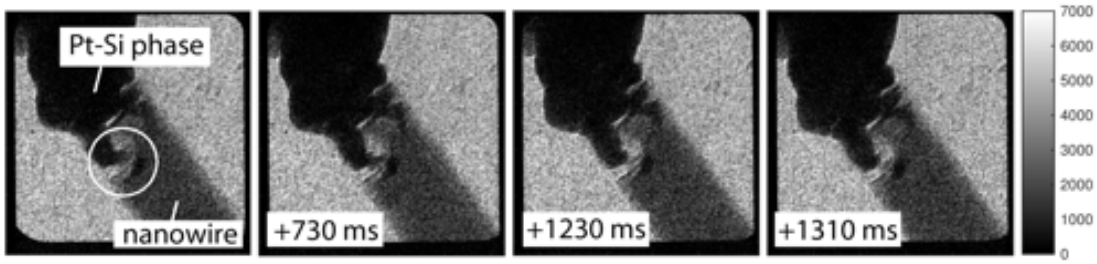

FIGURE 2.8: Examples of single raw images from a movie sequence in which a Pt-Si phase is propagating in a silicon nanowire. Notice the area of growth indicated by the circle in the first image. [6]

abrupt propagation steps could be observed in the movie, before a gap appeared in the silicide region.

A previous study by Dellas et al [28], reported similar phenomena. They show that Pt_2Si appears to form in a similar manner as the presented phase in Fig.(2.8).

According to their results on the Pt reaction with oxidized and as-grown Si NWs, the nucleation of the silicide phase was inhibited either by an oxygen contamination or by the presence of the native oxide.

In our samples, an Ar plasma was used to remove the SiO_2 and we doubt on the efficiency of the etching. Therefore, the second hypothesis appears likely for these samples. However, many other attempts to achieve Pt/Si NW samples were made also including an HF treatment prior to metal deposition, but we did not succeed to realize samples where the nucleation took place in a reliable way. In addition to the adherence issues between Pt metal and the silicon nitride substrate, stitching errors during the e-beam lithography process hindered the fabrication process. For these reasons, the PhD was reoriented to the Cu-Ge and Al-Ge systems, that were also studied by the collaborating team of Alois Lugstein.

2.4.3 Conclusion

The Pt silicide presents a high potential for low resistance electrical contacts on Si. A recent study by Wu et al [26] shows a successful sample where 400 nm Pt metal was deposited using the Focused Ion Beam (FIB).

2.5 Diffusion

2.5.1 Fick's Law

Since diffusion processes certainly contribute to the germanide phase formation, we briefly recall the relevant equations governing diffusion phenomena. Adolf Fick (1855) first described the diffusion in the salt-water system [56], where he developed an equation governing the occurring phenomena by establishing a linear response between the concentration gradient and the mixing of salt and water. Fick's first law describing the flux of diffusing particles in one dimension is written as follow :

$$J_x = -D\frac{\partial C}{\partial x} \tag{2.3}$$

where J_x is the flux of the diffusing particles, D is the *diffusion coefficient* or the *diffusivity* of the particles considered and C is their concentration. The negative sign indicates the opposite directions of diffusion flux and concentration gradient. Diffusion is a process which leads to an equalization of concentration. This equation permits to determine the diffusion coefficient in the steady state regime (the concentration gradient is time independent) as is represented in Fig.(2.9). The vector of the diffusion flux J is directed in opposite direction to the concentration gradient vector ΔC. The concentration gradient vector always points in that direction for which the concentration field undergoes the most rapid increase.
In steady state, the concentration profile is fixed and the flux is the same in different regions along the slope as it is described in Fig.(2.9). When following the steady state conditions, that means :

- Concentrations at the boundary conditions are constant with time.
- Diffusion is limited to molecular motion within the solid.
- Diffusivity is not influenced by concentration.
- There are no temperature gradients in the solid.

Usually, in diffusion processes, the number of diffusing particles is conserved. To integrate the conservation of matter into the equations of diffusion an equation of continuity has been created :

$$\frac{\partial C}{\partial t} + \frac{\partial J}{\partial x} = 0 \tag{2.4}$$

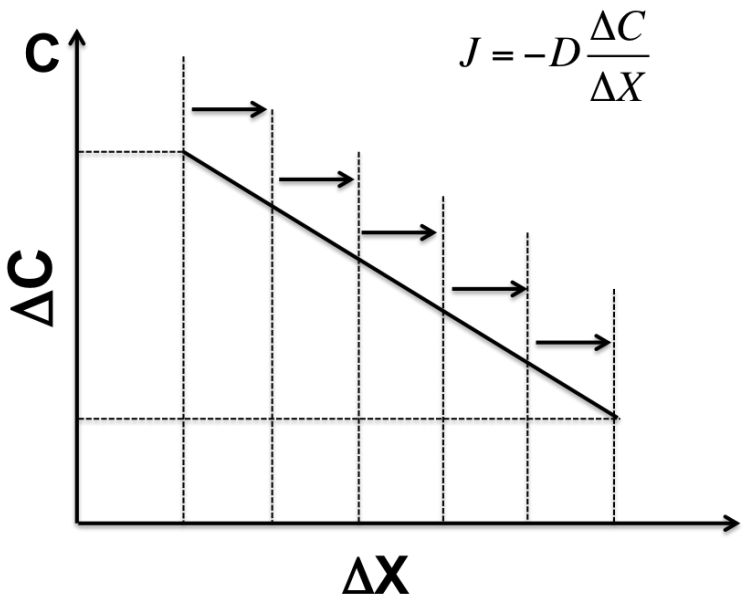

FIGURE 2.9: Illustartion of the flux in steady-state condition where the flux is the same in different regions (dashed lines) along the slope.

The equation of continuity describes the system in non-steady state or transient regime. If Eq.(2.4) $\neq 0$ the diffusion depends on position and time. In steady-state condition, the interactions of atoms like chemical reactions or reactions between different sites in a crystal, etc, are neglected [56]. The combination of Fick's first law and the equation of continuity above give Fick's second law in the general case :

$$\frac{\partial C}{\partial t} = -\frac{\partial}{\partial x}(-D\frac{\partial C}{\partial x}) \tag{2.5}$$

To simplify the equation, we consider that the diffusivity is independent of concentration, which is the case for tracer diffusion in chemically homogenous systems or for diffusion in ideal solid solutions [56], the Eq.(2.5) simplifies to :

$$\frac{\partial C}{\partial t} = D\frac{\partial^2 C}{\partial x^2} \tag{2.6}$$

The Fick's second law in the general case (2.5) can be found also under the name of the linear diffusion equation and it is a linear second-order partial differential equation for the concentration field $C(x, y, z, t)$. Different solutions of Eq.(2.6) are presented and demonstrated in [56] where its solved in both steady and non-steady state or transient conditions.

2.5.2 Thermodynamic description of diffusion

From a fundamental point of view, the assumption that the concentration gradients are the driving forces of diffusion, as given by Fick's laws, is not always correct. More generally, the gradient of the chemical potential μ_i of a component i is the real driving force, and can be written as :

$$\mu_i = \mu_i^0 + RT\,ln(a_i) \tag{2.7}$$

where a is the thermodynamic activity and μ^0 is the standard chemical potential for the pure phase (constant). The activity a of a component i is written as a function of its concentration c_i and γ_i, the activity coefficient, where $a_i = \gamma_i c_i$.
Using the chemical potential, Fick's law can be rewritten by substituting Eq.(2.7) in Eq.(2.3) and assuming that the solid solution is ideal then $\gamma_i = 1$, $a_i = c_i$. Therefore, in one dimension, we have :

$$J_x = -\frac{Dc_i}{RT}\frac{\partial \mu_i}{\partial x} \tag{2.8}$$

At an interface separating two regions of different concentrations or chemical potential, a diffusion flux occurs. In this case, the concentration or chemical potential curve is an Heavy side function and its derivative is a dirac multiplied by the difference of the concentrations or chemical potentials at each side of the interface. We thus have Eq.(2.9).

$$J_{interface} = -D(C_2 - C_1)\delta(x) \tag{2.9}$$

Eq.(2.9) is a special application of the Fick's laws. It describes the flux due to reactions or absorptions at interfaces. This equation can also be obtained by supposing that the interface has a finite, but very small, width d. Then using Eq.(2.3), one obtains :

$$J_{interface} = -D\frac{(C_2 - C_1)}{d} \tag{2.10}$$

By noting $D/d = k$, an equation similar to Eq.(2.9) the previous one can be obtained :

$$J_{interface} = -k(C_2 - C_1) \tag{2.11}$$

where k is a constant describing the reaction or absorption of the active species at the interface. Such relations are used in the next part.

2.5.3 The Deal and Grove Model

2.5.4 Original Model

Deal and Grove [57] were the first to build a simple model describing the formation of a new phase after the diffusion of some species. They studied the oxidation of a silicon substrate by oxygen. In their model, the oxidation process was described in 3 steps [7].

1. Absorption of the oxidizing gas at the outer surface of the oxide
2. Diffusion of the oxygen atoms across the oxide film towards silicon.
3. Reaction of the oxygen with silicon at the Si/SiO_2 interface, i.e. formation of a new SiO_2 layer.

By assuming, a steady state regime, Deal and Grove applied the equations (2.3) and Eq.(2.11) of the previous part and they obtained :

1. $J_1 = k\,(C^* - C_0)$
2. $J_2 = D\,\frac{C_0 - C_s}{x}$
3. $J_3 = k_s C_s$

J_1 is the flux of the oxidant from the gas to the vicinity of the outer surface of the silicon oxide, i.e it gives the absorption of oxygen at the silicon oxide surface. k is the coefficient describing this oxygen absorption rate. C^* is the equilibrium concentration of the oxidant in the surrounding gas atmosphere. C_0 is the concentration of oxidants at the oxide surface.
J_2 is the flux of oxygen in the oxide layer. D is the oxidant diffusivity in the oxide. C_s is the oxidant concentration at the oxide-silicon interface.
J_3 is the flux determining the oxidation rate of the Si at the Si/SiO_2 interface and k_s is the constant describing the oxidation rate. In the mass conservation (atom number conservation) regime, there is no accumulation of oxygen and the three fluxes are equal ($J = J_1 = J_2 = J_3$). Assuming that the physical constants k, D and k_s are known, there are thus 6 equations with 8 unknown : C^*, C_0, C_s, x, J_1, J_2, J_3 and J. So each of

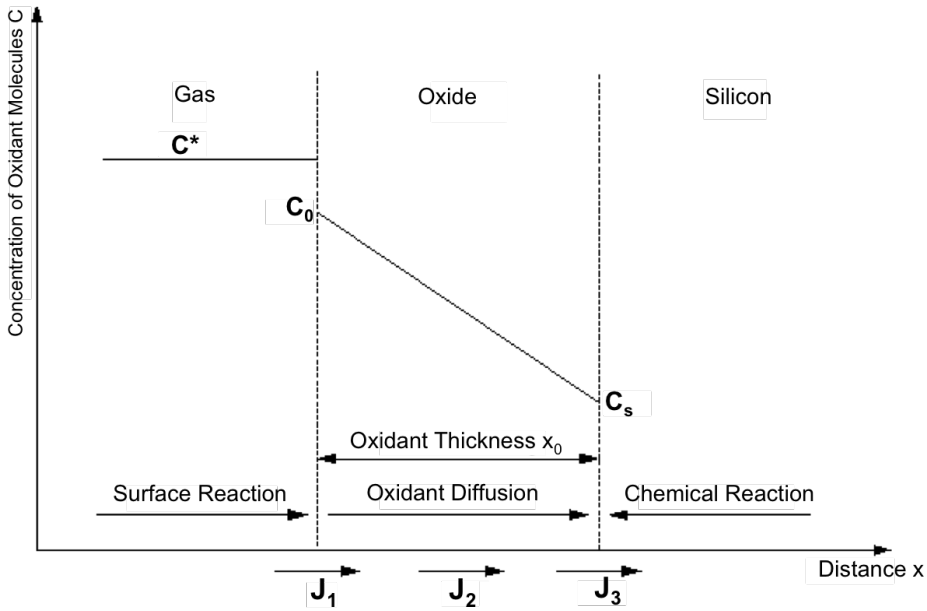

FIGURE 2.10: One-dimensional model for the oxidation of silicon. [7]

this 8 unknowns can be written in function of only 2 given unknowns. For instance, the flux J can be obtained as a function of C^* and x (see Eq.(2.12)).

$$J = \frac{C^*}{\frac{1}{k_s} + \frac{1}{k} + \frac{x}{D}} \tag{2.12}$$

In addition, as the incoming oxide is creating a new SiO_2 layer, there is a relation between the oxide thickness x and the oxidant flux.

If N is the number of oxidant molecules contained in a unit volume of the oxide layer, during the time dt, in the created oxide volume Sdx with S being an arbitrary surface perpendicular to the x-axis, there will be $N \times$ dx $\times$ S oxidant molecules. This number should be equal to the number of incoming oxidant molecules which is equal to $J \times$ dt $\times$ S. So we obtain eq (2.13).

$$\frac{dx}{dt} = \frac{J}{N} = \frac{\frac{C^*}{N}}{\frac{1}{k_s} + \frac{1}{k} + \frac{x}{D}} \tag{2.13}$$

This differential equation (2.13) was simplified and written as :

$$\frac{dx}{dt} = \frac{B}{A + 2x} \quad \text{with} \quad B = 2D\frac{C^*}{N} \quad \text{and} \quad A = 2D(\frac{1}{k_s} + \frac{1}{h}) \tag{2.14}$$

The Eq.(2.14) was analytically solved to relate the oxide thickness x to the oxidation time t :

$$x = \frac{A}{2}(\sqrt{1+\frac{4B}{A^2}(t+\tau)}-1) \quad \text{with} \quad \tau = \frac{x_0^2 + Ax_0}{B} \tag{2.15}$$

τ takes into account any oxide thickness at the start of the oxidation; x_0 is the reacted length at $t = 0$.

So if x_0 is taken as the origin of the x-axis, one has :

$$x = (\sqrt{\frac{A}{4}+Bt}-\frac{A}{2}) \tag{2.16}$$

Two limiting cases can be distinguished.

$$\text{When} \quad t >> \frac{A^2}{4B} \quad x \sim \sqrt{B.t} \quad \text{This is the parabolic regime.} \tag{2.17}$$

$$\text{When} \quad t << \frac{A^2}{4B} \quad \Longrightarrow \quad x \sim \frac{B}{A}t \quad \text{This is the linear regime.} \tag{2.18}$$

The rate constants B and B/A are known as the Deal-Grove parameters. These parameters are determined by fitting the experimental growth data. As C^* and N are known, B and B/A allow to determine the physical constants D and a mixture of k_s and k.

The weakness of the model is its impossibility to predict the initial stage of the oxidation growth as it is assuming a steady state regime.

In the next parts, we recall how the Deal and Grove equations have been applied to study the kinetics of the solid-state reaction occurring either in thin-films or in nanowires systems.

2.5.5 Application to Thin-films

Nemouchi et al [58] applied a modified Deal and Groves model to study the Ni/Si solid-state reaction of a Si subtrate. They used the chemical potential, instead of the concentration, as the driving force of the reaction. The Ni/Si solid-state reaction was triggered by heating and monitored by Differential Scanning Calorimetry (DSC) and X-Ray Diffraction (XRD). A sequential phase formation was observed : first a Ni-rich phase (Ni_2Si) was created, followed by the NiSi phase. By increasing the temperature a Si-rich ($NiSi_2$) phase was formed. They limited their study to fit and explain the kinetic data during the Ni_2Si growth where the linear-parabolic model appeared to provide a good fit to the data.

- Instead of working with the concentration gradient as the driving force, the fluxes were written as a function of the chemical potential.
- The model was limited to two limiting fluxes instead of three.

Therefore, the fluxes considered below that appeared to control the silicide growth rate are written as :

$$J_1 = D\,\frac{\mu_2 - \mu_1}{L}$$

Which describes the diffusion of Ni atoms across the growing Ni_2Si phase. D is the interdiffusion coefficient, L the thickness of the Ni_2Si film, μ_1 and μ_2 are the chemical potential of Ni, respectively, at the Ni/Ni_2Si interface and at the Ni_2Si/Si interface in the Ni_2Si film. A second flux controlling the growth rate is the interfacial reaction and can be written as :

$$J_2 = K\,(\mu_3 - \mu_2)$$

K is the interfacial rate constant and (μ_3 - μ_2) the difference in chemical potential at the moving interface.
The same assumption as above results in the Deal and Grove model written as function of the chemical potential :

$$\frac{dL}{dt} = \frac{KD}{KL+D}\,\frac{\mu_3 - \mu_1}{k_B T} \tag{2.19}$$

2.5.6 Application to Nanowires

The equation (2.19) was used in [22] to fit the kinetic data resulting from a solid-state reaction between Si NWs in contact to Au, Cu and Ni. The growth rate of the formed phases was triggered in-situ in a TEM using a heating TEM sample holder where the samples were heated up to 900°C. A linear-parabolic growth law similar to [58] was used to fit the evolution of the interface front as function of time in [22]. However, the Eq.(2.19) has been simplified and the term ($\frac{\mu_3-\mu_1}{k_B T}$) was neglected. It must be noted that the chemical potential in such systems is not generally known and experimentally accessible and even more so in NW systems. The growth rate of the different formed phases were found to be limited by a parabolic growth law for each of the three different metals (Au, Cu and Ni).
Several papers [24, 25, 41, 59] have used the Deal and Grove model in nanowire studies. For example, in Chen et al [59], the Ni/Si NW solid-state reaction was kinetically studied and the linear-parabolic growth law was found to control the silicide growth

rate. In [22], similar to [58], the mass transport and the reaction at the interface (silicide/Si NW) were considered to be the rate limiting step for the silicide growth rate and the concentration gradient was considered as the driving force.
Moreover, in Yaish et al [24], the silicide growth rate was modelled based on the original Deal and Grove model taking in account the influence of the NW radius deduced from experimental data in [24, 60, 61]. The same observation was reported in [25], where the influence of the NW radius was also observed and integrated in a similar model. The difference between [24] and [25] is the approach, where in [24] the mass transport through the silicide segment is considered to result from a pure surface diffusion whereas in [25] volume diffusion was not excluded in addition to surface diffusion. They used equations describing diffusion through a crystal with grain boundaries, considering grain boundary diffusion equal to surface diffusion. This approach was also presented by [23] where they formulated the interdiffusion coefficient as a sum of the volume diffusion coefficient and a surface diffusion coefficient, including g, an aspect ratio coefficient for the NW.

$$D_{measured} = D_B + gD_S \tag{2.20}$$

with D_B the volume diffusion coefficient, D_S the surface diffusion coefficient and g the aspect ratio of the NW.
As discussed above, in the NW geometry surface diffusion is generally observed. Papers [24, 25, 41, 59] on the topic all show a strong contribution of surface diffusion to the reaction, where the silicide phase was formed in NWs with different radii. For a decrease in the NW radius an increase of the silicide propagation speed was observed. However these papers can not exclude nor proof a small additional component due to volume diffusion.
Tang et al [41] made a nice review of the different studies realized on Ni/Si and Ni/Ge NWs. The authors established a kinetic model where they take into account all the factors that have been reported to influence the silicide or germanide growth rate and the former kinetic models. In all these models, Ni was considered as the only diffusing species during the formation of the silicide phases and this was used to explain the kinetic data from the Ni/Si NW solid-state reaction at different temperatures.

To conclude this part, the different models were established in a way to fit the resulting data found in each experiment. However, all the models, as mentioned above, rely on the same potential limiting steps that have been experimentally demonstrated to limit the silicide growth rate. One can observe that the models in [22, 24, 25, 41, 59]

are established based on Deal and Grove model certainly in different manners but they keep the same assumptions on which the model relies.

2.5.7 Model applied to NWs used in this Phd

At the end of this chapter, instead of presenting the Tang et al [41] model, which is an extension of the Deal and Grove model to Si NWs, we prefer to directly translate the Deal and Grove to what we have studied. So we present hereafter the extension of the Deal and Grove model to the diffusion and reaction of metal atoms with Ge nanowires. In this PhD work, the metal atoms will be either Cu (chapter 6) or Al (chapter 7).

Fig.(2.11) is a typical system that we have realized and studied. A metal contact has been deposited on the middle of a Ge NW deposited on a thin membrane. Details of the fabrication of these devices are given in chapter 3. As shown, in Fig. (2.11), due to geometrical constraints, the deposited metal does not surround the NW but covers the NW over a surface $2S_1$ which includes about half of the NW radius that is to say, $S_1 \sim \pi R L_1$, where h is the thickness of the deposited metal, $2L_1$ the length of the deposited contact along the axial direction of the NW and R is the radius of the NW.

Then the structure is heated in-situ in a TEM microscope in order to form a germanide phase, noted G in Fig.(2.11). During heating, the Cu atoms diffuse in the NW creating a germanide phase that extends on both sides of the NW. In the following we focus on the right part of the scheme, noting L the length of the formed germanide phase. We can distinguish three steps in the reaction:

1. The incorporation of metal atoms in the germanide phase at the reservoir/germanide interface
2. The diffusion from the reservoir/germanide interface to the germanide/Ge interface.
3. The reaction of the metal atoms with the Ge atoms at the germanide/Ge interface

So our model does not account for self-diffusion within the metal contacts. This diffusion is supposed to be very fast and supposed to have no effect on the propagation of the germanide/Ge growth front. The concentration gradient is also the driving force governing the metal atom transport. Let us examine each step in turn.

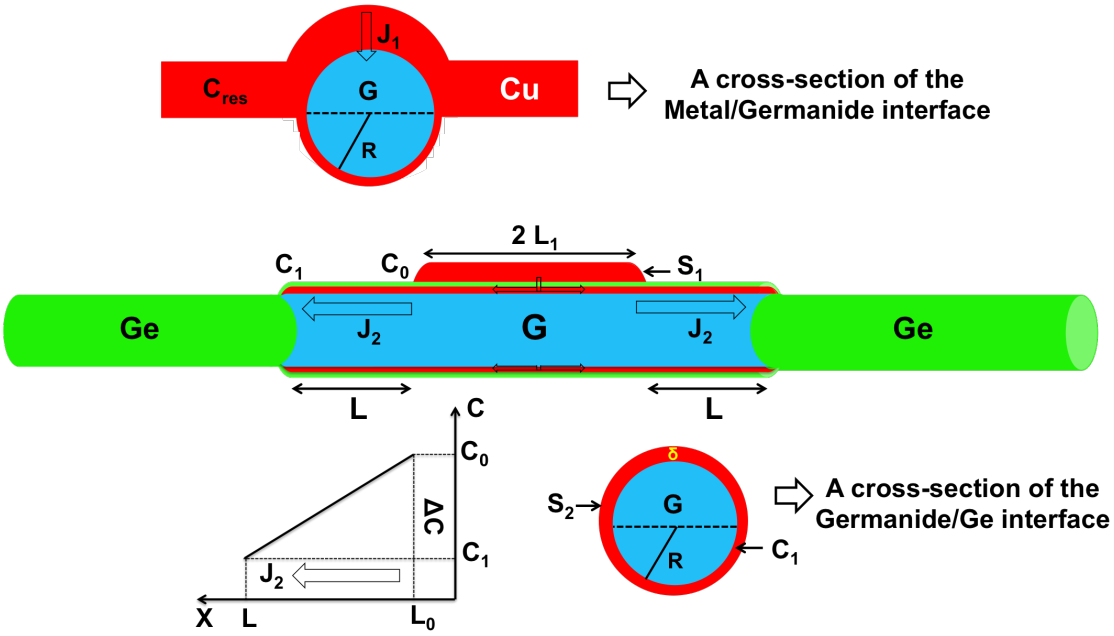

FIGURE 2.11: Schematic model for Cu germanide growth process during thermal annealing.

1. Incorportation of Metal in the germanide phase at the reservoir/germanide interface :

   Different studies reported an influence of the reservoir/germanide interface quality on the growth rate. Therefore, this parameter needs to be taken into account in order to determine the limiting step of the propagation growth rate. As done for the Deal and Grove model in the steady state regime, the flux of incorporated atoms is given by :

$$J_1 = k_1(C_{res} - C_0) \tag{2.21}$$

   where k_1 is the incorporation rate constant of metal atoms in the germanide phase. C_{res} and C_0 represent the local concentration of Cu atoms in the Cu reservoir - this is normally a known value, as was C^* in the Deal and Grove model - and Cu/germanide interface, respectively.

During the time dt, the number dN_1 of incorporated metal atoms in the germanide phase, is equal to :

$$dN_1 = I_1 dt = J_1 S_1 dt = k_1 (C_{res} - C_0)\pi R L_1 dt \tag{2.22}$$

where I_1 is the metal incorporation rate.

2. Diffusion through the germanide segment : The next step governing the germanide propagation, is the diffusion of dissolved atoms through the germanide segment to the germanide/Ge interface. As, we consider two diffusion paths, the total transport rate of metal atoms I_2, will include two terms, one due to volume diffusion I_2^v and one due to surface diffusion I_2^s.

$$I_2^v = J_2^v . S_2^v = D^v \frac{C_0 - C_1}{L} . S_2^v \quad \text{with} \quad S_2^v = \pi R^2 \tag{2.23}$$

$$I_2^s = J_2^s . S_2^s = D^s \frac{C_0 - C_1}{L} . S_2^s \quad \text{with} \quad S_2^s = 2\pi\delta R \tag{2.24}$$

So during the time dt, the number dN_2 of metal atoms diffusing in or on the germanide segment is given by :

$$dN_2 = \pi R (2\, D_2^s \delta + D_2^v R) \frac{C_0 - C_1}{L} dt \tag{2.25}$$

D^s is the diffusion coefficient (cm^2/s) of Cu atoms through the surface segment to the germanide/Ge NW interface. C_1 is the local concentration of Cu atoms at the germanide/Ge NW interface, L is the segment length and δ is the thickness of the surface layer where the Cu atoms diffuse through.

3. The reaction of the metal atoms with the Ge atoms at the germanide/Ge interface. With notations similar to the first step, during the time dt, dN_3 the number of metal atoms reacting at the germanide/Ge interface is equal to :

$$dN_3 = I_3 dt = J_3 S_3 dt = k_3 C_0 \pi R^2 dt \tag{2.26}$$

as we suppose that there is no Cu in the Ge section of the NW. These atoms create a thickness dL of germanide. If N is the number of metal atoms contained in a unit cell of germanide, the volume $S_3 dL$ contains $N S_3 dL = dN_3$ atoms. So we have the equation :

$$N dL \pi R^2 = I_3 dt \tag{2.27}$$

In steady state conditions and without accumulation of metal atoms in the system, all the atom currents i.e. intensities are equal ($I = I_1 = I_2 = I_3$), and similarly as in the Deal Grove model, the intensity I can be expressed as a function of C_{res} to obtain an equation depending on L:

$$I = \frac{\pi R C_{res}}{\frac{1}{k_1 L_1} + \frac{L}{2D^s\delta + D^v R} + \frac{1}{R k_3}} \tag{2.28}$$

$$\frac{dL}{dt} = \frac{I}{N\pi R^2} \tag{2.29}$$

Replacing I in this last equation, one obtains a differential equation in L similar to the one obtained in the Deal and Grove model.

$$\frac{dL}{dt} = \frac{\frac{C_{res}}{N}}{\frac{R}{k_1 L_1} + \frac{L}{2D^s\frac{\delta}{R} + D^v} + \frac{1}{k_3}} = \frac{B}{A + 2L} \tag{2.30}$$

Where $B = 2(2D^s\frac{\delta}{R} + D^v)\frac{C_{res}}{N}$ and $A = 2(2D^s\frac{\delta}{R} + D^v)(\frac{1}{k_1 L_1} + \frac{1}{R k_3})$

So, similar to the Deal and Grove model, there would be two limiting case. For a short reaction duration, the length of the germanide segment is small and the metal diffusion on this segment is small; in this regime L varies linearly with time. For a very long reaction duration, the length of the germanide segment is so long that the metal diffusion on this segment is the dominant factor; in this regime L varies as a square root of time, this is the so called diffusion limited regime. The big difference with the original Deal and Grove model is that now the variables A and B are a function of the NW radius R. Tang et al [41] defined several growth regimes depending on the values of the physical constant k_1, D^v, D^s and k_3 values. In fact the different regimes can be more easily understood by looking at equation (2.30).

If the incorporation of metal atoms at the reservoir/germanide interface is the limiting factor, k_1 will be very small and it will be the main factor in Eq.(2.30) . L will vary linearly with time and will vary as R^{-1}.

If the reaction at the germanide/Ge interface is the limiting factor, the reaction at this interface will be very slow and the reaction constant k_3 will be very small compared to the other physical constant and it will be the main factor in Eq.(2.30) and L will vary linearly with time and L will not be a function of R.

TABLE 2.4: Summary of the different regimes governing the germanide phase propagation deduced from Eq.(2.30).

Germanide growth regimes	L
Metal reservoir limited (t « $\frac{A^2}{2B}$)	$\sim R^{-1}t$
Interfacial reaction limited (t « $\frac{A^2}{2B}$)	$\sim t$ (Independent of R)
Volume diffusion limited (t » $\frac{A^2}{2B}$)	$\sim \sqrt{t}$ (Independent of R)
Surface diffusion limited (t » $\frac{A^2}{2B}$)	$\sim (\sqrt{\frac{t}{R}})$

If the diffusion along the germanide section is the limiting factor, the dominant factor in Eq.(2.30) will be the term dependent on L. So when solving Eq.(2.30), L will vary as a square root as a function of time. If its volume diffusion, L will be independent of the NW radius R, if it is a surface diffusion L will vary as a function of R^{-1}. These different regimes are summarized in table (2.4).

Chapter 3

Samples

In this chapter the different steps followed to achieve the different samples studied in this thesis are described. Firstly, the method for NW growth is briefly described. Secondly, the protocol followed in order to achieve reliable devices for in-situ TEM experiments is presented. The prepared device needs to be mounted on a sample with a thickness < 100 nm to be electron transparent and obtain sufficient image quality. The protocol followed in order to achieve reliable samples is based on conventional cleanroom fabrication techniques.

3.1 Nanowire Growth

The nanowires used in this thesis were undoped Si and Ge NWs, grown in the SiNaPS laboratory in Cea-Grenoble and in the Technical university of Vienna in Austria. The growth was done following a bottom up approach.
The bottom up approach consists of the formation of NWs starting from individual atoms that are supplied by a precursor material through a Chemical Vapor Deposition (CVD) mechanism [62]. This mechanism, which is characterized by a molecular precursor that decomposes at the catalyst surface to supply the atoms to form a nanowire, is used in most cases via the vapor liquid solid (VLS) mechanism (see Fig.(3.1)) where the precursor is supplied as a gas. The formation of Ge nanowires by the VLS mechanism is possible at low temperature by the deep Ge-Au eutectic at (640°C). The catalyst used for the growth was a gold colloid solution.
For the VLS mechanism gold colloids (or a gold layer) are deposited on a Si (111) substrate. Typically, the substrate is cleaned prior to catalyst deposition to remove

the native oxide. Then the substrate is heated beyond the eutectic temperature to remove the capping of the colloids. Either silane (SiH_4) gas for Si NW growth or germane (GeH_4) gas for Ge NWs growth is introduced in the reaction chamber. The gas reacts with the gold catalysts and the silane or germane decomposes at the catalyst allowing an incorporation of the silicon or germanium atoms in the liquid catalyst. Once the supersaturation is reached, the semiconducting atoms nucleate at the substrate below the catalyst and the growth starts.
These resulting 1D structures combine high crystalline quality with good controllability of both length and diameter.

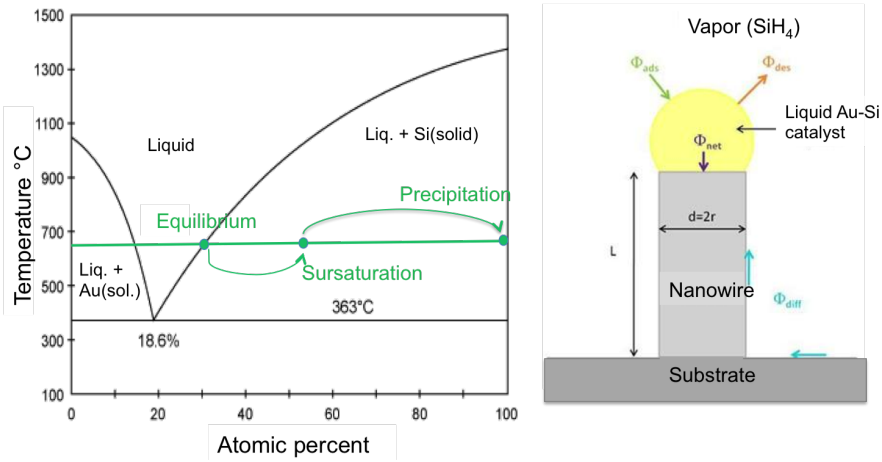

FIGURE 3.1: Illustration of the vapor liquid solid (VLS) growth process of Si NWs. The same process describes the Ge NW growth. The VLS growth mechanism consists of three different steps: 1) Incorporation and enrichment of the Au-Si droplet by Si atoms. 2) Supersaturation of the droplets by Si. 3) Precipitation of Si atoms at the liquid/solid interface and growth of the monocrystalline nanowire.[8]

3.2 Sample Preparation

Many efforts were deployed to find a good and reproducible protocol making reliable in-situ devices [63]. Therefore the different steps presented below need to be followed. For this purpose, we used lithographic techniques extensively which allow the patterning of custom designed contact electrodes.

3.2.1 Membrane Fabrication

To perform conventional TEM analysis, Cu grids with thin carbon foil (20 - 30 nm) are commonly used, where the sample is deposited on the TEM grid for TEM observation. However, these conventional substrates cannot support sample fabrication for advanced in-situ experiments (biasing or liquid). Therefore, we used silicon nitride membranes as they are compatible with lithography to electrically contact nano-objects. In the following, we show the different steps used for the homemade membrane fabrication. Additionally, commercial heater chips from DENsSolution [12] were used in our experiments and dispersed NWs were lithographically contacted on these chips.
The membrane fabrication was achieved using optical lithography in a UV-KUB equipped with UV-LED system, allowing to expose large areas (4 inch wafers). An array of silicon nitride membranes was made starting from a 300 μm thick Si (100) 4" wafer with a 50 nm thick layer of stoichiometric Si_3N_4 on each side deposited by low-pressure chemical vapor deposition.
The process starts by a plasma cleaning of the 4” wafer. Then a negative resist (MaN420) was spin coated on the substrate for 30 sec at 3000 rpm and subsequently baked at 95° for 150 sec. Then, the resist layer was exposed to radiation in the UV-KUB. After the exposure, the sample was developed in a chemical base called MaD332/S for 2 min (removing the resist from the unexposed areas) followed by 1 min rinse in deionized (DI) water. The substrate is then gently blown dry with a nitrogen flow. An SF_6 plasma was used to etch the Si_3N_4 layer on each of the patterned windows and a sequential etch of the 300 μm silicon was done in a KOH bath at 80°C for several hours, until the other Si_3N_4 layer was reached. The so-defined membrane arrays were cleaned in 65% HNO_3 at 80°C for 1 h. The 4” wafer was cleaved to small pieces (20 × 20 mm) and glued on a silicon support for the following lithography steps. Fig.(3.2) describes the membranes fabrication.

3.2.2 Optical Lithography of Large Contacts

Once the Si_3N_4 membranes were prepared, we pattern small markers on the membrane and metal contacts around the membranes to ensure that the sample can be connected to the external environment (see Fig.(3.4)). To this end, large contacts were defined by laser lithography allowing to connect single membranes to the TEM sample holder used for in-situ TEM experiments (more details are described in the

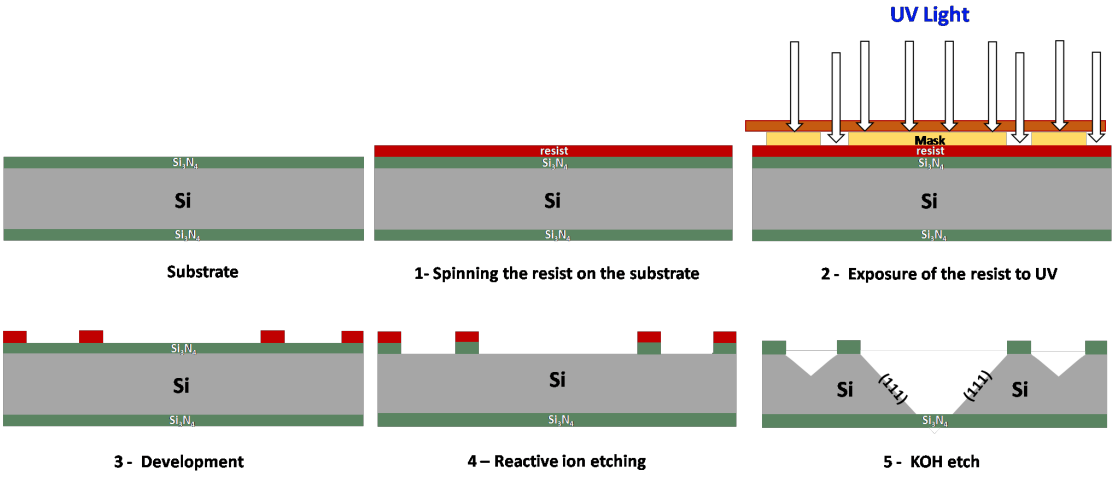

FIGURE 3.2: Illustration of the UV lithography process for the membrane fabrication. 2) The layer of resist is exposed to an UV-LED (optical lithography) using a mask (metal on quartz). The development 3) in a suitable solution removes resist in the unexposed areas. 4) Reactive ion etching using SF_6 plasma to remove the silicon nitride layer. 5) Silicon etch in KOH along the Si (111) planes to open the membrane window.

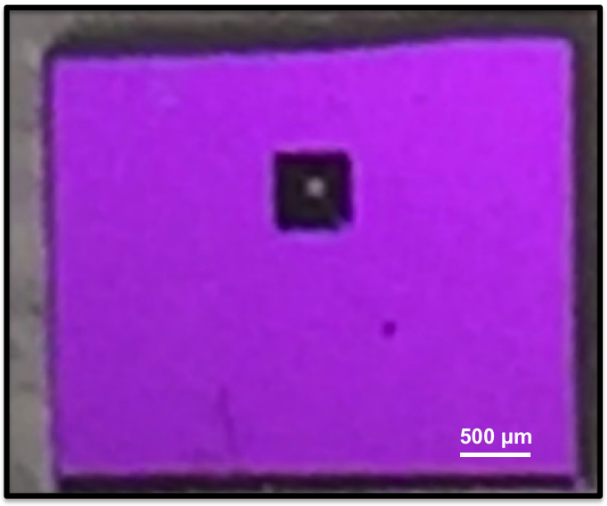

FIGURE 3.3: Photograph of the lithography side during the membrane fabrication after KOH etching.

following sections).

The choice of optical rather than e-beam lithography in this fabrication step is due to the patterning time because optical lithography is faster than e-beam. Thus, two positive photoresists, LOR-3A and S1805, from Shipley were subsequently spin coated on the substrate:

- **LOR-3A** was spin coated at 6000 rpm, 4000 rpm/s for 30 sec and baked at 200°C for 2 min.

- **S-1805** was spin coated at 6000 rpm, 4000 rpm/s for 30 sec and baked at 115°C for 1 min.

After the exposure, the sample was developed in a chemical base called MF-26A for 1 min (removing the resist from the exposed areas) followed by 1 min rinse in DI water and the substrate was gently blown dry with a nitrogen flow. A metal deposition was performed by e-beam evaporation where two metal layers (Ti (10 nm)/ Au (50 nm)) were deposited. The Ti layer was used to allow a better adherence between the deposited gold (Au) layer and the Si_3N_4 substrate. After metal deposition a lift off process is performed where the sample is put in remover PG heated at 80°C for several hours to remove the resist and metal on the resist from the substrate, see Fig.(3.5).

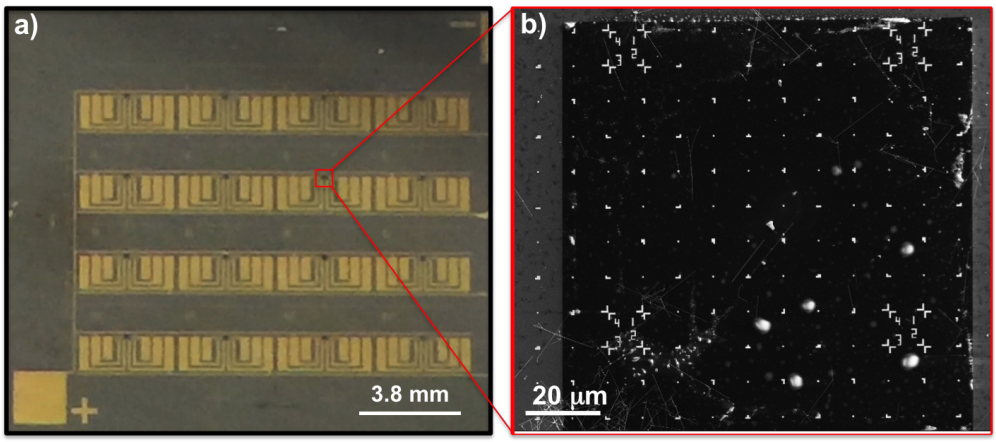

FIGURE 3.4: a) Photograph of the patterned large contacts made by laser lithography. b) SEM image of the small markers on a single membrane, where the NWs are dispersed on the silicon nitride membrane.

3.2.3 E-beam Lithography to Contact NWs

We have now obtained membranes patterned with small markers and large contacts. NWs were dispersed in ethanol using ultrasound and the solution was drop casted on the membranes with the aid of a micropipette to disperse the NWs. The solution was evaporated on a hot plate at moderate temperature or by blow drying with a nitrogen flow. These NWs are located and imaged by a Scanning Electron Microscope (SEM) with respect to the markers. We import the images in the Klayout software where we superpose the images to the marker pattern. Two parallel lines are defined on each side of a NW and connected to the large contacts. The width of the stripline is

around 500 nm at the NW extremity and becomes gradually wider towards the large contacts. These parallel lines are written using e-beam lithography and used as metal reservoirs for the solid-state reaction as well as electrical contacts. The different samples presented in this thesis were processed either in Vienna in Prof. Alois Lugstein groups or in our lab in Grenoble. However, fabrication processes used in the different labs are similar, the only difference is in the used instruments.
A polymethyl methacrylate (PMMA) 4% was spin coated on the substrate for 60 sec at 4000 rpm and subsequently baked at 180°C for 5 min, followed by a PMMA 2% resist using the same parameters. After the electron beam exposure the substrate is developed in a solution of (methyl-isobutyl-ketone (MIBK): Isopropyl-alcohol (IPA)) (1 : 3) for 30 sec followed by a final 30 sec rinse in IPA. The substrate is blown dry with nitrogen flow. Prior to the metal deposition step, the substrate is dipped in a diluted [HI:H_2O][1:7] for 5 sec and rinsed with DI water and dried under N_2 flow to remove the native oxide on the Ge NW surface at the contact region. A metallization of the substrate to fill the defined strip lines was made either by e-beam evaporation in the Cu/Ge NW samples or by both sputtering and e-beam evaporation in the Al/Ge NW samples. Finally, the substrate is placed in acetone for the lift off until the metal is removed from the unexposed parts. This process can be facilitated by agitating the solution using a pipette. The procedure is shown schematically in Fig.(3.5).
After separating the different chips from each other by cleaving along defined cleaving lines (see Fig.(3.2)), the sample is ready for the in-situ TEM experiments as shown in the Fig.(3.6).

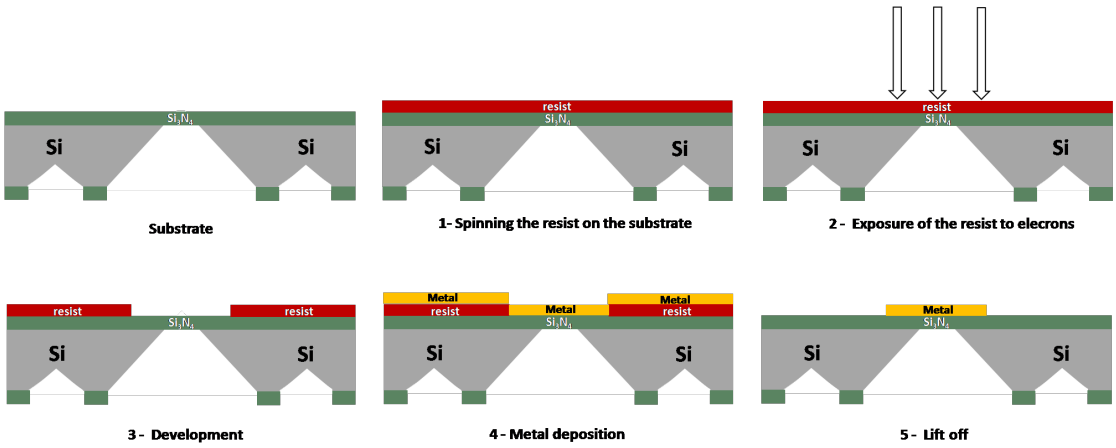

FIGURE 3.5: Illustration of the process followed in both laser and electron beam lithography.

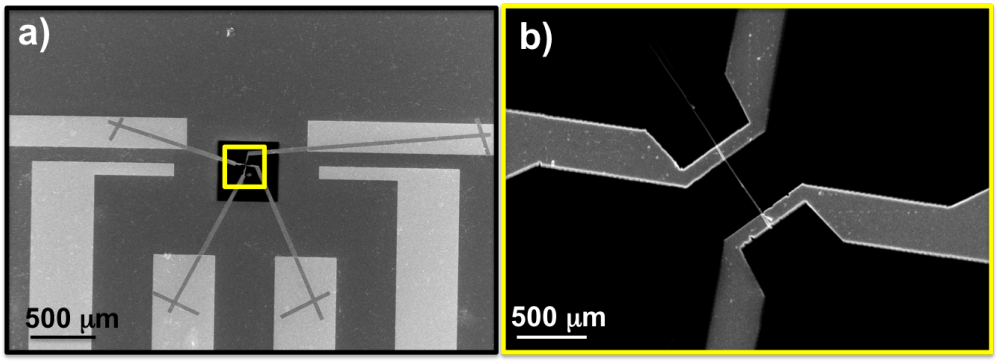

FIGURE 3.6: a) SEM images of NWs contacted by e-beam lithography. b) Large contacts defined by laser lithography are also visible.

As already mentioned above, we also used commercial membranes calibrated in temperature, where a buried heating spiral in a SiN membrane is heated by Joule heating. We dispersed Ge NWs (same process as defined above) on 20 nm thick Si_3N_4 windows (see Fig.(3.7)). These NWs were contacted on one side with a metal strip line, providing a metal reservoir using the same lithography process as defined above.

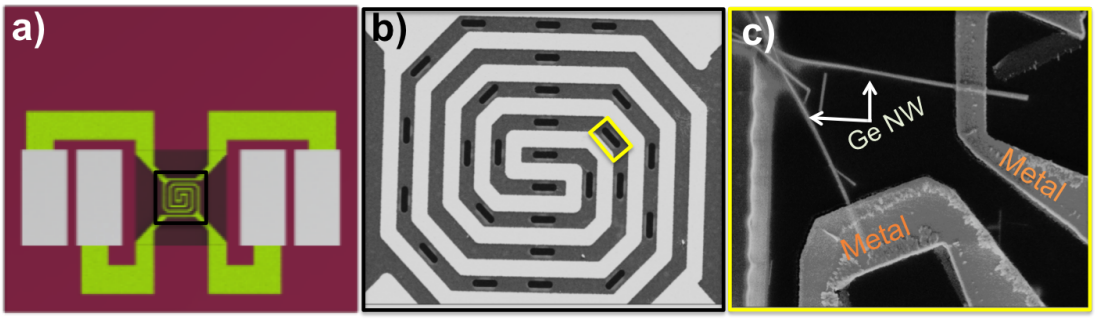

FIGURE 3.7: a) Photograph of microfabricated commercial membrane from DENSsolutions calibrated in temperature and used during H_b heating experiments. b) SEM image showing a Mo spiral buried in two SiN layers with different windows spanned with 20 nm thick Si_3N_4 layer for electron transparency. c) SEM image on a window showing an electron lithography contacted Ge NW by a Cu metal.

Chapter 4

Electron Microscopy

In this chapter we present briefly the different electron microscopy instruments and techniques used during the experiments presented in this work. Our aim is to recall the characteristics of the different techniques used in transmission electron microscopy that provide information which allows a better understanding of the phenomena occurring during our heating experiments. The source that provided most of the following information on those techniques is William and Carter's book [64]). Transmission electron microscopy analyses were performed in the Plateforme de Nanocaractérisation - Cea (PFNC) and in-situ TEM experiments and part of the electron diffraction studies were performed in Néel Institut in Grenoble.

4.1 Transmission Electron Microscope

Electron microscopes were used and developed in order to attend a resolution beyond the resolution limit of light microscopes. De Broglie (1925) theorized the electron wave-like characteristics with a wavelength shorter than visible light, since the spatial resolution δ depends on the wavelength λ according to the Rayleigh criterion, given approximately as :

$$\delta = \frac{0.61\lambda}{\mu sin\beta} \tag{4.1}$$

Where μ is the refractive index of the viewing medium and β is the semi-angle of collection of the magnifying lens. Therefore, electron microscopes are the alternative to reach higher spatial resolution. A couple of years after the demonstration of the electron wave nature, a first electron microscope was presented in Knoll and Ruska's

paper (1932) where they developed the idea of building an instrument that allows to acquire electron images. Many studies came afterwards developing the instrument, especially when transmission electron microscopes started to be commercialized. Nowadays the transmission electron microscope is one of the most used instruments in material characterization not only for the better spatial resolution but also for the structural, chemical, electrical and magnetic information provided by the electron-specimen interactions [65].

The electrons passing through the sample are scattered either by the electrons or by the atomic core. We can distinguish two scattering processes: *elastic* scattering (no loss of electron energy after scattering) and *inelastic* scattering (a loss of electron energy). If the electrons are scattered in a particular direction this is called diffraction, which is both due to the wave-like nature of the electrons, their coherence and the periodic spacings present in the crystal [65]. If we ignore relativistic effects, the wavelength can be expressed (ignoring the inconsistency in units):

$$\lambda \sim \frac{1.22}{E^{0.5}} \tag{4.2}$$

In this equation E is in eV and λ in nm. So from eq.(4.2) we can work out that by increasing the acceleration voltage the wavelength will decrease. For some time the tendency in TEM development was to increase the acceleration voltage to increase spatial resolution. Indeed an increase of acceleration voltage reduces the wavelength of the electron and thereby we gain in spatial resolution. However, bombarding samples by electrons with high energy can cause a lot of damage. For example, knock-on damage (this phenomenon occurs when we provide enough energy to knock an atom off is lattice site) occurs in silicon at and above 150 kV [66]. Also, the acceleration voltage becomes unstable at high acceleration voltages around and above 1 MeV, which degrades the resolution due to the chromatical aberrations of the lens system [65]. Lens aberrations have a very strong effect on the resolution and for this reason the spatial resolution that we can obtain is at present not limited by the Rayleigh criterion but limited by lens aberrations. Therefore, another approach was initiated to improve the resolution limit which is based on correction of the different lens aberrations in the TEM. Electron lenses suffer from two main aberrations: chromatic and spherical aberration. Chromatic aberration appears in an electromagnetic lens by a change of its focal point for different electron wavelengths [65]. To reduce the spread of the electron wavelength, an energy filter can be introduced, limiting this aberration. Spherical aberration is a change in the focal point for the electrons traversing

the electromagnetic lens either in the center or near the edge [65]. To limit this aberration a corrector was designed allowing to reach an ultimate resolution limit down to 0.5 Å operating at 300 kV.
Nowadays a new generation of electron microscopes equipped with these correctors are commercialized and the trend now is to operate these microscopes at lower voltages, keeping an atomic spatial resolution due effectively to these correctors. This allows to decrease the specimen damage, and therefore, increase the spectrum of TEM applications to beam sensitive material and life science.

4.1.1 Principle Components of the Transmission Electron Microscope

In conventional TEM different pieces mounted in a particular architecture allow to acquire sample images with a high spatial resolution. All TEM microscopes are equipped with an electron gun. There are two different electron sources: a thermionic source which emits electrons when heated and a field-emission source emitting electrons when an intense electric field is applied to it. Tungsten and LaB_6 tips are two examples of a thermionic gun and a tungsten tip with a ZrO_2 reservoir is one of the tips used in a field-emission gun (FEG). The main difference between these types of guns is that FEGs are characterized by a higher brightness and a small spot size because electrons are emitted from a very small region on the tip, contrary to a thermionic LaB_6 tip. However, LaB_6 guns are still commonly used as they are cheaper than a FEG tip. The electron beam is produced by the gun and then accelerated by a potential difference between an anode and a Wehnelt, which is a cylinder just after the electron source that is charged negatively (cathode). This difference of tension determines the accelerating voltage of the electrons. The beam is directed through the column by electromagnetic lenses which behave like a thin lens in geometrical optics. The electromagnetic lenses consist of coils which permit to deflect beam electrons by applying an electromagnetic field created by a current. The TEM is composed of several lenses. Most important are the condenser lenses that form the electron probe to pass trough the sample and the objective lens that is directly behind. Samples need to be transparent to electrons with a thickness $\leq$ 100 nm. The objective lens and the sample are so close that this latter is actually in the magnetic field of the objective lens and this limits the study of magnetic samples. The objective lens is the lens that deals with a large amount of entering electrons over a large range of angles and its

the part of the instrument where the image of the sample is created. Therefore, its aberrations (chromatic and spheric) determine the instrument resolution [65]. A series of projector lenses follows the objective lens that allow to magnify the resulting image projected on a phosphor screen or on a CCD camera where the image can be recorded. There are also apertures in the column which allow selecting a part of the beam. The condenser aperture controls the illumination of the sample, the objective aperture placed in the back focal plane of the objective lens gives contrast to the image (bright field, dark field or high resolution) by selecting a region in reciprocal space and the selected area aperture placed in the image plane of the objective lens allows to select a specific area of the sample to obtain a diffraction pattern only of the selected region. Electrons interact with matter, so to protect the system and avoid contamination of the specimen, a vacuum is created in the TEM by incorporating several pumps at different locations in the TEM column.
This assembly of lenses is used in all TEM instruments, however, different ways of using these lenses results in different kinds of images. When using a parallel beam, this results in a conventional TEM (CTEM) image, however, when forming a very punctual probe at the specimen plane and scanning this beam over each point of the sample, this results in a Scanning TEM (STEM) image. Most modern microscopes can be operated in both modes but also machines dedicated to one of the two modes are used [65].

4.2 Scanning Transmission Electron Microscopy

In STEM mode a small probe is created by the third condenser lens. The beam is raster scanned from left to right and top to bottom and the scattered electrons are collected by different detectors where the intensity on a detector is collected at each point to form the STEM image. Three STEM detection ranges are used for imaging : Bright Field (BF), Annular Dark Field (ADF) and a High Annular Dark Field (HAADF) detector. In BF images the direct beam is detected. In ADF the scattering angles are relatively low (angles between 10 and 40 mrad [64]). In BF and ADF contrast is formed both from mass-thickness variations and diffraction. For HAADF, the detector detects electrons deviated over large angles (angles > 40 mrad [64]) so that only inelastic electrons are detected and hence the intensity is very sensitive to the atomic

number Z as described by eq.(4.3).

$$I = mtZ^{\eta} \tag{4.3}$$

where m is a scaling constant, t is the sample thickness and η is a constant between $\sqrt{\frac{2}{3}}$ and 2. Therefore, heavy elements are distinguished from lighter ones. The advantage of the HAADF STEM technique with respect to other STEM or TEM techniques is the absence of any artefacts or contrast reversals in images, since in HAADF mode, we are interested only in inelastic electrons [64]. For enhancing the contrast of lighter elements, a quite new technique called annular BF (ABF) can be used. In ABF, the primary convergent beam electron diffraction (CBED) disk is magnified to cover the entire ADF detector which makes it a BF technique but without the elements of the central part of the beam. As such, it promotes imaging of both light and heavy elements. In a STEM instrument the spatial resolution that can be obtained is determined largely by the beam diameter generated by the probe-forming lens, which is also limited by aberrations. STEM and TEM modes are related by the principle of reciprocity that means that the same image acquired in BF STEM mode can be acquired in TEM mode under certain conditions.
It is also possible to use a narrow parallel probe with a size of few nm to produce diffraction patterns from nm sized regions. This technique is called nanobeam electron diffraction (NBED). NBED is a great tool to characterize nanoscale semiconducting devices [67, 68] because of the small size (~ 2 nm) of the parallel beam used in NBED, we can easily study diffraction patterns of small crystal regions. In STEM mode, the NBED diffraction patterns can be filtered by an electron energy loss spectrometer, where inelastically scattered electrons are removed before being acquired on the camera. From these diffraction patterns both structure and sample thickness can be determined.

4.3 Electron Energy Dispersive X-ray Spectroscopy

The characteristic X-ray energy reveals the chemical nature of the atom. In any interaction between the electron beam and the sample two types of X-rays are produced :

- Bremsstrahlung (which means 'braking radiation'): Bremsstrahlung X-rays are produced by slowing down of the primary beam electrons by the electric field

surrounding the nuclei of the atoms in the sample, this type of X-rays are referred to as background X-rays and bruit of the detection in material science characterisation [64].

- Characteristic X-rays : Once the inelastic transition has taken place, causing the fast electron to lose energy by producing a hole in the distribution of the atomic core electrons, the hole is healed by the transition of an outer electron into it. An X-ray and/or Auger electrons are produced.

The electron cloud gravitating around the nucleus is organized with a stable set of energy levels, also known as electron shells. The shell closest to the nucleus is known as the K shell, followed outwards by the L, M, N, O, P and Q shells. Energy dispersive X-ray (EDX) microanalysis is mostly concerned with electrons in the inner shells, i.e., the K, L and M shells. The maximum number of electrons in each shell is governed by quantum mechanics, with a maximum of 2 electrons in the K shell, 8 in L shell, 18 in M shell and so on. Each shell, apart from the K shell, is split into subshells, with the electrons in related subshells having slightly different energies. The L shell has three subshells, the M shell has five subshells, and so on. The K shell has the highest ionization energy or critical ionization energy in the atom. That is, more energy is needed to remove an electron from this shell than from subshells further from the nucleus. The further from the nucleus the electron is, the lower its ionization energy. Characteristic X-rays are produced by electron transitions between the electron shells. In spectroscopy, the most commonly used naming convention for characteristic X-ray lines is the Siegbahn notation. The first component of the name is the element involved, e.g. Si. The second component is the electron shell that was ionized to produce the X-ray, e.g. K, L or M. The third component reflects the relative intensity of the line within each shell, e.g. α is the most intense line, followed by β and γ. The lines within each shell make up a family, or series, of lines for that shell, e.g., the K family comprises the K_α and K_β X-ray lines. For each element, the electrons in the K shell have the highest ionization energies while the ionization energies of electrons in outer shells are lower. More energy is required to ionize the K shell, and it follows that the energies of the K family X-ray lines for each element are greater than those of the L family, which are greater than those of the M family. That is, for every element: $E_K > E_L > E_M$.
An energy dispersive X-ray spectrometer is placed near the sample collecting all the resulting X-rays and displays the signal as spectrum of intensity (X-ray energy spread

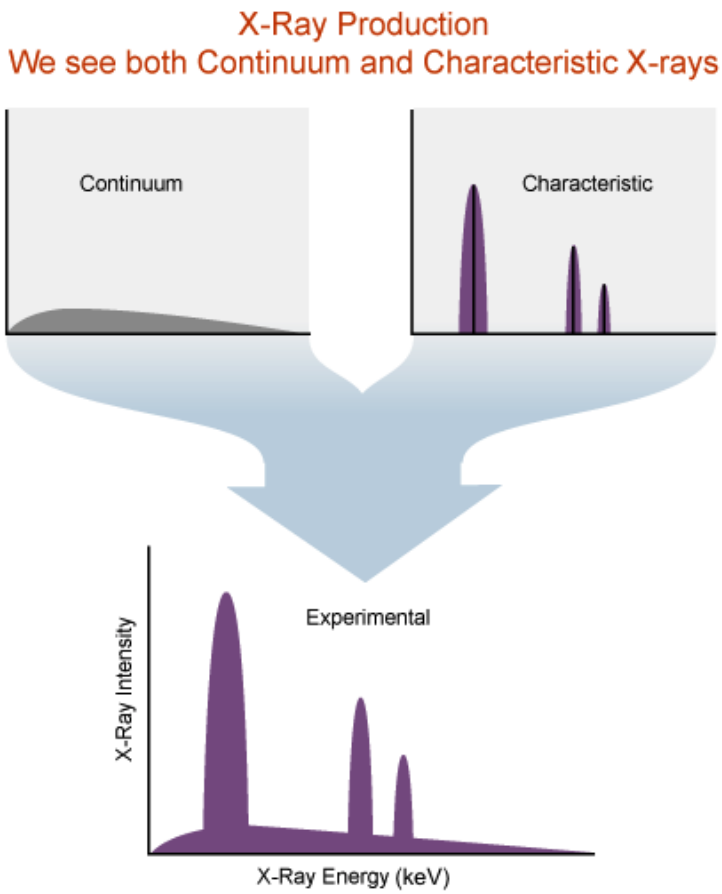

FIGURE 4.1: The X-ray spectrum displayed by the Energy Dispersive system comprises characteristic X-ray peaks superimposed on the continuum (Bremsstrahlung X-rays). [9].

versus number of X-rays). The experimental resulting spectrum is always represented by a superposition of both characteristic X-ray lines and Bremsstrahlung X-rays as seen in Fig.(4.1). The energy of the characteristic X-ray allow identifying the element, while the intensity allows quantifying the concentrations. The spectral resolution of a peak is defined as the width of the peak (in eV) measured at half of the peak height. This is known as the FWHM (full width at half maximum) resolution. The spectral resolution is determined by the acquisition time more longer it takes better the resolution will be.

Several artefacts can be produced in EDX spectra and need to be taken into account during the spectrum analysis. These artifacts are due either to the way that the X-rays were detected or processed. The three major artifacts are : the internal fluorescence peak, the escape peak and sum peaks.

- Internal Fluorescence : These X-rays are related to the material present in the

detector. For example in an Si detector, the X-rays coming into the detector can generate characteristic X-rays from the dead layer which is a layer surrounding the active region of the Si detector. These X-rays will appear in a small peak in the spectrum even if no Si is present in the characterized sample.

- Sum peaks : This artifact is produced when the pulse processor cannot distinguish between two X-rays that arrive almost simultaneously. Instead of recording two X-rays with either the same or different energies, one X-ray with energy equal to the sum of the energies of the two incoming X-rays is recorded and plotted in the spectrum.

- Escape peaks : This is produced when instead of all of the energy of an incoming X-ray being converted to electron-hole pairs, a Si (K_α) X-ray is generated from the silicon detector crystal and escapes the detector. The energy measured for the incoming X-ray is reduced by the magnitude of the Si (K_α) X-ray and an escape peak is detected in the spectrum. Less than 2% of incoming X-rays will fluoresce Si (K_α) X-rays, so escape peaks form minor peaks located at an energy less than the energy of related major peaks in the spectrum.

The electron beam - sample - detector geometry should be optimized. The X-ray EDX detector will have been installed with an optimal working distance, and this will vary from microscope to microscope. The X-ray detector should be as close as possible to the sample to maximize collection of the generated X-rays, but this may be limited by the presence of other detectors and safe operation of the microscope. There should be a clear path between the sample and the X-ray detector.
To determine the nature of the different lines in the acquired spectrum qualitative analysis can be afforded to identify the different elements present in the sample in respect to these characteristic X-ray peaks, but their abundances are not determined. Commercial peak-identification software were developed and therefore allow to correct the different possible artifacts present in the EDX spectrum (presence of overlapping peaks) and allow to attribute each of the peaks in the spectrum to the corresponding elements affirmed to be present in the sample, but the results need to be always verified.

4.3.1 X-ray Quantification Analysis

In the quantifications performed in Chapter 5 and 6, we quantified X-ray hypermaps acquired in STEM mode at 200 kV using state-of-the-art FEI microscopes Osiris or Themis equipped with a FEG source, C_s-corrector (Themis) and four Silicon Drift Detectors (SDD). These acquired hypermaps are characterized by a full spectrum at every pixel in the STEM image. We used this method, since, it is the best way to gather X-ray information with some semblance of statistical significance and without operator bias [64]. All these equipments provided by this new generation of microscopes allow to provide a maximum collection angle, therefore sufficient counts specially with the use of the 4 detectors and a high spatial resolution due to the help of the FEG source and the C_s corrector. In addition, they provide a reduced acquisition time which avoids sample drift, damage and contamination.
To quantify the acquired hypermaps, we proceed as following : first the Bremsstrahlung (background) X-ray counts have to be subtracted from the spectrum, then the characteristic X-ray peaks have to be processed to derive the concentration of the element concerned.
The background subtraction is performed using the QUANTAX-800 software from BRUKER. The quantification of the extracted X-ray peaks in commercial softwares is based on Cliff-Lorimer quantification and generally the resulting data are only an estimation of the element composition present in the analyzed sample. Cliff-Lorimer (CL) quantification allows to relate the characteristic X-ray intensities of each element present in the sample to the weight percents via the relation:

$$\frac{C_A}{C_B} = k_{AB}\,\frac{I_A}{I_B} \tag{4.4}$$

where C_A and C_B are the weight percents of each element and I_A, I_B are the characteristic X-ray intensities of each of the elements A and B, respectively. k_{AB} is called Cliff-Lorimer factor and is a sensitive factor depending on both the TEM instrument and the acceleration voltage used during the experiment. This factor is determined from a multielement standard composed from both A and B elements where both their respective weight percents is known. Yet, the k_{AB} factor can be determined both theoretically and experimentally but many studies showed [69, 70] that the most accurate quantifications were based on experimentally determined k-factors. The experimental approach to determine these k-factors is very tedious and is limited by a phenomenon that takes place even in thin-films, which is absorption.
X-ray absorption is one of the issues faced in the quantitative EDX analysis. It occurs

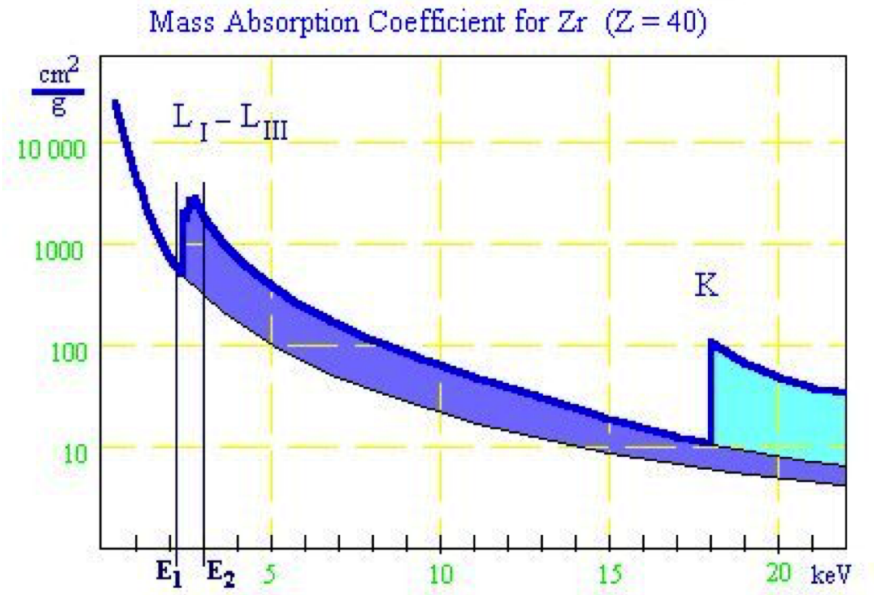

FIGURE 4.2: A schematic of an infinite flat sample with its respective thickness **t** representing the X-ray absorption phenomenon. [10]

in all heterogenous samples where for example a characteristic X-ray of an element A is absorbed by the surrounding matrix resulting in an under estimation of its concentration during the X-ray quantification. Goldstein et al [71] proposed a correction to the equation (4.4) by introducing a factor **A** which is the absorption correction factor derived from the originally Beer-Lambert-Bouger law. This latter predicts the absorption in a material where it relates the primary generated X-ray intensity to the resulting X-ray emerging from a thin-film as follow:

$$I_{emitted} = I_{generated} \times A^{-1} = I_{generated} \times e^{-(\frac{\mu}{\rho})\rho t} \tag{4.5}$$

where $(\frac{\mu}{\rho})$ is the mass absorption coefficient (MAC), ρ is the sample density and t is the thin-film thickness. Thus, if one want to neglect the absorption term, the working conditions need to satisfy: $(\frac{\mu}{\rho})\rho z << 1$. From these 3 different terms the tangible term is $(\frac{\mu}{\rho})$.

Fig.(4.2) represent the evolution of the MAC determined for **Zr** as a function of energy. Different jumps are seen in the (MAC vs E) plot and appear to be less intense at high energies. These observations are explained by an X-ray absorption occurring at different energy levels of the elements composing the analyzed sample. This explains why we should focus on the X-rays generated at high energies during the quantification, to reduce errors in the quantification due to absorption.

Furthermore, the factor **A** introduced in CL approach is an integration of the eq.(4.5)

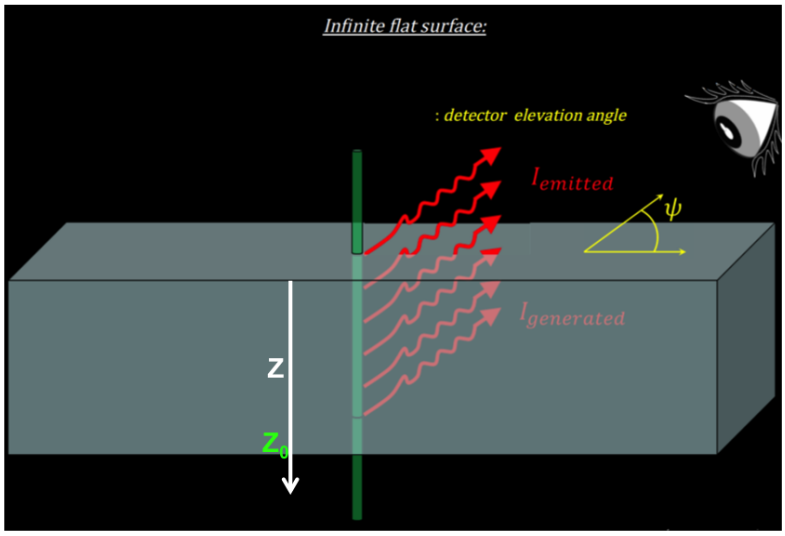

FIGURE 4.3: A schematic of an infinite flat sample with its respective thickness **t** representing the X-ray absorption phenomenon. [**?**]

(Beer's law) along the sample (represented in Fig.(4.3)) resulting in the following expression (for more calculation details see [72]) :

$$A = \frac{(\frac{\mu}{\rho})\rho t cosec\alpha}{1 - e^{(-\frac{\mu}{\rho}\rho t cosec\alpha)}} \tag{4.6}$$

where α is the take-off angle and $t\ cosseca\alpha$ is equal to the distance from the generation point to the surface [72].

This expression is used in both the CL and the eq.(4.4) is now corrected an written as :

$$\frac{C_A}{C_B} = k_{AB}\frac{I_A A_A}{I_B A_B} \tag{4.7}$$

These final equations (4.7 and 4.6) can allow to perform a correct quantification by performing an iterative solving process allowing to converge and determine the compositions ratio in eq.(4.7). The same approach is followed to determine the k-factor based on eq.(4.7) from a standard with known composition, density and thickness. However, this approach to determine the k-factor is one of the most important limitations of the CL approach. Since, it's not always evident to have an idea on the thickness and the density of the characterized sample. Therefore, to overcome this problem related to this limitation and other limitations well described in [64, 73]. Watanabe and William [73], described a new quantification thin-film procedure termed ζ-factor method where no need to have a prior knowledge of both sample (thickness

and density) as can be seen from the ζ-factor expression for an element A [73] :

$$\zeta = \frac{M_A}{N_v Q_A \omega_A a_A \frac{\Omega}{4\pi} \epsilon_A} \tag{4.8}$$

where where N_v is Avogadro's number, Q_A is the ionization cross-section, ω_A is the fluorescence yield, a_A is the relative transition probability (i.e. the relative line weight), M_A is the atomic weight, $\frac{\Omega}{4\pi}$ is the detector collection-angle in the whole 4π space and ϵ_A is the detector efficiency.

As can be seen from eq.(4.8), the new ζ-factor is dependent only on the X-ray energy and the accelerating voltage and is independent of the specimen composition, thickness and density. [73]

This ζ-factor is incorporated in a relation established in order to determine the density and thickness product by relating between ρt and I_A for an element A :

$$\rho t = \zeta_A \frac{I_A}{C_A D_e} \tag{4.9}$$

ρ and t are the specimen density and thickness, respectively. ζ_A is a proportional factor connecting I_A to ρt and C_A, and D_e is the total electron dose during acquisition defined as :

$$D_e = N_e I_p \tau \tag{4.10}$$

N_e is the number of electrons in a unit electric charge and I_p and τ are the beam current and acquisition time, respectively.

Similar to eq.(4.9), a relationship between ρt and I_B can be established using the ζ-factor for an element B :

$$\rho t = \zeta_B \frac{I_B}{C_B D_e} \tag{4.11}$$

From eq.(4.9) and eq.(4.11), assuming that $C_A + C_B = 1$ in a binary system, ρt can be expressed as :

$$\rho t = \frac{\zeta_A I_A + \zeta_B I_B}{D_e},\ C_A = \frac{\zeta_A I_A}{\zeta_A I_A + \zeta_B I_B},\ C_B = \frac{\zeta_B I_B}{\zeta_A I_A + \zeta_B I_B} \tag{4.12}$$

Therefore, C_A, C_B and ρt can be determined simultaneously from measured X-ray intensities but k-factors are no longer required. Eq.(4.12) is valid as long as $\sum C_i = 1$, which appears a reasonable assumption. The absorption term represented in eq.(4.6) is introduced in eq.(4.12) in the same way introduced in CL expression:

$$\rho t = \sum_j^N \frac{\zeta_j I_j A_j}{D_e},\ C_N = \frac{\zeta_N I_N A_N}{\sum_j^N \zeta_j I_j A_j} \tag{4.13}$$

In the quantified EDX data presented in this thesis, the absorption-correction term was estimated from a model that takes into account the direction of the X-ray emission (since the absorption term **A** represented in eq.(4.6) is characteristic of an infinite flat surface) relative to the position of the detectors. In addition, a geometrical model was used that allows to build a 3D reconstruction of the sample based on a model of its corresponding cross-section by limiting the number of projections to only two projections. The NW cross-section can be modeled by a series of imbricated ellipses, hexagons or rectangles, depending on the NW crystal structure and facets. More details about this 3D reconstruction are presented in Rueda et al [74].

Chapter 5

Experimental Setup

5.1 Introduction

The solid-state reactions introduced in chapter 2 were activated using conventional thermal heating experiments either ex-situ or in-situ in a TEM. Performing in-situ TEM heating experiments have as a goal to control the silicide or germanide segment and follow all the phenomena that occur during the exchange process with nm or atomic spatial resolution. These in-situ heating experiments were achieved by the intermediate of a heating stage. The in-situ heating stages for TEM are normally integrated as part of the specimen holder cradle and use precise Joule heating and temperature dissipation to obtain tunable and stable sample temperatures. Fig.(5.1.a) depicts a Gatan single tilt heating stage that can accommodate a 3 mm disk specimen and can reach 1200°C [11]. When it is the aim to perform high resolution TEM imaging at elevated temperatures, it is imperative to obtain high (<0.1°C/min) temperature stability and low sample drift. This is difficult to achieve with a large sample stage that has a very large thermal mass and, respectively, slow temperature response. To address this issue, a new generation heating stages were developed and are commercially available by DENSsolutions [12] and Protochips Inc [13]. These use integrated circuitry to produce localised resistive heating directly on the sample support. Such stages show much lower thermal mass and very high thermal stability that allow high resolution imaging at elevated temperatures. Additionally, this type of stages offers disposable design of the heating elements, for example, the integrated circuit platform (chip). Since the heated area is very small, contamination problems are reduced. However, the chip design did not allow simultaneous heating

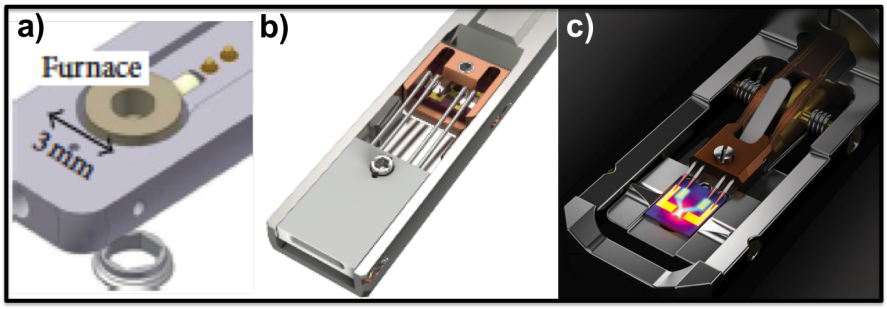

FIGURE 5.1: a) Schematic of a heating sample holder that accommodates full-size TEM grids commercially available from Gatan [11]. b) Schematic of a four pins double tilt heating sample holder commercially available from DENSsolution [12]. c) Photograph of double tilt heating sample holder commercially available from Protochips Inc [13].

and electrical measurements of the created NW heterostructure at the time. Therefore, to potentially provide a better control of the germanide segment length and to perform a local heating in a specific region of the target device, a new method was proposed by Massimo et al [20, 75] that we called the direct Joule heating technique. In addition, this method combines heating and electrical measurements of the NW heterostructure.

Direct Joule heating [H_a] provides different advantages, as an example: it allows to combine both heating and electrical experiments. Furthermore, it could provide a better control of the germanide or silicide segment by following in real-time the electrical properties, that are potentially more precise, as propagation depends on NW diameter and metal NW interface quality, where controlling only temperature is not precise enough. However, one of the inconveniences of H_a heating experiments is that they are not calibrated in temperature, which is not adequate for a kinetic study. The geometry of the contacts is displayed in Fig.(5.2.b). This technique offers unique advantages as compared to conventional thermal treatments :

- It allows the reproducible fabrication of ultrascaled FETs with channel lengths down to few nms [75].
- There is no need for searching optimum conditions regarding the time and the annealing temperature.
- It can be easily extended to other contact metals that form germanides and, possibly, to any type of contact and nanowire or a generic nanostructure which requires an annealing step.

5.2 In-situ TEM Heating Setup

The in-situ experiments were carried out in a Philips CM300 at 100 kV and an FEI Titan at 80 kV. An acceleration voltage below 150 kV was used to avoid knock-on damage, creation of vacancies and related modifications of electrical and diffusion properties. A 6 contact biasing sample holder from DENSsolutions (see Fig.(5.2.c)) was used for in-situ annealing experiments.

5.2.1 Uncalibrated Temperature Direct Joule Heating [H$_a$]

In the in-situ direct Joule heating experiments [H$_a$], the heating system comprises five main components (see.Fig(5.3)):

(i) Heating sample : Electrically contacted NW on membrane (Fig.5.2)

(ii) A low-drift TEM holder with electrical connections

(iii) An electrical interconnect box

(iv) Electrical setup

(v) A computer and labwindows program to control the heating current

Using an e-beam lithography step the NW is contacted by two metal strip-lines, that are connected to large Ti/Au pads defined in a prior laser lithography step, see Fig.(5.2a,c). The contacted NW is locally heated by flowing a current through one of the strip-lines creating a Joule heating current $I_{heating}$, see Fig.(5.2.b). In these experiments an (a)symmetrical positive V^+ and negative V^- voltage were applied on both ends of a Cu strip line to decouple the heating current from the current through the NW, I_{NW}, that is measured with a picoampermeter providing a real time measurement of the current during the germanide process, see Fig.(5.2.b) and Fig.(5.3). The heating current and the applied potential are decoupled in the sense that we can vary the bias potential on the NW while keeping the heating current constant. To provide the heating current $I_{heating}$ we use two current generators (Keithley), these two generators are controlled by a labwindows program. Additionally, this software allows a real-time observation of the metal resistance (R_{strip}), the current through the contact (I$_{strip}$) and the current through the nanowire (I$_{NW}$) evolution during the in-situ

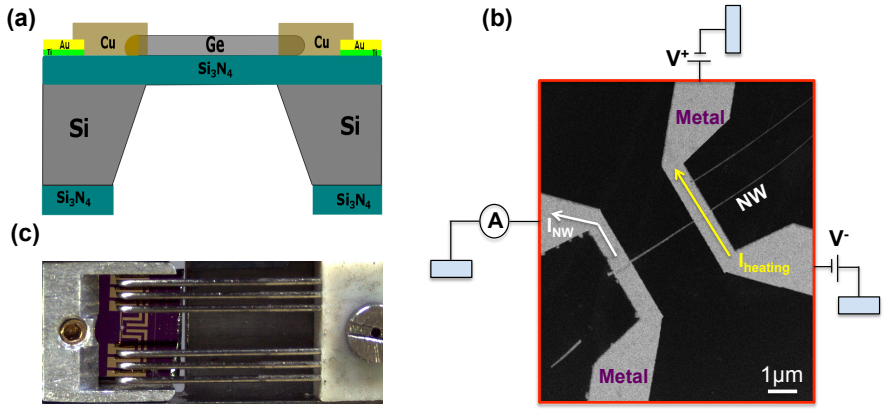

FIGURE 5.2: Illustration of the direct Joule heating technique [H_a] allowing the germanide formation. (a) Schematic of a cross-sectional view representing a contacted Ge NW on a silicon nitride membrane. The Ge NW is contacted by Copper metal pads which are connected to the sample holder via Ti/Au pads contacted by small needles. (b) High angle annular dark field (HAADF) STEM image showing a top view of a connected Ge NW by two Cu metal strip lines. Cu contacts are heated one at a time via a heating current $I_{heating}$ driven by the voltage difference $(V^+ - V^-)$ while measuring the current I_{NW} through the GeNW. (c) Photograph of microfabricated membrane loaded on a 6 contact biasing sample holder from DENS solution.

heating experiment. In fact, following the metal resistance R_{strip} in real-time provides a qualitative feedback on the annealing or damage to the metal strip which is reflected in an increase of the metal resistance due to electromigration. When we observe an increase in R_{strip}, we inverse the applied voltage on the end contacts to limit electromigration in one direction which can allow to remedy the metal stripline. A cable connection is used to connect the sample holder to the Keithleys and the picoampermeter through an interconnect box, see Fig.(5.3), which assures the electrical connection between the sample holder and the outside environment (electrical setup).

5.2.2 Calibrated Temperature Joule Heating [H_b]

In the in-situ calibrated Joule heating experiments [H_b], the heating system comprises four main components (see.Fig(5.5)) [76]:

(i) Denssolution heating chip

(ii) A low-drift TEM holder with electrical connections

(iii) An electrical control box

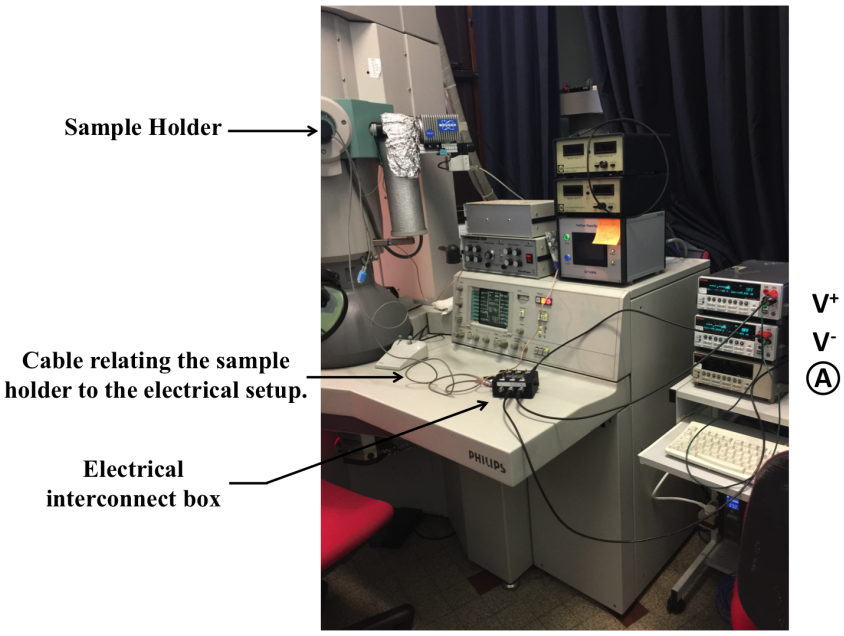

FIGURE 5.3: Photograph of the system (the two current generators and the picoampermeter) connected to the TEM sample holder through an interconnect box. A labwindows program allows to monitor both heating and biasing process.

(iv) A computer to control the heating system

A software interface is connected with the electrical control box (outside the TEM) to enable communication between the heater chip and the computer. Each heating chip is used as a sample carrier that replaces a traditional TEM grid and has dimensions of 3.9 × 3.2 mm. It contains a micrometer-sized Mo or Pt spiral, which is sandwiched inside a few 100 nm thick SiN_x membrane that is used as a micro-hotplate and requires only few milliwatt to heat a sample from room temperature to 1300°C. These chips offer a highly stable platform for atomic-resolution in-situ heating/biasing experiments. Between the Mo spirals, there are multiple micrometer-sized electron-transparent windows with a thickness of 20 nm, where the NWs were dispersed and lithographically contacted as already shown and described in chapter 3). In both experiments the electrical setup was grounded using the ground of the TEM.

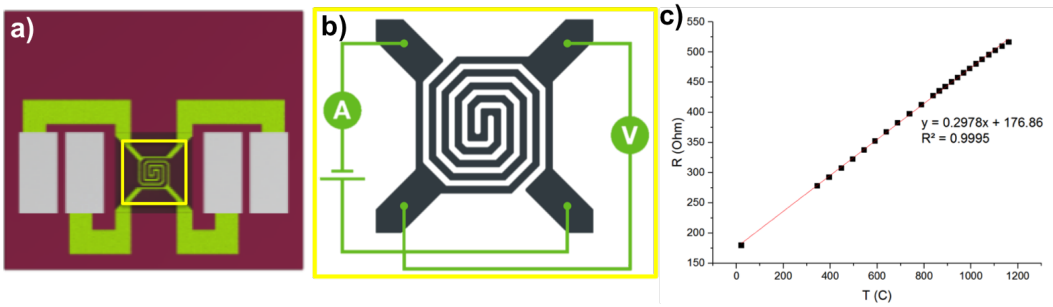

FIGURE 5.4: a) Photograph of microfabricated commercial membrane from DENSsolution calibrated in temperature used during H_b heating experiments. b) The 4 point-probe configuration where 2 contacts deliver the current (A) and 2 contacts measure the resistance (V). c) Represent the linear relation of the Mo spiral resistance over the temperature range which proves the resistance thermometer accuracy with respect to the temperature range where it's used.

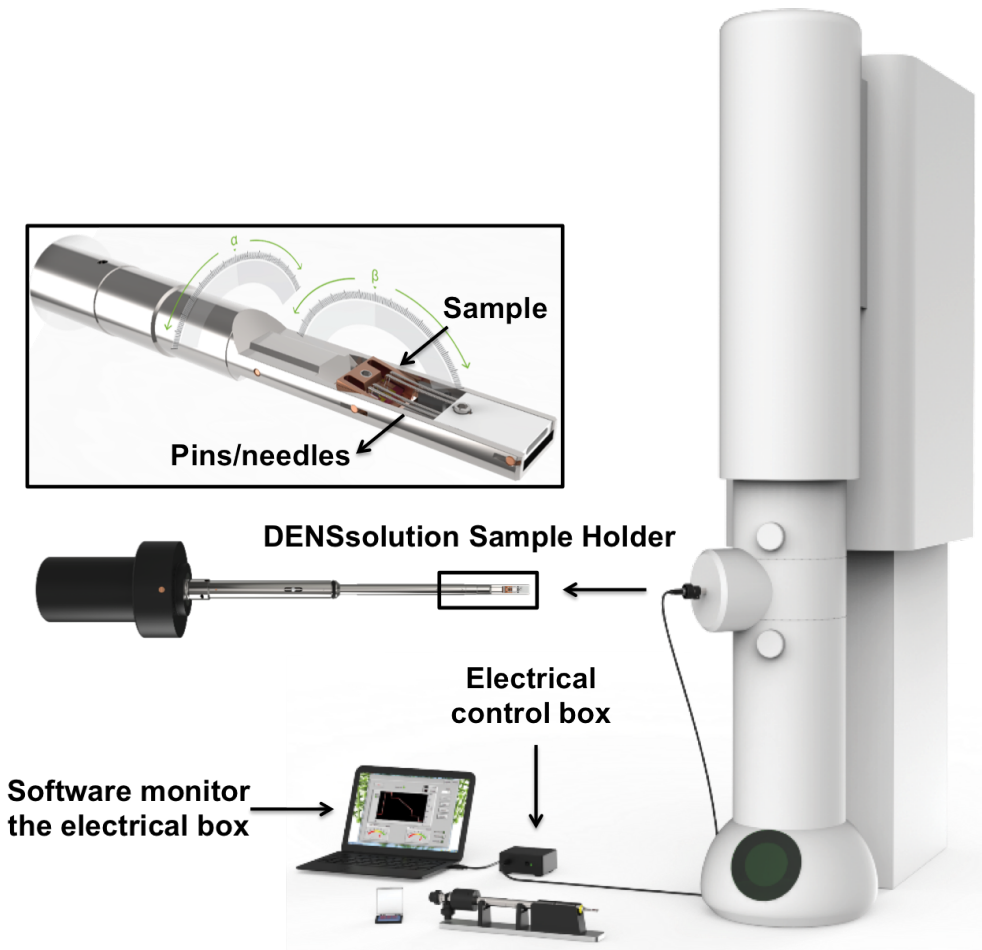

FIGURE 5.5: Design drawing of the main components of the DENSsolutions double-tilt heating system.

Chapter 6

TEM Study of Cu-Ge (NW) Solid-State Reaction

In this chapter, the work performed on the solid-state reaction between Cu and Ge nanowires is reported. In a first part the solid-state reaction is initiated and followed in-situ in a TEM microscope (see also section 5.1). As already said in chapter 5, the reaction was triggered by using two approaches, either with a *direct* Joule heating technique, referred to as H_a, or using a Joule heating method where a buried heating spiral heats the sample on the membrane, named H_b. The in-situ observation allows us to locate the interface position between the Cu-germanide and the Ge as a function of time (section 6.2). We observe that the reaction is not triggered simultaneously in all the contacted NWs and performed different NW sample preparations in order to determine the influence of the initial Cu-Ge interface ((subsection 6.2.3). The structure and chemistry of the Cu-germanide phase were then studied ex-situ by electron diffraction (section 6.3) and EDX (section 6.4). The last part of this chapter (section 6.6), presents the modeling and the discussion of the experimental work.

6.1 In-situ Phase Propagation of Cu-Ge Nanowire System

The samples were prepared as shown in chapter 3 and mounted for the in-situ experiments as described in chapter 5. The microscope was set up in TEM mode. First, the different NWs were localized and their positions stored in the microscope interface.

Then a selected NW was visualized in live mode on a TEM camera. The magnification of the TEM was set up at a rather low magnification, in order to see the Cu contact and the two sides of the NWs (see Fig. (6.1). The temperature of the NW was then progressively raised, by increasing the current either in one of the the Cu-contacts (case of direct Joule Heating, H_a) or in a buried heating spiral in a heater chip from DENSsolution (H_b). As the DENSsolution heater chips are calibrated, the current passed through the buried spiral gives directly the temperature of the membrane-substrate on which the NW with its metal reservoir is deposited. This is not the case for the direct Joule heating experiment. So direct Joule heating experiments will be characterized not by the temperature but by the voltage that is applied. When the reaction starts, the contrast in the Ge NW changes and immediately the increase of the temperature was stopped, i.e. the temperature was kept constant. Regularly, generally every ~ 0.5 sec, an image of the NW is acquired. This series of images, which forms a movie, allows us to follow the location of the reaction front. When the reaction front has been propagated over a relatively large distance, the temperature was brought back to room temperature and the different NWs on the membrane were visualized. As we will see below, it happens that the reaction did not start in all the contacted NWs. It is the reason why the previous steps (live imaging of a given nanowire, increase of temperature, stabilization of temperature and acquisition of a series of images) have been repeated several times, allowing us to study how the reaction varies with temperatures.

6.2 Kinetic of Cu-Ge Phase Formation

All the performed experiments were performed in-situ in a CM300 and an FEI Titan TEM to provide a better control of the germanide segment length and follow all the phenomena that occur during the copper-germanium phase formation with nm spatial resolution. We follow the location of the reaction front in real time to get insight into the dynamics of the diffusion process and compare with diffusion models. Moreover, we study the formed heterostructures ex-situ using chemical mapping by EDX and diffraction studies to validate the diffusion model. In the following, we present 4 heated samples where in 2 samples we used H_a and in the 2 others H_b heating techniques.

6.2.1 Direct Joule Heating

Fig.(6.1) summarizes the result of two direct Joule heating experiments. Fig. (6.1.a, left) is an image of a NW and its Cu pad before heating. The Cu pad has been deposited approximately in the middle of the NW and so we could observe the propagation of the Cu into the two sides of the NW. In this case, the diameter of the NW is not constant. Its shape is slightly conical. On the part of the NW above the Cu pad, called L_{side1}, the diameter varies from 22 to 32 nm. On the part of the NW below the Cu pad, called L_{side2}, the total diameter of the NW has a rather constant diameter of about 32 nm. On the NW segment L_{side1} an amorphous shell is present. This unintentional shell around the Ge NW was a particularity of this NW. We attributed this shell to remaining resist on the Ge NW after sample preparation. This unintentional shell was interesting for studying the influence of the Ge NW surface on the solid-state reaction. The solid-state reaction started at an applied voltage of 0.75 V resulting in a metal intrusion where a phase is observed to propagate during 400 sec. Fig.(6.1.a, right) is an image of the NW at the end of the heating during t = 400 sec. One can notice that the two sides of the NW are very different. The surface of the NW in L_{side1} is still smooth, while a lot of protruding crystals were formed in L_{side2}. In these TEM images, the Cu-germanide parts of the nanowire are slightly darker than the Ge parts and the position of the germanide/Ge interface can be easily located. Fig. (6.1.b) shows the plots where we followed the progress of the germanide interface as a function of time, L is the distance of the reaction interface between the Cu pad and the germanide/Ge interface. Despite the slight change in the diameters of both NW sides and the presence of protruding crystals in L_{side2}, while no crystals appeared in L_{side1}, the germanide transformed segment in L_{side1} (L_{side1} = 0.51 μm) and L_{side2} (L_{side1} = 0.49 μm) are almost equal. This slight length difference can be attributed to the small difference in NW diameter. Fig. (6.1.c) shows a direct Joule heating on another sample. Here we can notice again the presence of the protruding crystals along the transformed region (L = 1.35 μm) of the NW. The length-curves cannot be fitted by a simple square root function for propagation over longer parts of the NW. There are in fact two regions in this curve that are more clearly visible in the inset of (6.1.d), where the x-axis is plotted as the square root of time. During the first 800 nm of propagation, the length-curve can be fitted by a square root function (a linear relation is visible when plotting as a function of $\sqrt{t}$, see inset Fig. (6.1.d). For longer propagation distances, we can no longer fit a simple square root function to the entire curve: this is reflected as a change in slope in the inset of Fig. (6.1.d).

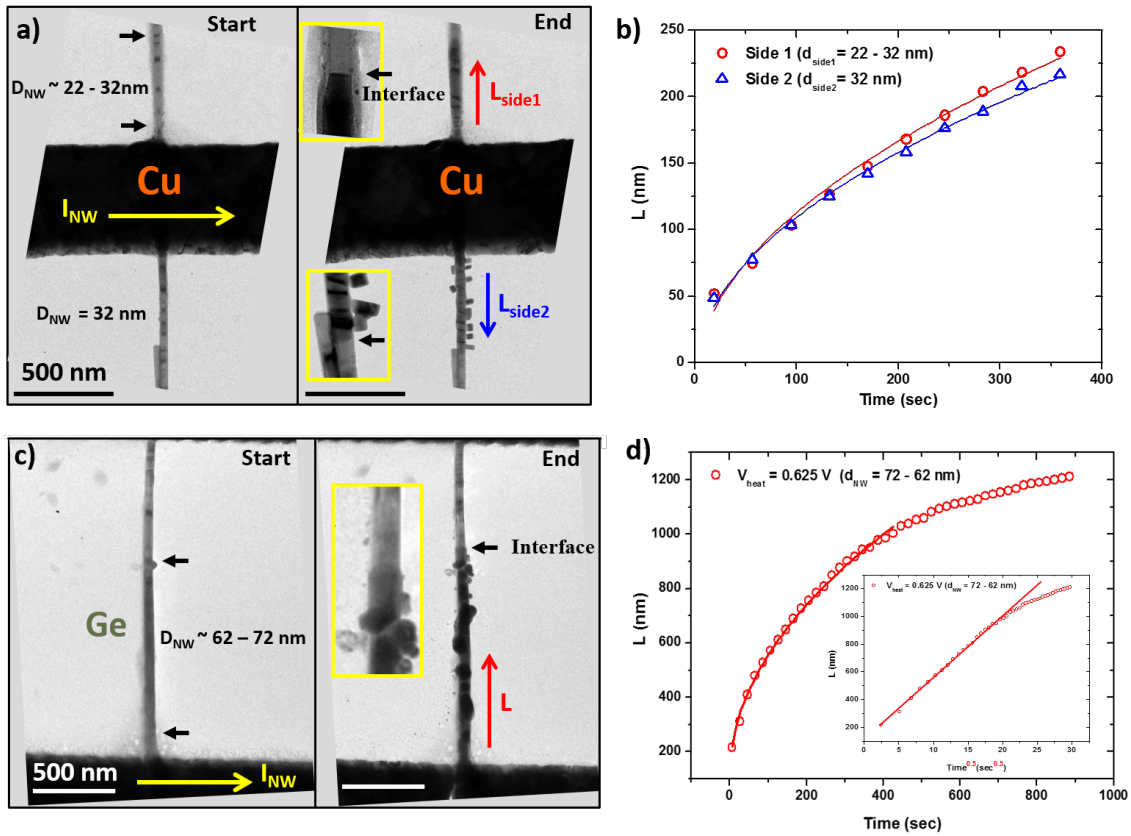

FIGURE 6.1: In-situ copper-germanium phase propagation experiments using both in situ direct Joule heating H_a. a, c) TEM image showing the sample heated using in-situ H_a. b) The length of germanide segment versus time at $\Delta V = 0,75V$ using in-situ H_a for both opposite propagation directions L_{side1} (∘ ; fit (—)) and L_{side2}(△; fit (—)). d) The length of germanide segment versus time at $\Delta V = 0,625V$ using in-situ H_a, L (∘ ; fit (—)).

We attributed these length-curve shapes to a variation of temperature along the NW. In order to prove that, we performed Comsol simulations (section 6.5) to estimate the temperature gradient along the NW segment. It was found (section 6.5) that the temperature is indeed not constant along the NW and so it appears that direct Joule heating is not an easy set-up to perform a kinetic study under a constant temperature. It is why we set up the membrane-substrate Joule heating experiment in order to have a well known constant temperature during the heating experiments. More discussion on H_a will be given in section 6.6.

6.2.2 Membrane-substrate Joule heating

Similarly to Fig.(6.1), Fig.(6.2) summarizes two membrane-substrate Joule heating H_b experiments on contacted NWs by Cu pads, obtained respectively at 360°C, 410°C and 600°C. In all cases, protruding crystals were observed. For annealing below 500°C, a square root function could be fitted to the length-curves. During the H_b heating experiments at 410°C, the reaction had not started in every contacted NW on the sample. Therefore, a second heating was applied with the aim to activate the solid-state reaction in the other contacted NWs present on the sample. The reaction started to occur at 600°C, however, again not all contacted NWs were activated. At 600°C, the propagation of the germanide is very fast and the position of the interface is not clearly seen in each frame. This explains why the points in the length-curve are more dispersed, especially for the L_{side1} in the NW of Fig.(6.2.e). However, the evolution of L_{side2} was tracked with more accuracy compared to L_{side1} and this can be clearly seen from the fitting where L_{side2} is well fitted by a linear function. It is found that at 600°C, the length-curve is better fitted by a linear function. As the NWs have slightly conical shapes, the variation of the germanide growth rate with the Ge NW diameter can be analysed by using the two sides of a NW. In all cases (i.e H_a or H_b heating experiments), the smaller diameters always showed a faster propagation of the reaction front.

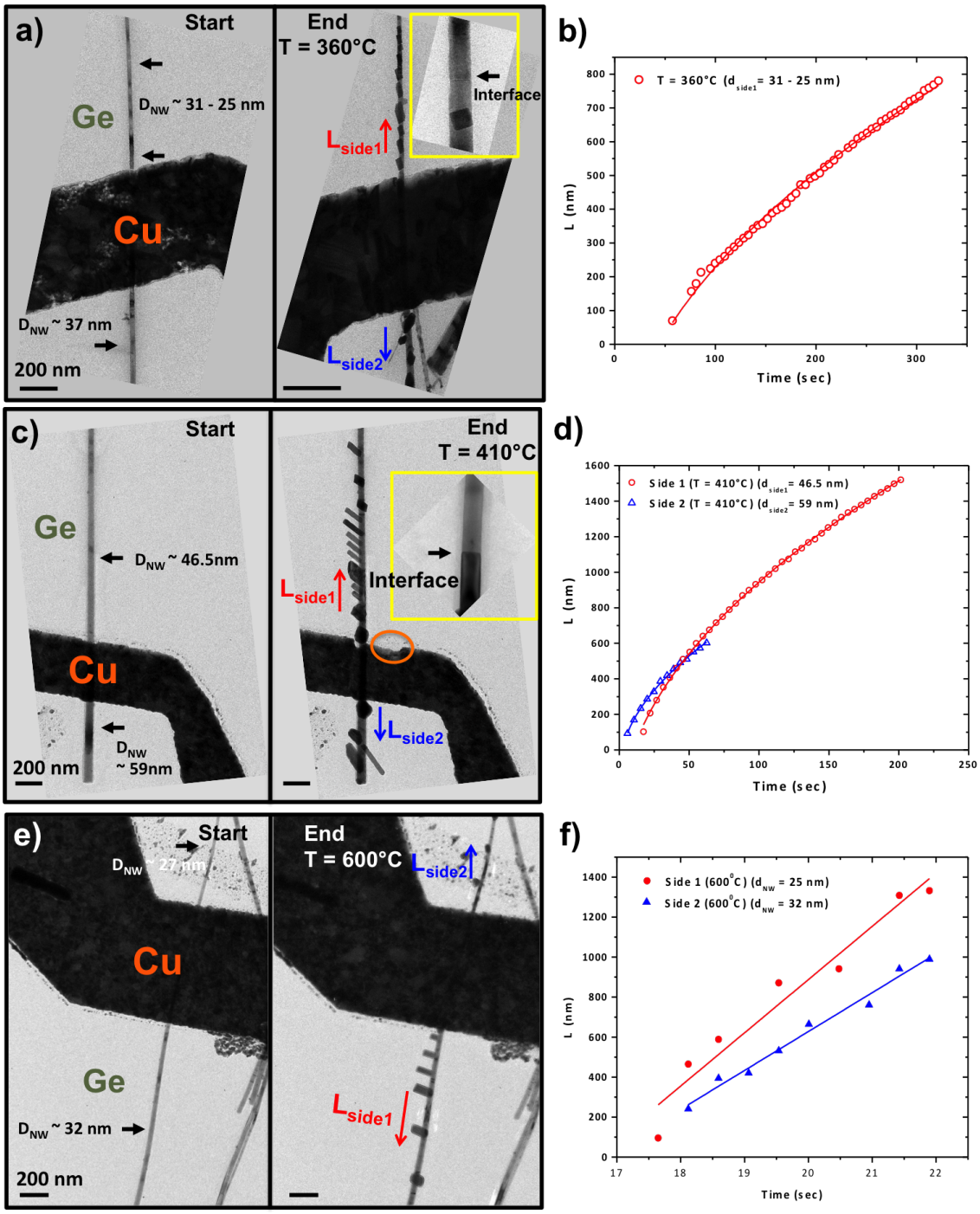

FIGURE 6.2: In-situ copper-germanium phase propagation experiments using membrane-substrate Joule heating H_b. a) TEM image showing the sample heated at 360 °C using in-situ H_b. b) The length of germanide segment versus time at 360°C for L_{side1} (∘ ; fit (—)) c, e) TEM images of in-situ heating experiments H_b at 410°C and 600°C, respectively. d) The length of germanide segment versus time at 410°C for both opposite propagation directions L_{side1}∘ ; fit (—)) and L_{side2}(△; fit (—)) f) The length of germanide segment versus time at 600°C for both opposite propagation directions L_{side1} (• ; fit (—)) and L_{side2}(▲; fit (—)). The sample reveals an influence of the NW diameter on the reaction speed.

6.2.3 Influence of the Cu-Ge interface on reaction initiation

After heating at 410°C to obtain the images in Fig.(6.1.c), we observed that the reaction had not started in every contacted NW on the sample. To investigate possible reasons for a delayed activation of the solid-state reaction in the contacted NWs, we prepared another sample for an [H_b] experiment. Additionally to the chemical cleaning of the NW prior to the metal deposition using HI:H_2O, an Ar plasma for 30 sec was applied to remove any native oxide left on the NW before metal deposition. Although the solid-state reaction started in some NWs at a lower temperature (360°C) compared to the previous sample, again the reaction didn't start in all contacted NWs, even though the Cu/Ge NW reaction was activated in much more NWs compared to the previous sample. This reveals that the additional Ar plasma provides a better Cu/Ge NW contact. However, the contact is still not clean enough to start the reaction in all contacted NWs. Moreover, an incubation time was observed in the sample heated using H_b at 410°C (see Cu-M_2-H_b-410C) and noticed at 360°C, where the reaction started later in some NWs at constant heating. At 410°C the propagation starts in 4 NWs out of 42 contacted NWs, see Table.(6.1). Movie Cu-M_2-H_b-410C presents a clear illustration of the metal/Ge NW interface influence, where the propagation starts later in the second NW than the first. In addition, the reaction didn't initiate in the third NW during the entire heating process. In the sample treated with the additional Ar plasma, heated at 360°, the number of activated NWs increased and the propagation starts in 26 NWs out of 32 contacted NWs. The influence of the interface quality on the reaction initiation still manifested even at 600°C, where the number of transformed NWs raised to 17 NWs out of 42 contacted NWs (for the sample without Ar plasma), see Table.(6.2). Very interestingly, sometimes a NW was not connected

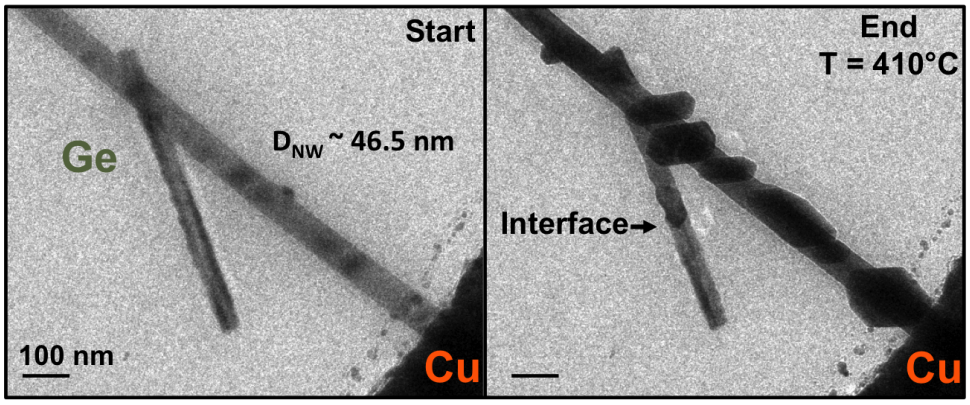

FIGURE 6.3: TEM images before and after heating at 410°C showing the propagation taking place in a Ge NW without been contacted to the Cu pad.

to a Cu pad, but was just touching a NW connected to a Cu pad. In this case, when the propagation front of the connected NW reached the adjacent NW, the germanide did propagate in the adjacent NW, both at high or low temperature (see Fig.(6.3)). However when propagation started in the adjacent NW, the propagation speed in the connected NW was reduced.

Furthermore, some of the heated samples at 600°C showed a detachment from the metal contact either after nucleation or without any start of the solid-state reaction see Fig.(6.4). These observations are reported only at high temperature. In addition, the metal contacts quality degraded after the heating at 600°C.

TABLE 6.1: A summary of all contacted NWs showing the number of activated NWs during the solid-state reaction using the thermal heating [H_b] at 410°C. Only 4 NWs out of 42 contacted NWs were activated and gave rise to the germanide phase formation at 410°C. Hole (xx) indicates the window on the DENS chip where the NWs were located.

	Number of nanowires	Propagation
Hole 1	1	no
Hole 2	1	no
Hole 4	1	no
Hole 5	6	no
Hole 6	1	yes
Hole 7	2	1 NW (yes) and 1 NW (no)
Hole 10	2	no
Hole 11	3	2 NW (yes) and 1 NW (no)
Hole 12	5	no
Hole 13	2	no
Hole 14	4	no
Hole 15	1	no
Hole 17	2	no
Hole 18	7	no
Hole 20	2	no
Hole 21	5	no
Hole 25	3	no
Hole 27	2	no

TABLE 6.2: A summary of all contacted NWs showing the number of activated NWs during the solid-state reaction using the thermal heating [H_b] at 600°C. 17 NWs out of 42 contacted NWs were activated after the second heating at 600°C and were completely transformed into a Cu_5Ge phase structure. Hole (xx) indicates the window on the DENS chip where the NWs were located

	Number of nanowires	Propagation
Hole 1	1	no
Hole 2	1	yes
Hole 4	1	no
Hole 5	6	2 NWs (yes) and 4 NWs (no)
Hole 6	1	yes
Hole 7	2	yes
Hole 10	2	no
Hole 11	3	yes
Hole 12	5	2 NWs (yes) and 3 NWs (no)
Hole 13	2	yes
Hole 14	4	no
Hole 15	1	no
Hole 17	2	no
Hole 18	7	2 NWs (yes) and 5 NWs (no)
Hole 20	2	no
Hole 21	5	2 NWs (yes) and 3 NWs (no)
Hole 25	3	no
Hole 27	2	no

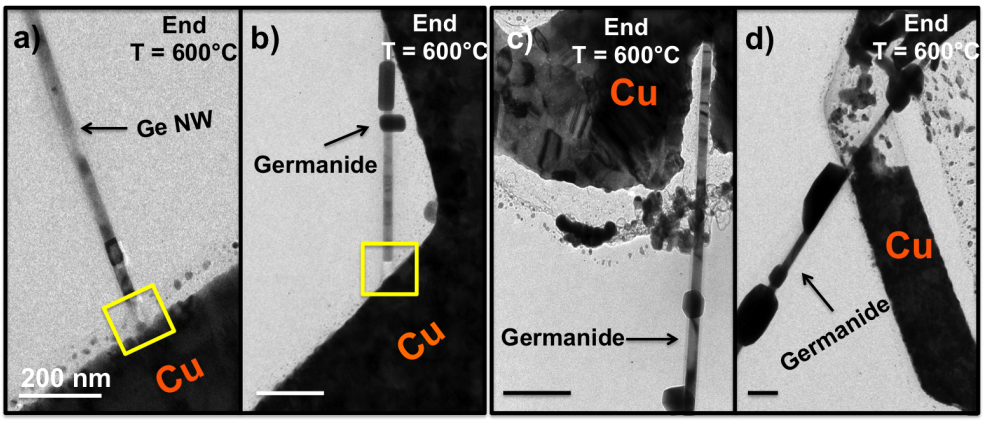

FIGURE 6.4: TEM images after thermal annealing [H_b] at 600°C. a), b) TEM images taken after the in-situ [H_b] heating at 600°C where the NWs appear to be detached from the metal with or without formation of the germanide phase in the Ge NW. c), d) TEM image of the Cu contact after the heating experiment showing a degradation of the metal contact.

6.3 Structural Analysis of the Germanide Phase

The germanide phases were structurally studied in order to determine which phase is formed at low or high temperature. Nanobeam diffraction was performed in an

FEI Titan at 80 kV (the NW was scanned by a small probe ~ 10 nm) while electron diffraction tomography was done on a Philips CM300 at 300 kV.

6.3.1 Nanobeam Electron Diffraction

Fig.(6.5.a) presents HAADF STEM images after H_a heating experiments. The contrast in HAADF STEM depends both on the sample thickness and on its composition, where the more heavy elements scatter more electrons on the annular detector, giving rise to a brighter contrast. Therefore, a strong contrast is present on the thicker Cu contacts and on the transformed region due to the change in the NW diameter after copper intrusion compared to the unreacted Ge part.
Electron diffraction studies showed that at low temperature (360 and 410°C) in H_b and in H_a experiments, the germanide phase formed was a Cu_3Ge phase with an orthorhombic structure [30, 34] with lattice parameters (a = 4.576 Å, b = 5.272 Å and c = 4.2 Å) and space group Pmmn (see Fig.(6.5.c)). The diffraction patterns taken at two different orientations are shown, Fig.(6.5.c):

- The Ge part (green squares) oriented along the [011] zone axis and the Cu_3Ge along the [53-6] zone axis, respectively, Fig.(6.5.c, top).
- The Ge part (green squares) oriented along the [-112] zone axis and the Cu_3Ge along the [10-3] zone axis, respectively.

The protruding crystals show often similar diffraction patterns as the core of the NW

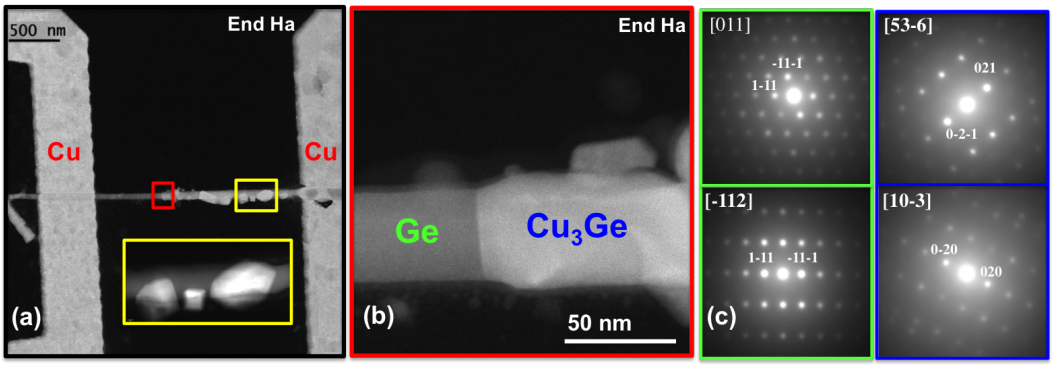

FIGURE 6.5: (S)TEM images of a Cu-Ge (NW) solid-state reaction after H_a heating process. (a),(b) HAADF STEM images of copper-germanium phase propagation after H_a heating process showing the exchanged segment length and Cu_3Ge/Ge interface, respectively. The inset image in *a* shows the shape of the protruding crystals. (c) Nano Electron beam diffraction patterns on both the Ge and Cu_3Ge part at two different orientations.

and appear therefore to be also Cu_3Ge in the orthorhombic structure (as will be confirmed later by EDX). However their orientation can be different from the NW core.

They show grain boundaries due to collapse of different protruded crystals shown later in Fig.(6.16). An abrupt interface separates Ge and the Cu_3Ge phase in the NW (see Fig.(6.5.b)).
As already discussed in (chapter 2), the different phases ϵ-Cu_3Ge and ϵ_2-Cu_3Ge reported to form in the solid-state reaction in the Cu-Ge system do not form in Ge NWs. In addition, the ϵ_1-Cu_3Ge monoclinic didn't form in these different experiments either using H_a or H_b heating techniques.
During the NBED experiments an electron probe is scanned across the specimen in STEM mode and a diffraction pattern is acquired at each point of the selected region on the specimen. A set of diffraction patterns was acquired on 2 different orientations by tilting the NW. The diffraction patterns changed along the transformed segment due to several effects:

- A rotation of the crystal was observed and can be attributed to the fact that the NW is bent.
- The diffraction pattern of the germanide core sometimes interfered with the protruding crystals, which makes the interpretation of the different diffraction patterns more difficult.

6.3.2 Electron Diffraction Tomography

In order to determine the atomic structure of the protruding crystals that appeared at 600°C in an H_b experiment, selected area electron diffraction tomography was performed on the longest protruded crystal (see selected region in Fig.(6.6.a). The [1-2 0] zone axis electron diffraction pattern presented in Fig.(6.6.b) confirms the good crystallinity of this region of the NW. The precession angle of the electron beam was 1.25°, in order to limit dynamical effects. 41 precession electron diffraction (PED) patterns were recorded, from sample holder tilt angle α = - 20° to + 20°, with a step of 1°. The intensities of the different reflections were extracted and analyzed using PETS and JANA softwares [77]. Slices of the reciprocal space are presented in Fig.(6.7). A hexagonal unit cell was determined, with parameters a = b = 2.6 Å, c = 4.2 Å. Reflection conditions were compatible with space group $P6_3/mmc$ (hkl: l = 2n). A structural model was determined from 14 independent reflexions using "ab initio" direct method calculations. The completeness was 88% for a resolution of 0.8 Å. It led to the disordered hexagonal compact Cu_5Ge structure already mentioned in the literature [3].

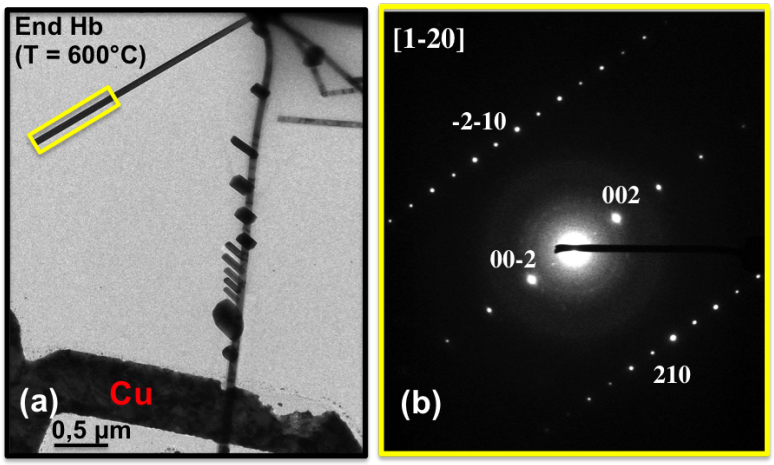

FIGURE 6.6: (a) TEM image of a Cu-Ge (NW) solid-state reaction after [H_b] heating at 600°C showing the exchanged segment of the Cu_5Ge. (b) A diffraction pattern that is indexed as an hexagonal Cu_5Ge phase.

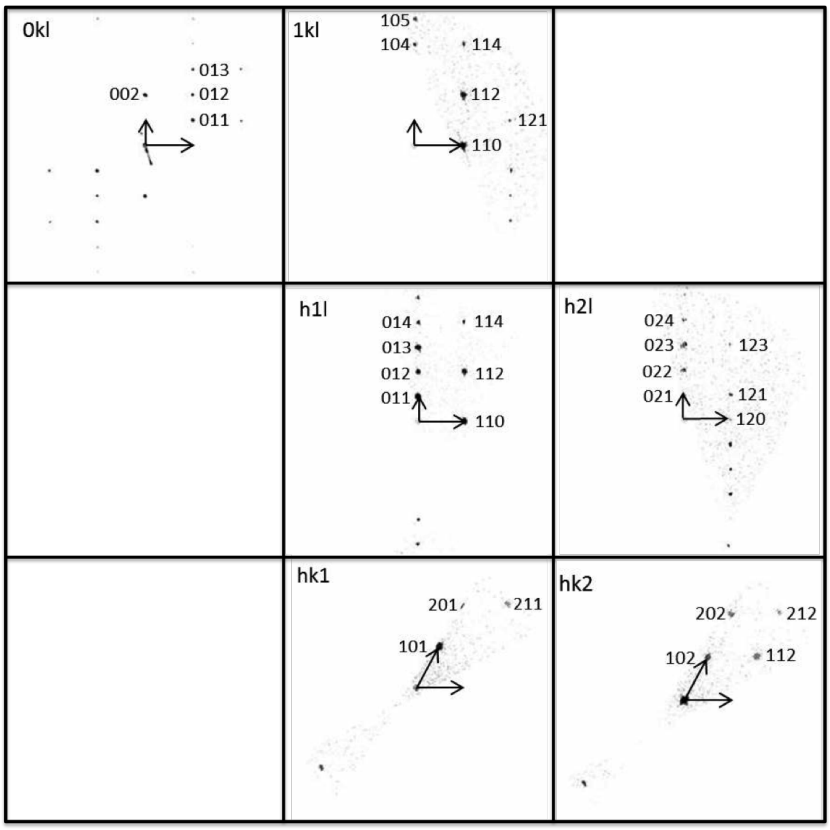

FIGURE 6.7: EDT slices of the reciprocal space at (hkl : l = 2n) compatible with the $P6_3/mmc$ space group.

6.4 Chemical Analysis of The Germanide Phase

To confirm the chemical composition of the germanide phase formed after H_a and H_b heating experiments, an energy dispersive X-ray (EDX) analysis at 200kV was performed in different samples. Chemical characterization was carried out ex-situ in a state of the art FEI Osiris or Titan Themis, equipped with four Silicon Drift Detectors using an utra-Narrow gap Fischione tomography sample holder, which allows a large solid angle for signal detection.

6.4.1 EDX Quantification and Modeling

Fig.(6.8.a) represents an HAADF STEM image of the sample shown in Fig.(6.1.a) heated using H_a. The brighter part corresponds to Cu_3Ge and the darker part to Ge. The inset represents an EDX hypermap. To provide a better quantitative analysis of the hypermap, we use a NW model as presented by Rueda et al [74]. Using the sample thickness extracted from the total X-ray count, a model of an hexagonal cross-section NW, including different layers, is calculated and compared with the experimental data to obtain a best fit. A reconstruction of the germanide cross-section extracted from the hypermap is represented in Fig.(6.8.b). This cross-section reproduces the experimentally quantified concentration profiles well. We find a cross-section of four imbricated hexagons : a thick Cu_3Ge core t = 53.35 nm surrounded by a shell of pure Cu with a thickness estimated ~ 0.8 nm, surrounded by a shell of pure Ge with a thickness estimated ~ 0.35 nm and covered by a GeO_2 shell ~ 4.5 nm. Fig.(6.8.c) illustrates the distribution of these different layers forming the NW cross-section.
The curves in Fig.(6.8.b) with symbols (--○--, --◇--, --□--) are the atom concentrations deduced directly from the net experimental X-ray intensities of each element using the zeta factor method [73] and the (—, —, —) curves are the calculated concentration profiles using the hexagonal model of the NW cross-section. To achieve a complete cross-section model, at least two X-ray maps acquired at two tilt angles are required [74], however the observation of a core-shell structure remains valid even though only one orientation was used to reconstruct the NW cross-section. The thickness of the pure Cu layer was estimated to be 0.8 nm (see Fig.(6.8.b,c)) and 1.2 nm in another studied sample shown in Fig.(6.10) using the same TEM. Given the precision of this method, we estimate the Cu layer thickness 1 ± 0.2 nm. These cross-section reconstructions were restricted to two samples which does not allow

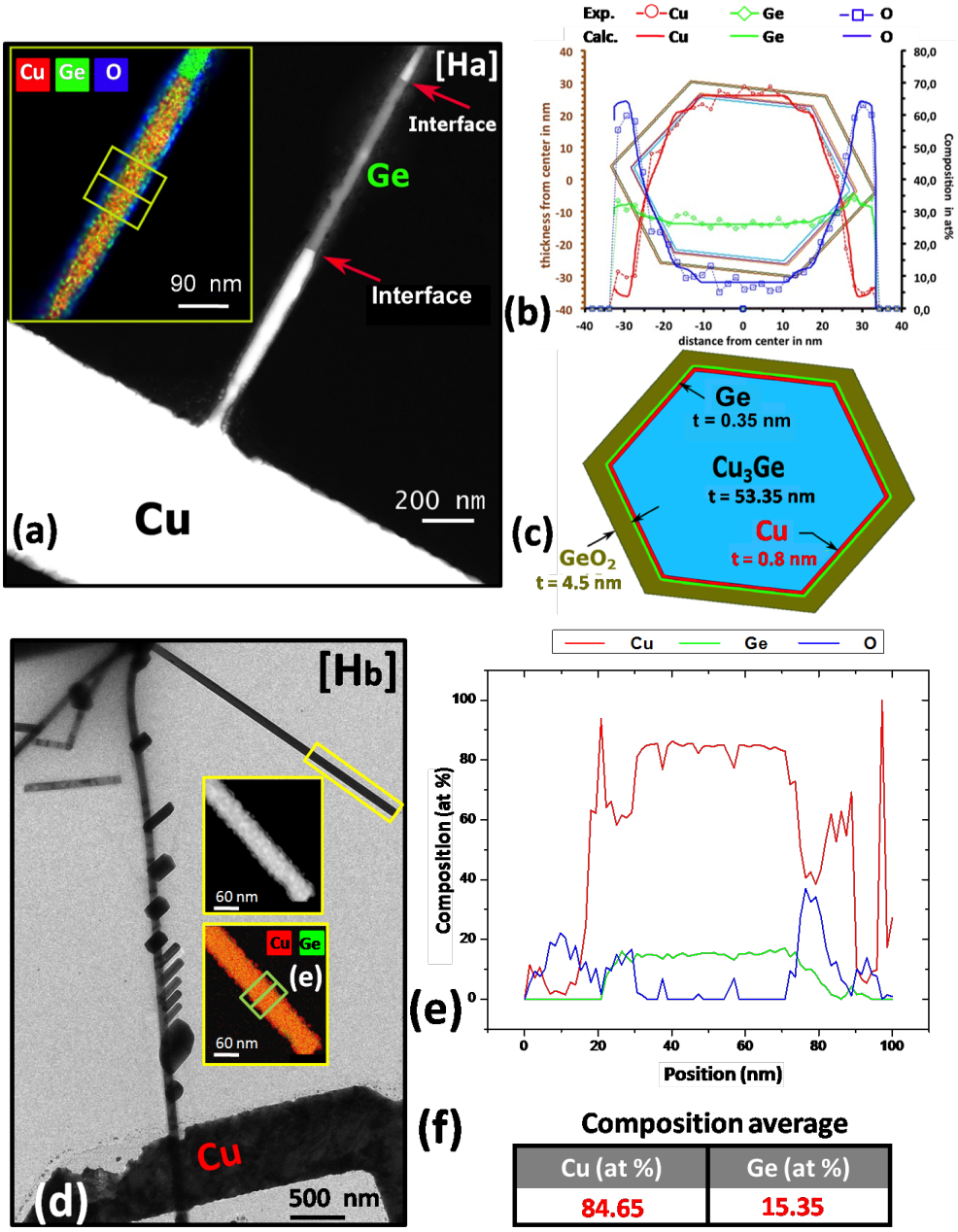

FIGURE 6.8: (S)TEM images and EDX quantification (line scan & hypermap) of different elements (O, Cu, Ge) in the NW after $H_a(V_{heat} = 0.775V)$ and $H_b(T = 600°C)$ experiments. (a) HAADF STEM image of a copper-germanium sample heated using H_a. The inset shows an EDX hypermap of the Cu_3Ge region. (b) Cu, Ge and O average concentration (at%) and local thickness profiles along the line shown in the inset in *a*. (c) schematic of the NW cross-section composed of different core-shell layers after heating. (d) TEM image of a heated sample at ($T = 600°C$) using H_b. Inset images show a HAADF-STEM image and an EDX hypermap of the crystal formed after heating at $T = 600°C$. (e) Line scan of Cu, Ge and O concentration in atom % along the defined region in the inset image in *d*. (f) Local concentration in atom % of both Cu and Ge in the crystal.

to provide enough statistics to probe possible variations in Cu layer thickness, potentially related to the NW radius. To verify the structural analysis realized on the sample heated at 600°C shown above, additional chemical analysis was performed. The EDX analysis was made on the same protruded crystal as shown in Fig.(6.6.a). Fig.(6.8.d) shows a TEM image of the NW after the germanide process and the inset images represent an HAADF STEM image and an EDX hypermap of the selected region, respectively. A concentration profile obtained in the inset of Fig.(6.8.d) is shown in Fig.(6.8.e), showing the quantified concentration in atom % of different elements present, obtained using the Cliff-Lorimer quantification method. The average concentration of **Cu** and **Ge** determined along the line scan is shown in Fig.(6.8.f). The EDX results confirm the previous EDT analysis concluding on the Cu_5Ge phase formation at 600°C. Furthermore, the EDX analysis was extended to the Cu metal pad,

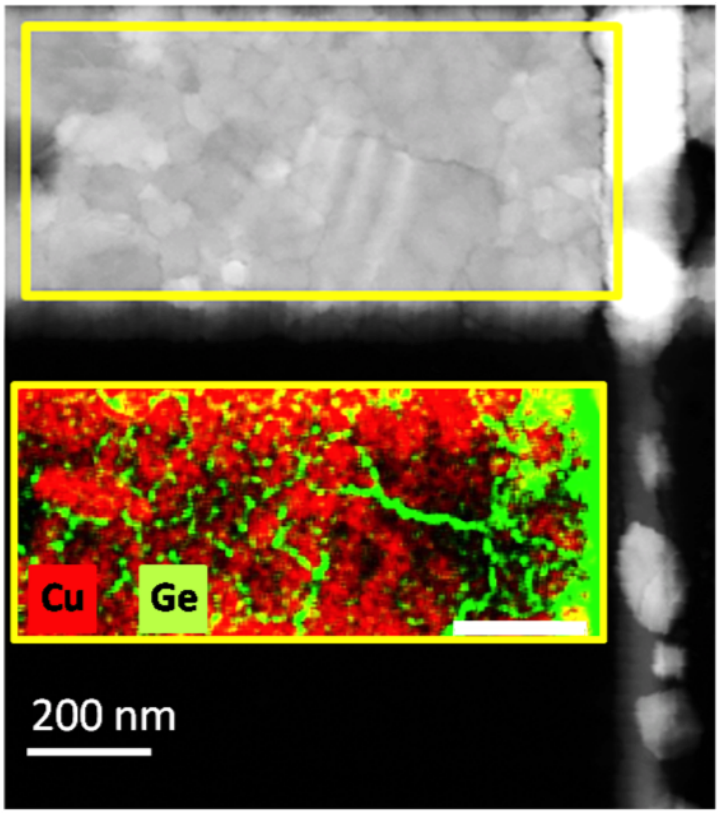

FIGURE 6.9: STEM image and EDX hypermap of Cu and Ge elements present in Cu metal after phase propagation using $H_a(V_{heat} = 1.15V)$. The Ge atoms appear to diffuse in the metal grain boundaries.

revealing contrast caused by grain boundaries in the polycrystalline Cu, see Fig.(6.9). The inset image is an EDX hypermap showing the incorporation of Ge atoms along grain boundaries in the metal. The Ge atom incorporation in Cu grain boundaries was detected on a large area of the Cu metal, revealing an important amount of Ge

atoms exchanged between the NW and the metal during the germanide phase formation. Similar results were found for H_b heating experiments. This result reveals that both species are moving during germanide phase formation.

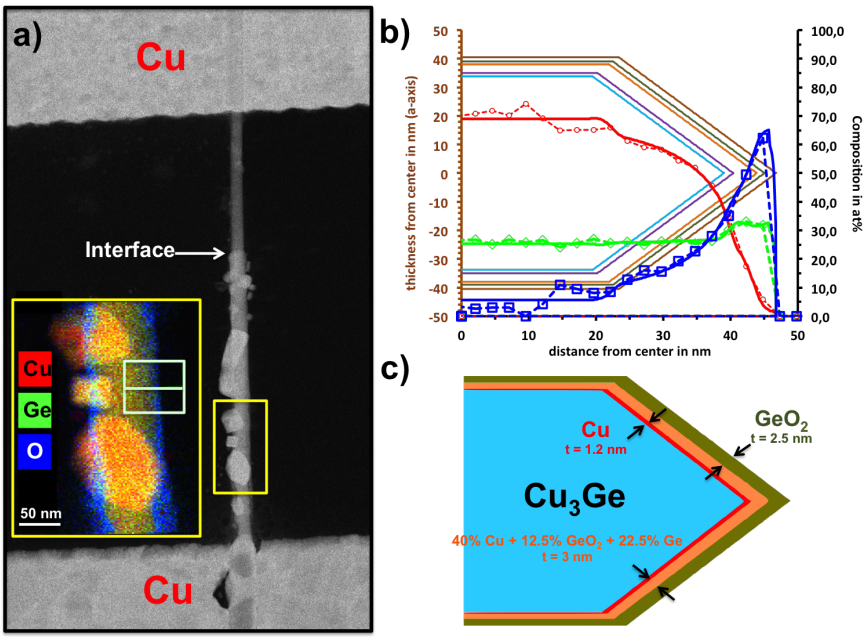

FIGURE 6.10: (S)TEM images and EDX quantification (line scan & hypermap) of different elements (O, Cu, Ge) in the NW after $H_a(V_{heat} = 0.625V)$ experiment. (a) HAADF STEM image of a copper-germanium sample heated using H_a. The inset shows an EDX hypermap of the Cu_3Ge region with the protruding crystals. (b) Cu, Ge and O average concentration (at%) and local thickness profiles along the line shown in the inset. (c) schematic of the NW cross-section composed of different core-shell layers after heating.

6.5 Comparison of Both Joule heating Techniques and Heat Flow Simulations

The choice of using temperature calibrated membranes was to confirm the H_a kinetic data, to have an idea on the temperature where the germanide process takes place and assess the influence of the electron flow in the metal stripline (in H_a experiments) on the germanide reaction initiation. As already mentioned above, the H_b heating experiments revealed an incubation time contrary to the samples where the H_a method was used and where the reaction starts instantly in both NW sides. However in H_a experiments, we have only one observation of propagation in two NWs simultaneously.

Table.(6.3) represents a summary of all performed experiments, were the speed of the reaction front reveals that the H_a heating experiments allow a better control of the germanide propagation compared to the H_b heating experiments, as lower propagation speed can be obtained in H_a. It reveals that the propagation speed, and related diffusion constant, is systematically low in H_a experiments with respect to H_b. Since

TABLE 6.3: Summary of different experiments performed on copper-germanium samples using both H_a and H_b heating techniques. All the samples show a square root evolution of the reaction interface as a function of time except at high temperature were the evolution is linear. A size dependence is clearly visible in the fit-coefficient of the length-curves reported for different diameter NWs heated with both techniques.

Heating	Temperature	Diameter	Curve Behavior	Fit coefficient ($nm/s^{0.5}$)	Remarks
H_b	360 °C	D_{side1} = 31 - 25 nm ; D_{side2} = 37 nm	Square root	B_{side1} = 62.3 ; B_{side2} = can't be fit	Size dependance
H_b	410 °C	D_{side1} = 46.5 nm ; D_{side2} = 59 nm	Square root	B_{side1} = 137.5 ; B_{side2} = 93.3	Size dependance
H_b	600 °C	D_{side1} = 25.5 nm ; D_{side2} = 32 nm	Linear	$(B/A)_{side1}$ = 246.94 nm/s ; $(B/A)_{side2}$ = 194.46 nm/s	Size dependance
H_a	V_{heat} = 0.625 V	D_{side1} = 72 - 62 nm	Square root	B_{side1} = 44.4	—
H_a	V_{heat} = 1.15 V	D_{side1} = 50 nm	Square root	B_{side1} = 22.4	—
H_a	V_{heat} = 0.75 V V_{heat} = 0.75 V	D_{side1} = 22 - 31 nm ; D_{side2} = 32 nm D_{side1} = 22 - 31 nm ; D_{side2} = 32 nm	Square root	B_{side1} = 13 ; B_{side2} = 11.83 B_{side1} = 14.7 ; B_{side2} = 15.12	Crystals show no influence in propagation

H_a experiments are not temperature calibrated, we expect that the temperature is also systematically lower in H_a experiments.
This speculation was confirmed by COMSOL simulations where we relate the heating current I_{strip} to the temperature of the heat source (Cu pad) and calculate the heat transfer to the Ge NW and the opposite Cu pad. The heat transfer is defined as the movement of energy due to a difference in temperature. It is characterized by three mechanisms :

- Conduction : Theoretically it takes place in metals mainly by electrons carrying heat and in other solids by molecular motion which in crystals takes the form of lattice vibrations known as phonons. Typical for heat conduction is that the heat flux is proportional to the temperature gradient.

- Convection : Heat convection (sometimes called heat advection) takes place through the net displacement of a fluid, which transports the heat content in a fluid through the fluids own velocity. The term convection (especially convective cooling and convective heating) also refers to the heat dissipation from a solid surface to a fluid, typically described by a heat transfer coefficient.

- Radiation : radiation takes place through the transport of photons. Participating (or semitransparent) media absorb, emit and scatter photons. Opaque surfaces absorb or reflect them.

In these simulations only conduction and radiation heat transfer phenomena are considered to occur in the Joule heating experiment between the Cu pad and the Ge NW since we are working in vacuum.

6.5.1 Comsol Multiphysics Software

Comsol software [78] is one of the efficient tools that help to describe the behavior of a physical object in various domains of scientific research and engineering calculations. Comsol is a finite element analysis which is the perfect tool to solve partial differential equations. It is also a solver and simulation software package for solving various physics and engineering applications.
To solve the addressed problem using Comsol, we coupled both electric current and heat transfer in a solid module. In order to achieve the simulation, we follow these steps :

1. Assumptions : - we assume working in steady-state conditions - One dimensional heat transfer - Constant properties.

2. Materials properties : we specify material properties as known from bulk studies for the different components of one sample.

3. Boundary conditions : we specify boundary conditions and assume the metal contacts outside the membrane are at room temperature.

4. Analysis : heat transfer using Fourier's law to solve the conduction heat transfer from the Cu metal to the other contacted systems (nanowire, Cu metal, membrane) and radiation by taking into account the heat loss with the external environment.

We built the membrane with the contacted NW similar to the real sample and we applied the same experimental conditions. A heating current (I_{strip}) through the metal is defined that allows to start the reaction, therefore, a heat transfer from the metal

(heat source) to the contacted NW and the Si_3N_4 membrane occurs.
A part of the materials properties presented below are from Comsol library and the values underlined are taken from literature where the properties are determined experimentally in order to achieve a reliable simulation of the system. We applied a

TABLE 6.4: Material characteristics used for the Comsol Simulation.

	Ge	**Si_3N_4**	**Si**	**Cu**
Heat Capacity C_p $(J.Kg^{-1}.K^{-1})$	310	700	678	384
Thermal Conductivity k $(W.m^{-1}.K^{-1})$	14 [79]	2.5 [80]	34	401
Electrical Conductivity σ $(S.m^{-1})$	0.28 [81]	10^{-15}	1	4.1×10^{7} [82]
Relative permetivity ϵ	16.3	7	4.5	1
Density ρ $(Kg.m^{-3})$	5323	3000	2320	8960

voltage difference on both metal sides, the voltage was adjusted to reproduce the same current density determined experimentally in the metal stripline $\sim 10^{-11}$ A/m^2. Fig.(6.12.a,b) represents the temperature distribution in a direct Joule heating exper-

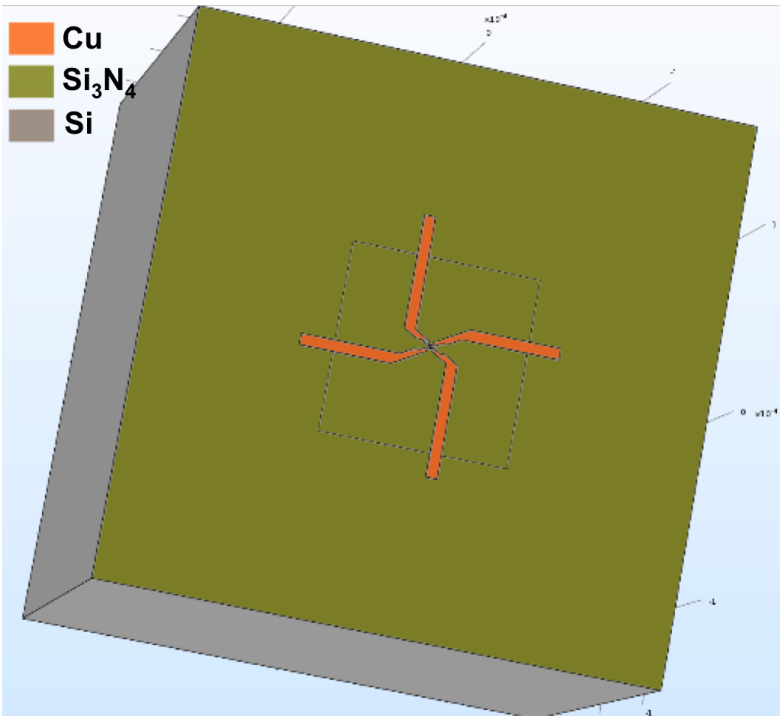

FIGURE 6.11: Schematic representing a silicon nitride membrane on top of a silicon substrate where a Ge nanowire is contacted from both sides by a Cu metal.

iment [H_a]. The Comsol simulation shows a temperature gradient along the Ge NW, visualized in more detail in Fig.(6.13), expected from the kinetic plots $L \sim \sqrt{t}$ (see inset Fig. 6.1.d) where a slope change was observed in an [H_a] heating experiment. The determined temperature when a heating current ($I_{heating}$ = 0.0143A) flows through

the Cu metal corresponds to a temperature T = 240°C. In the following, we compare three samples studied in H_a experiments, see Table.(6.3) and Table.(6.5).

The three samples in H_a experiments (see Table.(6.5)) show a similar heating current ~ [0.014 - 0.016 A], however, the measured metal resistance during the heating experiment are not the same. Therefore, the power dissipated in each of the three samples is not the same. Regarding the injected power we expect the fastest propagation in sample 2, while the fastest propagation is observed in sample 1, see Table.(6.5). The slowest propagation is observed in sample 3, while it has the smallest NW diameter and the intermediate power injection. One reason explaining these results is that the resistance of the metal strip depends on the metal micro-structure, the size of crystal grains and the crystal grain size evolves during the annealing experiment leading to a changing relation between resistance, resistivity and temperature.

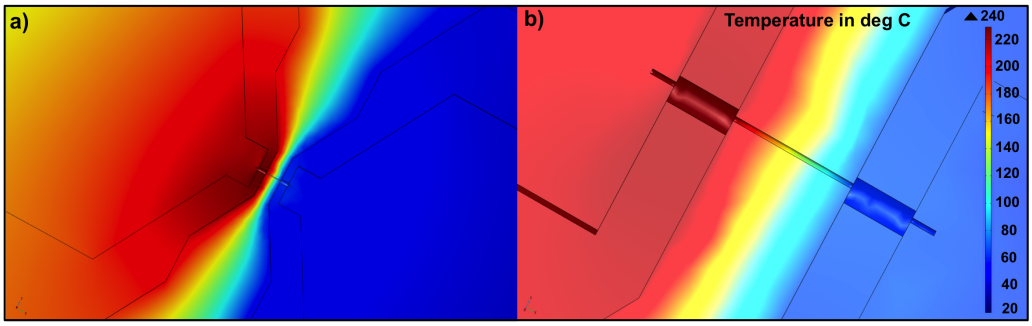

FIGURE 6.12: Temperature distribution in the heated device during *direct* Joule heating. a) The heat distribution when a heating current $I_{heating}$ = 0.0143 A flows through the Cu metal and rises the temperature to a T_{max} = 240°C in the contact area between the Cu metal and Ge NW. b) Zoom to represent the temperature gradient along the Ge NW.

TABLE 6.5: Experimental data of the heated samples during direct Joule heating experiments [H_a].

Sample	V_{heat} (V)	$I_{heating}$ (A)	R_{strip}(Ω)	P (W)	D (nm)	Fit (nm/s$^{0.5}$)
Sample 1	0.625	0.0143	43.5	0.009	72 - 62	44.4
Sample 2	1.15	0.015	76.45	0.017	50	22.4
Sample 3	0.75	0.0153	49	0.011	22 - 31	13

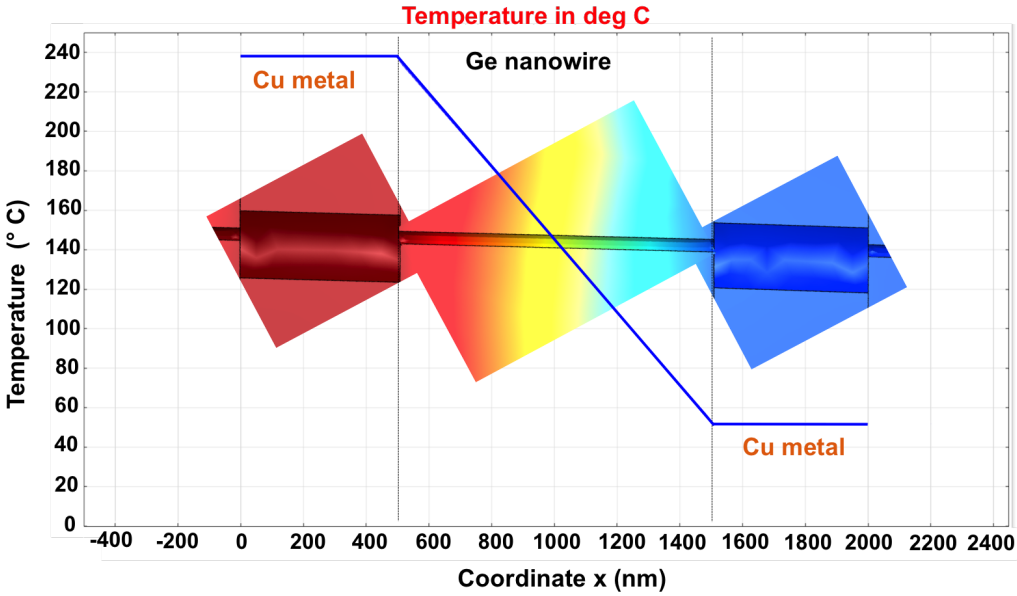

FIGURE 6.13: Temperature profile starting from the end of the heated side to the end of the Cu contact on the other side ($I_{heating}$ = 0.0143 A) in [H_a] heating experiment.

6.6 Discussion and Modeling

6.6.1 Kinetic study

In the following, we will combine both kinetic and structural analysis results to provide a better understanding of the Cu-germanide growth rate in a Ge NW. Once the reaction starts and the formation of Cu_3Ge under the metal occurs, it starts to propagate in both NW sides as shown in Fig.(6.2). We have analyzed the apparition of the reaction interface in the NW on both sides of the metal strip. Extrapolation of the location of the interface to its nucleation point, that is hidden underneath the strip, using the propagation speed, indicates that the nucleation takes place in one point contact between the metal and the NW, contrary to the Al/Ge system, this will be shown later in chapter 7.

We notice a square root behavior of the reaction interface as a function of time in all heated samples following eq.(2.17), except for the H_b experiment at 600°C, where the germanide front progresses linearly as a function of time. The germanide growth rate at low temperature appears therefore to be limited by a diffusion process. As observed in Fig.(6.1.b) and Fig.(6.2.d,f), the propagation rate is systematically faster in small diameter NWs. According to the model presented by [24, 41, 61] an influence of the radius indicates a reaction limited by surface diffusion, which is consistent with the EDX observations of a pure Cu and Ge shell close the NW surface, at the Cu_3Ge

- GeO_2 interface. Several papers have presented kinetic studies of metal phases in semiconducting NWs [24, 25, 41, 59], mostly on the NiSi system. In these studies, surface diffusion was reported to be the rate limiting factor of the metal phase propagation. In all these previous studies, metal atoms have been reported as the only or the dominant diffusing species during silicide phase formation. Therefore, the diffusion models presented in all these former studies follow the diffusion of metal atoms from the metal pad (reservoir) through a small layer δ on the intermetallic segment to react with the semiconductor atoms at the interface. In addition, Cu atoms are the dominant diffusing species in the NW, since Cu atoms present in the Cu_3Ge segment represent around 2 times the number of Ge atoms incorporated in the metal grain boundaries after Cu_3Ge phase formation, as can be shown from basic calculations presented below.

6.6.1.1 Calculation exchanged Cu and Ge atoms

This basic calculation allows to estimate the dominant diffusing species between Cu and Ge atoms, based on the experimental data of Fig.(6.1). After the germanide phase formation, we noticed that the NW diameter increases only with few nm. Therefore, to simplify the calculation we assume that the diameter didn't change after Cu_3Ge phase formation.

Number of Ge atoms/nm^3:

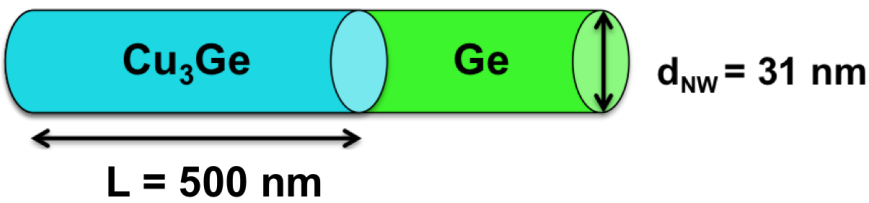

FIGURE 6.14: Schematic illustrating the section of the transformed Ge NW before and after H_a and H_b heating experiments.

$$C_{Ge} = \frac{Z}{V_{Ge}} = \frac{8}{(0.565)^3} = 44.35\ atom/nm^3$$

Volume of the NW segment exchanged into Cu_3Ge:

$$V = \pi R^2 L = \pi \times (15.5)^2 \times 500 = 3.78\ 10^5\ nm^3$$

Number of Ge atoms present in the NW segment before it exchanges to Cu_3Ge is :

$$N^i_{Ge} = 44.35 \times 3.78\,10^5 = 1.67\,10^7\ atom$$

In the orthorhombic Cu_3Ge phase structure, the lattice points per unit cell are : Cu (Z = 6) and Ge (Z = 2) and the structure volume V = 0.457 × 0.527 × 0.42 = 0.101 nm^3. Therefore, the number of Ge and Cu atoms in the Cu_3Ge phase/volume are :

$$C'_{Ge} = \frac{Z_{Ge}}{V} = \frac{2}{0.101} = 19.8\ atom/nm^3\,; \quad C_{Cu} = \frac{Z_{Cu}}{V} = \frac{6}{0.101} = 59.4\ atom/nm^3$$

The number of Ge and Cu atoms present in the Cu_3Ge segment (shown above) are :

$$N^f_{Ge} = 19.8 \times\ 3.78\,10^5 = 7.48\,10^6\ atom\,; \quad N_{Cu} = 59.4 \times\ 3.78\,10^5 = 2.24\,10^7\ atom$$

So, from the N^i_{Ge} and N^f_{Ge} values we could estimate the number of Ge atoms that diffused from the NW to the Cu pad grain boundaries.

$$N^{diff}_{Ge} = N^i_{Ge} - N^f_{Ge} = 1.67\,10^7 - 7.48\,10^6 = 9.22\,10^6\ atom \sim 10^7\ atom \tag{6.1}$$

To estimate the order of magnitude of Cu atoms introduced into the Ge segment compared to the Ge atoms diffusing into the Cu grain boundaries during the Cu_3Ge phase formation we write:

$$\frac{N_{Cu}}{N^{diff}_{Ge}} = \frac{2.24\,10^7}{10^7} = 2.24 \tag{6.2}$$

We see from this small calculation that twice as many Cu atoms diffuse with respect to diffusing Ge atoms. This could be an argument that the dominant diffusing species is Cu atoms during the Cu_3Ge phase formation.

6.6.2 Interpretation of Diffusion model

However, both the kinetic studies as well as the EDX results shown above, present clear evidence for both Cu and Ge surface-diffusion on the Cu_3Ge NW segment (as illustrated in Fig.(6.15)). Therefore, two diffusion scenarios are possible:

A first scenario can be an interdiffusion of both Cu and Ge through a surface layer δ at the Cu_3Ge - GeO_2 interface, where a Cu_xGe_y solid solution is created. Therefore, a concentration gradient should be present between the germanide/Ge and the

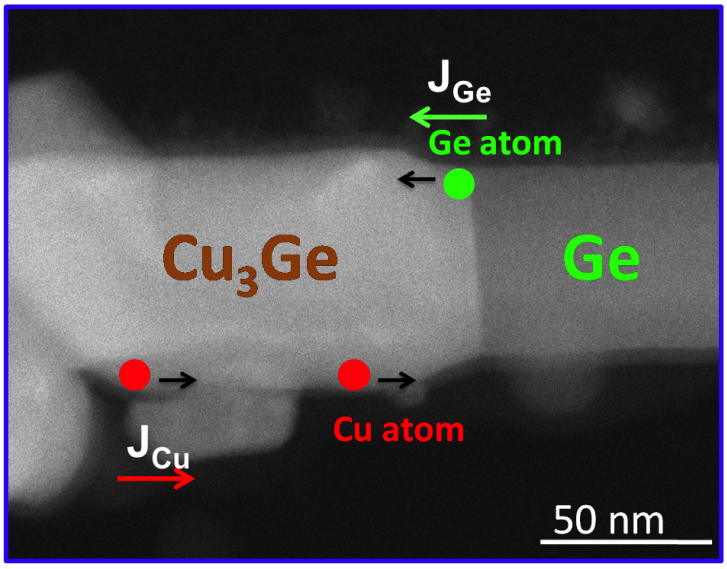

FIGURE 6.15: High magnification HAADF STEM image of Cu_3Ge - Ge interface in HAADF-STEM with schematic indicating both Cu and Ge surface diffusion.

germanide/reservoir interfaces, allowing a continuous diffusion of both Cu and Ge atoms during the heating experiments. After heating (at ambient temperature) a separation of the solid-solution in two layers occurs and it is detected in the ex-situ EDX analysis.

A second scenario is the presence of both surface and volume diffusion of both Cu and Ge species. The surface diffusion occurs in a similar manner as described above and the additional volume diffusion occurs through the defects present in the Cu_3Ge segment.

This latter scenario can't be excluded since planar defects were detected in the protruding crystals by STEM imaging (see Fig(6.16)). Furthermore, the presence of point defects in the Cu_3Ge segment can't be excluded, potentially contributing to the volume diffusion.

However, the first scenario is entirely supported by the experimental results where the kinetic results show the radius dependency of the propagation speed and EDX reconstruction of the NW cross-section reveals clear evidence on the presence of a surface layer where a diffusion of both Cu and Ge atoms occur during the heating experiments. Hence, we tend to explain the mechanism of the Cu_3Ge phase formation by the first scenario of pure surface diffusion. Even if volume diffusion takes place, the surface diffusion will be the dominant diffusion mechanism during the Cu_3Ge phase formation.

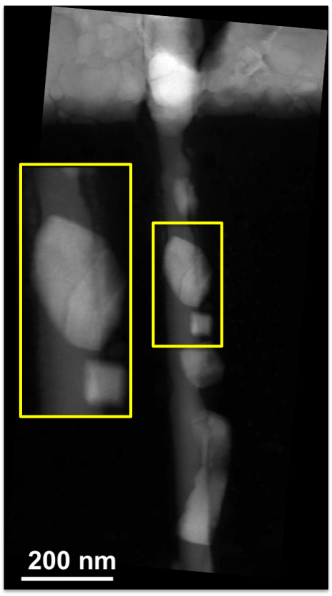

FIGURE 6.16: STEM image showing grain boundaries present in the protruding crystals after phase propagation using H_a (V_{heat} = 0.625 V).

6.6.2.1 Additional EDX analysis

We performed an additional chemical analysis (EDX) along the germanide segment in order to determine the concentration gradient along the germanide segment and deduce the diffusion limiting species. Therefore, if Cu diffusion is the rate limiting step, we expect the presence of a concentration gradient in the layer δ along the germanide segment where a Cu-rich region will be detected near the Cu reservoir and a Cu-poor regions will be detected near the Cu_3Ge/Ge NW interface. A similar scenario for the Ge layer thickness is expected to be observed if the Ge diffusion is the rate limiting step. EDX results shown in Fig.(6.17) performed several months after initial heating experiment, reveal interesting results.

Fig.(6.17.a) represents an hypermap of the NW presented above in Fig.(6.10) near the Cu reservoir. In Fig.(6.17.b), the NW thickness and its shape are determined. The NW is well modelled by a hexagonal structure as its shown by the fit (brown line). However, we couldn't fit the entire thickness profile, but after quantification of the cross-section marked by the yellow box in Fig.(6.17.a), this excess is attributed to GeO_2 (Fig.(6.17.b)).

In (Fig.(6.10.b)) and (Fig.(6.17), the reconstruction of the germanide cross-section demonstrates the transformation of the NW core to Cu_3Ge surrounded by three layers of **Cu**, **Ge** and **GeO_2**, respectively, with different thicknesses. As we can notice in Fig.(6.17.c), these surrounding layers and a part of the Cu_3Ge were oxidized even if

the sample was stored under vacuum in a desiccator. **GeO_2** and **CuO_2** are the oxides present with Cu_3Ge in the layer represented with the green hexagon in Fig.(6.17.c). As we can see in Fig.(6.10), the reconstructed zone of the germanide NW was roughly halfway between the Cu reservoir and the reaction interface. Fig.(6.17) represents a reconstruction near the Cu(reservoir)/Cu_3Ge NW interface and it reveals the presence of an excess of GeO_2 surrounding the NW (see Fig.(6.17).b,c) as compared to NW region closer to the reaction interface represented in Fig.((6.10). b, c). This excess of GeO_2 informs on the presence of an important amount of Ge at the Cu/Cu_3Ge interface at the end of the heating experiment. This result indicates the presence of a limitation in the Ge intrusion through metal grain boundaries. Ge is apparently diffusing more easily through the surface diffusion layer than in the metal grain boundaries, and therefore piles up before entering the Cu metal strip. However, it should be noted that this effect is not the rate limiting step of the reaction, since in that case a linear relation of the reacted region L with time would be expected eq.(2.18) and [41]. Therefore our results indicate that indeed Cu surface diffusion on the Cu_3Ge segment is the rate limiting step.

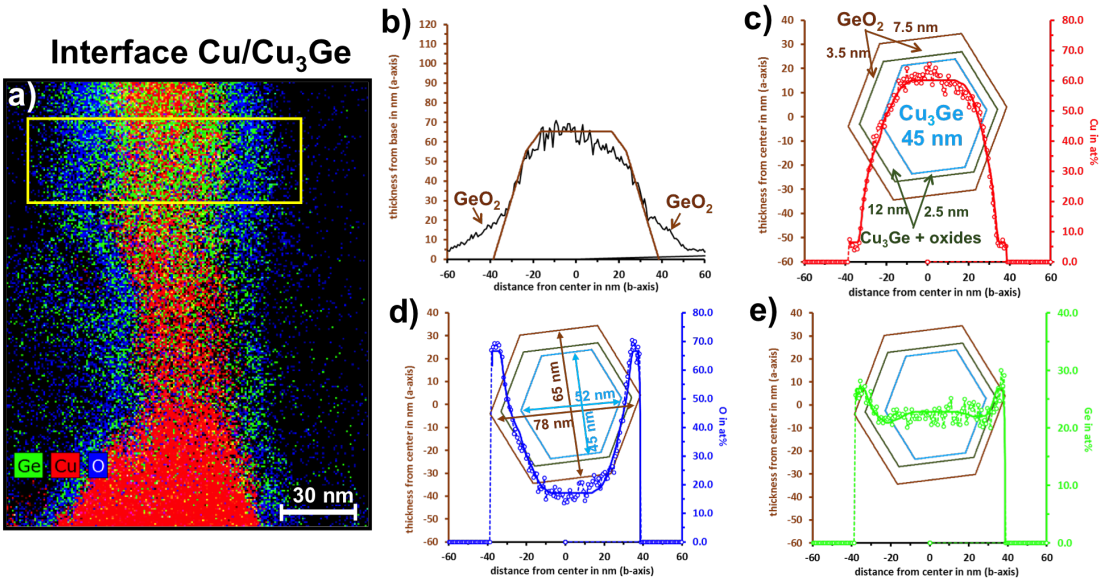

FIGURE 6.17: EDX hypermap and quantification of different elements (O, Cu, Ge) in the NW after $H_a(V_{heat} = 0.625V)$ experiment. a) EDX hypermap of the germanide NW, the yellow box shows the reconstructed cross-section. b) Local thickness calculated from the detected signal (black line) and corresponding profile (brown line) simulated for hexagonal cross-section. c, b, d) Cu, Ge and O average concentration (at%) distributed along the different layers representing the reconstructed Cu_3Ge cross-section.

6.6.3 Discussion

It should be noted that the hypothesis that Cu surface diffusion on the germanide segment is the rate limiting step doesn't appear consistent with the observation in Fig. (6.1.a), where the propagation in both sides of the NW on opposite sides of the Cu contact with and without the appearance of clusters showed a very similar propagation speed. We would expect that for such an experiment, the propagation is faster if no protruding crystals appear on the NW germanide surface, as this means loss of the rate limiting Cu material, and is therefore expected to decrease the reaction interface propagation. On the other hand, it was also observed that if the germanide entered a crossing NW, the propagation speed decreased in the original NW (see Fig. (6.3)), which is an observation that could be explained by Cu diffusion being the rate limiting step. We speculate therefore that in the upper part of the NW in Fig. (6.1.a) a diameter increase of the germanide occurs, that almost exactly balances the appearance of clusters in the lower NW part in terms of Cu quantity, leading to a very similar reaction interface propagation.

However, no Cu concentration gradient was detected. The inability to detect a concentration gradient along the NW segment is related to the fact that we try to detect a variation of the amount of Cu atoms in a ~ 2 nm layer. At this layer thickness, we are in the limit of the accuracy of the quantification method.

The question now is why Ge atoms prefer to diffuse trough the germanide surface instead of diffusing in the Ge NW (giving rise to a Ge self-diffusion), the answer is presented in Table.(6.6) where the Ge self-diffusion coefficient is very low. Therefore, the diffusion of Ge atoms on the surface of the Cu_3Ge segment is energetically favorable.
To resume the germanide (Cu_3Ge) growth rate mechanism two phenomena need to be considered :

- First, the interface between the deposited metal and the Ge NW. The diffusion of Cu atoms in the Cu_3Ge segment occurs through the Cu/Cu_3Ge interface where Cu and Ge atoms diffuse in in opposite directions. Initiation of the reaction was shown to depend on the quality of the Cu-Ge NW interface.

- Second, the Cu atoms diffuse mostly through a small layer δ on the germanide surface to react with the Ge atoms present at the Cu_3Ge/Ge NW interface. Ge

atoms diffuse through the same layer on the germanide surface which potentially creates a CuGe solid solution in the layer δ where a concentration gradient is present along the NW axis. The Ge atoms don't influence the kinetics of the germanide growth rate and metal diffusion is the rate limiting step.

TABLE 6.6: Diffusion coefficients of Cu and Ge systems at 500°C.

	Copper	Copper	Germanium	Copper
in	Germanium	Cu_3Ge	Germanium	Copper
D ($cm^2.s^{-1}$)	3.06×10^{-6} [46]	$10^{-10}-10^{-8}$ [83]	9.34×10^{-20} [84]	3.04×10^{-4} [85]

Furthermore, the kinetic model that we presented in subsection 2.5.7, which presents three potential rate limiting steps similar to [41] expressed as a function of Cu atoms, allows to fit and explain all the kinetic data represented above either at low or high temperatures. The surface diffusion equation resulting from eq.(2.30) is written as follows :

$$L = \sqrt{Bt} = \sqrt{\frac{C_{res}}{N}\frac{\delta}{R}4D^s t} \tag{6.3}$$

δ is the thickness of the near surface-diffusion layer obtained from the EDX experiments, we assume δ = 1 nm. We applied this equation on the data shown in Table.(6.3) and we find the surface-diffusion coefficient of Cu at different temperatures summarized in Table.(6.7). It can be seen from Table.(6.3) that the propagation speed, and related diffusion constant are systematically lower in H_a experiments with respect to H_b. Since H_a experiments are not temperature calibrated, we expect that the temperature is also systematically lower in H_a experiments. Since in H_b experiments at lower temperatures no reaction was observed, this could indicate that the presence of an electrical current in the metal strip on the NW could facilitate nucleation of the Cu_3Ge phase. Interestingly, we notice a different growth rate in the

TABLE 6.7: Calculated surface-diffusion coefficients

	Heating	Power (mW)	Plasma	D(cm^2/s)	D$_2$(cm^2/s)
				Bulk Diffusion	Surface Diffusion
H_b	T = 360 °C	—	30 s	1.94×10^{-11}	2.3×10^{-11}
—	T = 410 °C	—	—	9.4×10^{-11}; 4.35×10^{-11}	1.91×10^{-10}

opposite NW sides (see Table.6.3) for the heated sample at 410°C. Thus, we applied eq.(6.3) with the aim to determine D^s in the Cu_3Ge NW at 410°C in both sides (L_{side1} and L_{side2}). In order to provide a common D^s, we found that $\delta_1 = 1.7\ \delta_2$. This might reveal that the diffusion of Cu through the smaller segment occurs through a thicker

Cu layer. This result was not yet experimentally verified due to a lack of characterized NWs so far. However, we need to keep in mind that this layer thickness is detected after the end of the heating experiments. Therefore, during the heating experiment the thickness δ of the surface diffusion layer could be different.

At 600°C, we observed a linear reaction between L and t influenced by the NW diameter. According to Tang et al [41] this can indicate a reaction limited by the metal-NW interface or the germanide-Ge NW interface. However, in the first case an influence of NW diameter is expected where no diameter influence is expected for the second case. According to the eq.(2.18) and eq.(2.30) this can therefore indicate a reaction limited by the metal-NW interface as a diameter influence was observed. Two possible explanations can be proposed for the linear growth rate behavior based on eq.(2.30). Either the diffusion through the metal is very slow compared to the diffusion through the wire itself, or the contact section where the diffusion occurs in the metal is very small with respect to the NW section. Initially, we aimed to measure the reaction activation energy. According to Yaish et al [24] the metal/NW interface quality is an important parameter influencing the propagation growth rate. Indeed, in our experiments, we noticed an influence of the surface quality on the reaction initiation. Therefore, it will be possible to deduce the activation energy from the D^s at different temperatures, but first we need to establish a good protocol allowing the reaction to start simultaneously in all contacted NWs to avoid any influence of the interface on the germanide growth rate during the different heating experiments.

6.7 Conclusion

In summary, this section presents a detailed TEM in-situ study of the solid-state reaction using direct Joule heating H_a and controlled temperature H_b heating experiments, where H_a shows a better control of the germanide growth rate. We formed Cu_3Ge heterostructures at temperatures below 600°C and a copper rich Cu_5Ge phase at 600°C. Kinetic analysis of the germanide segment length as a function of time using both types of heating experiments shows size dependancies. The rate limiting step appears to be Cu surface diffusion and the Cu/germanide interface seems to be the critical factor for the germanide reaction initiation and can possibly influence the growth rate below 600°C. These results are supported by a quantitative EDX model revealing formation of a double core-shell structure , with a Cu_3Ge core covered by

thin double shell layers of pure Cu and Ge, with an estimated average thickness of 1 $\pm$ 0.2 nm of Cu and 0.35 nm of Ge. Additional characterization by electron diffraction and electron diffraction tomography was performed to determine the different crystal phases. Direct Joule heating experiments appear to be a powerful tool to develop and control short channel metal oxide semiconductor transistors down to sub-10 nm length scales independently of the spatial resolution of an lithography process. This technique allows to perform electrical characterization during the heterostructure phase formation.

Chapter 7

TEM Study of Al-Ge (NW) Solid-State Reaction

In this chapter the solid-state reaction of Al and Ge NWs similar to Cu and Ge NWs system (chapter 6) is triggered in-situ in a TEM using both H_a and H_b Joule heating techniques. The location of the interface was followed as a function of time in section 7.2, and the corresponding observations were explained in section 7.6 by the diffusion model presented in chapter 2. Similar to chapter 6 on Cu-Ge NWs system, the reaction didn't start uniformly over all the NWs and we used different NW preparations in order to determine the influence of the initial Al-Ge interface. The structure of the transformed region was studied ex-situ using HRTEM by a collaborator in Vienna and confirmed by electron diffraction in section 7.3. A 3D EDX reconstruction of a cross-section of the transformed region is presented in section 7.4. In-situ TEM heating and biasing measurements were performed using the H_a heating technique, allowing us to follow the evolution of the electrical resistance of the Al/Ge/Al NW heterostructure. These results are presented in section 7.5.
In section 7.6, we combine all the experimental results in order to understand the rate limiting step governing the Al-Ge solid-state reaction. The last part of this chapter, section 7.7, presents the electrical results published with and by our collaborators Alois Lugstein's group, where they showed that the Al/Ge NW system has potential applications in several domains. However, one of the issues faced in their results [14, 16] is to control the length of the unreacted Ge NW below 500 nm. Therefore, using the H_a heating technique could allow a better control of the Al propagation in the Ge to form small Ge segments then can be obtained using conventional heating techniques.

7.1 In-situ Phase Propagation of The Al-Ge (NW) System

The same experimental procedure as described in section 6.1 was followed both for the fabrication, the in-situ experiments and the data acquisition in the TEM. Contrary to the structure of chapter 6 (section 6.2), we will present both H_a and H_b heating experiments in the same section, since the propagation speed in H_a experiments appeared to be comparable to the low temperature H_b experiments, see chapter 6, as confirmed by heat flow calculations, see section 6.5, and this was also observed on the Ge-Al couple. Then, we present the kinetic results at high temperature using the membrane-substrate heating technique H_b.

7.2 Kinetic study of the Al-Ge Exchange Reaction

All the experiments were performed in-situ in a Philips CM300 TEM at 100 kV to provide a nm-scale spatial resolution, which allow to follow all the phenomena occurring during the aluminium-germanium solid-state reaction. We follow the location of the reaction front in real time to get insight into the dynamics of the diffusion process and compare with diffusion models. In the following, we present 6 heated samples where in 3 samples we used H_a and in the 3 others the H_b heating technique.

7.2.1 Al-Ge (NW) at Low Temperature

In Fig. (7.1) several heating experiments are shown : heating using H_a (Fig. (7.1.a)) in a metal strip on the Ge NW, and H_b in Fig. (7.1.c, e) at 280°C and 330°C, respectively. Movies of the Al-Ge exchange using both heating techniques are shown in videos (Al-Ge (M_1 - H_a), Al-Ge (M_2 - H_b - 250 and 280°C) and Al-Ge (M_3 - H_b - 330°C)). The difference between the two heated samples at 280 and 330°C is the metal deposition (sputtering + evaporation), where sputtering was performed in two different machines. This is translated by a change in the temperature where the Al-Ge reaction is initiated. In the sample shown in Fig. (7.1.c) the reaction was initiated at 250°C, while in the sample shown in Fig. (7.1.e) the exchange starts only at 330°C. As can be noticed from Fig. (7.1) the contrast change in the Ge NW in BF images indicates the metal intrusion in the NWs. To investigate the kinetics of the metal

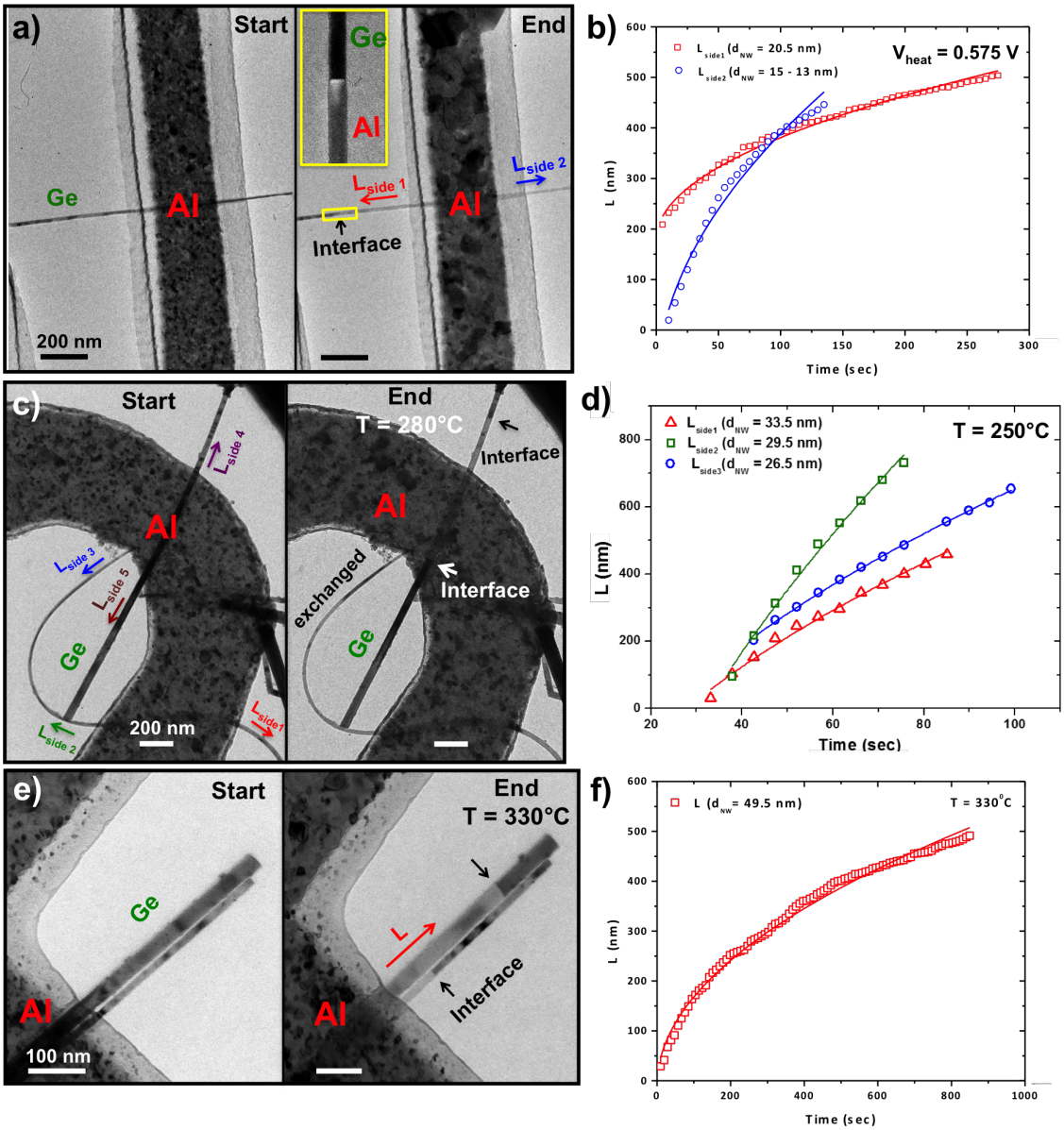

FIGURE 7.1: In-situ aluminum-germanium propagation experiments using either in situ H_a and H_b. a) TEM image showing the sample heated using in-situ H_a, the 2 sides have different NW diameters. b) The length of transformed segment versus time at $\Delta V = 0.575V$ using in-situ H_a for both opposite propagation directions L_{side1} (□ ; fit (—)) and L_{side2}(∘; fit (—)). c, e) TEM images of in-situ heating experiments H_b at two different temperatures (250 - 280°C) and 330°C, respectively. The NWs in these images have different NW diameters. d, f) The length of the transformed segment versus time at two different temperatures 250°C and 330°C. d) The length of the segment versus time at 250°C in the curved NW L_{side1} (△ and fit (—)), L_{side2} (□ ; fit (—)) and L_{side3} (∘ ; fit (—)). f) The length of the transformed segment at 330°C on the big NW L (□; fit (—)). Profiles in *b*, *d* and *f* can be well fitted with a square root function eq.(2.17).

intrusion, we followed the progress of the propagated phase as a function of time, where L is the distance the reaction interface has travelled. Three different examples

of these traces are presented in Fig. (7.1), where both H_a and H_b heating techniques were used. The shown traces were realized by H_a at V_{heat} = 0.575 V and by H_b at 250 - 280 and 330°C, respectively. The metal intrusion started to take place in L_{side1} before L_{side2} at a lower V_{heat} = 0.525 V, as it can be noticed in Fig. (7.1.b): observe that L_{side1} starts at L = 200 nm as the reaction initiated in this side at lower heating current than L_{side2} and only the traces at constant heating power are represented here. The propagation speed is faster in L_{side2} with respect to L_{side1}. Fig. (7.1.c) shows TEM images of a heated sample at both 250 and 280°C where the propagation was followed only in the curved NW (L_{side1}, L_{side2} and L_{side3}) at 250°C, since in the straight NW (L_{side4}) the interface position was not very clear (presence of diffraction contrast) during the reaction. The metal intrusion in the Ge NW started at 250°C only in the curved NW. Unfortunately, this was not noticed during the in-situ TEM H_b experiment, and therefore we increased the heating to 280°C, where the metal intrusion starts to take place in L_{side4}, whereas the curved NW was fully exchanged as can be seen in Al-Ge (M_2 - H_b - 280°C). The plot describing the evolution of the interface as a function of time in the different sides of the curved NW at 250°C is presented in Fig. (7.1.d), showing the evolution of the interface in the three NW sides. From the plot in Fig.(7.1.d) we see clearly the length $L_{side1} < L_{side3} < L_{side2}$ where the NW diameters are $d_{NW3} < d_{NW2} < d_{NW1}$. In Fig. (7.1.e) TEM images of two Ge NWs contacted by the same Al strip line are shown before and after heating at 330°C. The propagation front was followed as a function of time only in the big NW since the interface was not easily detected in the small NW during the heating experiment.

The propagation speed varies from one NW to another and as can be observed in Fig. (7.1.b, d) the propagation speed cannot be related to the NW diameter. Therefore it appears that the metal intrusion growth rate varies from one sample to another. This result contradicts Kral et al [14], where they attest that the Al-Ge NW exchange is size dependent in all their heated samples. However, in [14] no in-situ experiments were performed, therefore, observed propagation speeds can be interpreted correctly only if the reaction initiates in all NWs simultaneously, which we know is unlikely. Indeed the graph showing propagation speed as a function of NW diameter in [14] is characterized by a large scatter of data points.

Furthermore, as it can be seen in Fig. (7.1.c) and Fig. (7.5), the exchange didn't start in both NW sides. We observed in a series of images (see Fig. (7.2)) taken during an H_a heating experiment that the reaction starts to occurs in many nucleation points underneath the Al stripline.

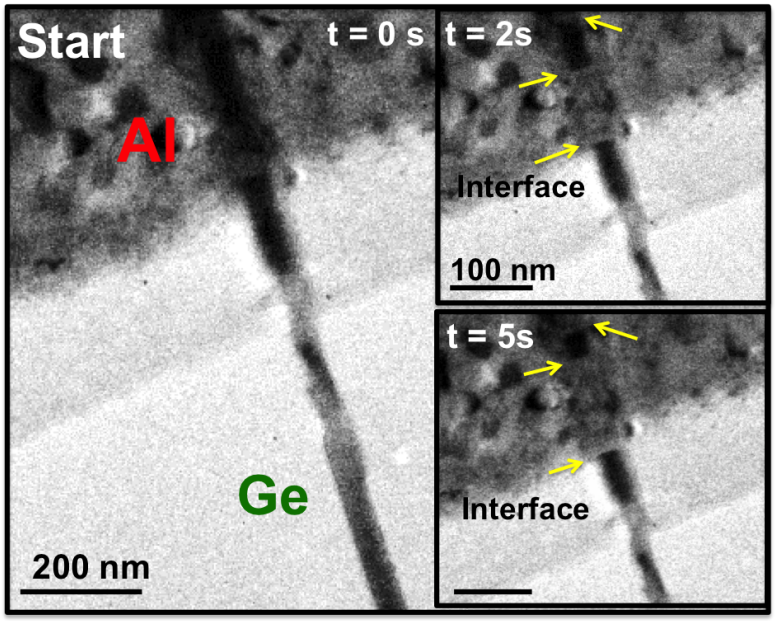

FIGURE 7.2: TEM images during an in-situ TEM H_a heating experiments where we see clearly the multiple nucleation sites of the formed heterostructure in the Ge NW.

7.2.2 Al-Ge (NW) at High Temperature

During the H_b heating experiments at 280°C, the reaction did not start in the thicker NW part of L_{side5} as shown in Fig. (7.1.c). Therefore, the heating was increased with the aim to activate the metal intrusion in the NW. The propagation started to occur at 400°C and the reaction front progress was followed as a function of time in Fig. (7.3.b). The evolution of the interface at 400°C (Fig. (7.3)) shows a different behavior compared to the plots shown in Fig. (7.1.b, d, f). At 400°C, the interface appears to move very fast during a short period of time, alternated with a static interface. In other words : the movement of the interface appears to take place in tens of nms sized steps, instead of a continuous movement as observed in all previous experiments, resulting in a stepwise growth. A similar behavior as observed in Fig.(7.3)), though with a much smaller step size, was observed in Si [110] and Si [111] NWs during Ni [86] and Co [21] point contact reactions, respectively, performed in-situ in a ultrahigh vacuum TEM at 700 and 800°C where the propagation was observed to occur in steps ranging from one to several atomic planes. Additional heating experiments were performed on an Al-Ge NW sample by in-situ TEM H_b heating at 580°C (see Al-Ge ($M_4 - H_b - 580°C$)). The plot of the interface evolution as a function of time is not shown, since the interface was not very well visible during the heating experiment. However, this sample shows a very interesting result where two contacted

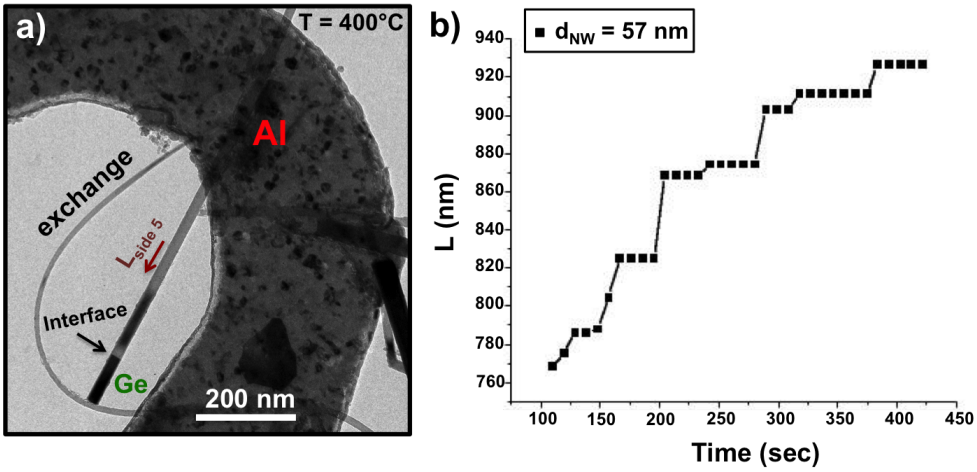

FIGURE 7.3: In-situ aluminum-germanium propagation experiments using Joule heating [H_b]. a) TEM image showing the sample heated using in-situ [H_b] at 400°C. b) The length of the segment versus time at 400°C in the straight NW L showing a stepwise growth.

NWs with different diameters contacted by the same metal strip line showed different propagation speed and a competition of the two interfaces is observed. However, on average the propagation speed is found to be much higher in the thicker NW.
From these results shown at low and high temperatures it appears that the interface propagation speed doesn't depend on the NW diameter. However, another parameter that can potentially influence the reaction initiation is the metal NW interface quality [61].
We took advantage from the previous experiments done on the Cu-Ge system, and prior to metal deposition, we dipped all Ge NWs in a (HI:H_2O) solution and we exposed them to an Ar plasma for 30 sec to remove the native oxide, except for the sample shown in Fig. (7.1.b) where the reaction was initiated at 250°C, only (HI:H_2O) solution was used to remove the native oxide. Similar to the Cu-Ge NW system, the reaction did not occur in all contacted NWs and the reaction was initiated in 7 out of 9 contacted NWs at 280°C. At 330°C the Al intrusion in the Ge initiated in 9 out of 16 contacted NWs and the number of activated NWs raised after increasing the temperature to 380°C and did starts in 11 out of 16 contacted NWs. This latter experiment showed a particular behavior during the 2nd heating at 380°C where the interface was not always as sharp as it was at low temperature in both NWs. We observed that the propagation stopped abruptly in the small NW and two interfaces appeared at the Al/Ge NW interface (this is illustrated in the zoom made on the interface Fig.(7.4) and in Al-Ge (H_b - M_2 - 280°C)). This double interface was more clearly visible in STEM images as shown in Fig.(7.5). In addition, the reaction was not initiated in the

opposite sides of the exchanged segments even after rising the temperature to 380°C, as it can be well observed in the STEM image shown in Fig. (7.5). The influence of

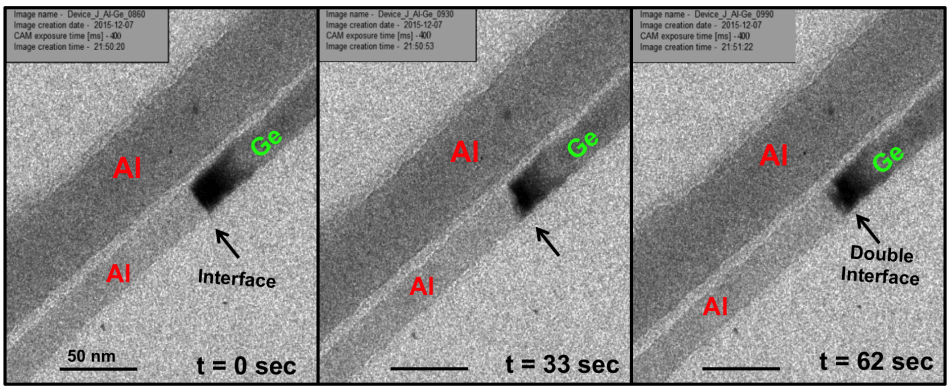

FIGURE 7.4: Different snapshots taken from the video M_3 - H_b - 380°C during the in-situ H_b heating at 380°C where we can observe the appearance of the double interface.

the interface quality on the reaction initiation is manifested also at high temperature as can be clearly seen in Al-Ge (H_b - M_4 - 580°C). In Al-Ge (H_b - M_2 - 400°C), the propagation didn't start in L_{side5} (see Fig. (7.3.a)) until 400°C. In Al-Ge (H_b - M_4 - 580°C), the reaction was activated at 580°C in two contacted NWs, however, a third NW contacted by the same Al strip line didn't show any metal propagation even after increasing the temperature to 800°C. Contrary to the Cu-Ge system, Al did not propagate in crossing NWs at low or high temperatures.

These different formed segments heated using Joule heating techniques were structurally studied in order to investigate the formed heterostructure in the reacted segment at low and high temperature. Therefore, electron diffraction and HRTEM were used to determine both crystallinity and epitaxial relationship of the formed heterostructure at the interface with the Ge NW. EDX analyses using a 3D chemical reconstruction model were performed to provide a reconstruction of the reacted segment cross-section and to determine the proportions of different elements present in the heterostructure.

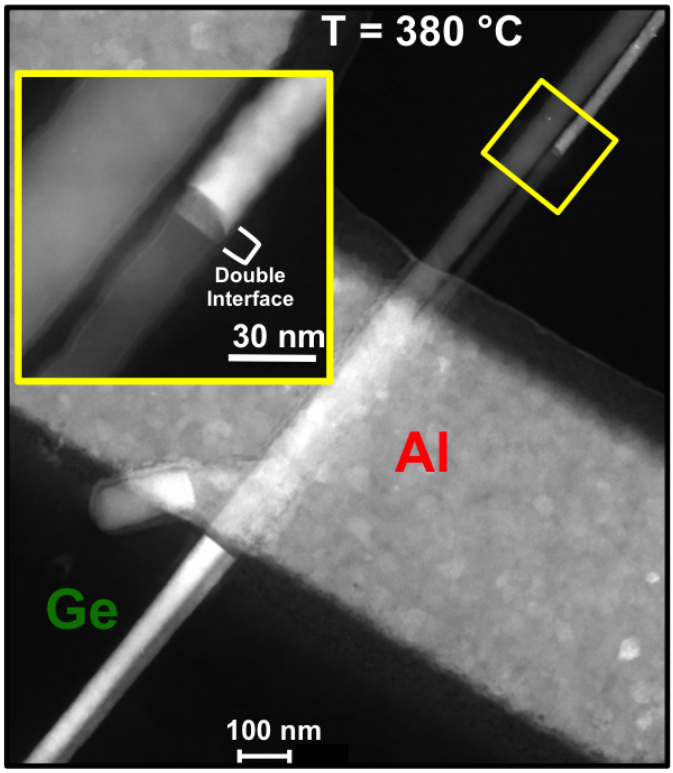

FIGURE 7.5: HAADF-STEM image showing the heated sample using H_b at 380°C where we can see that the Al-Ge exchange occurs only in one side of the contacted NWs. The inset is a STEM image showing clearly the double interface formed during the heating process.

7.3 Structural Analysis of the Al-Ge (NW) System

7.3.1 Electron Diffraction

Fig.(7.6.a) presents a BF image of a heated sample using rapid thermal annealing at 350°C obtained in a CM 300 TEM at 300 kV. The heating was continued until the full exchange of Ge by Al was realized. The yellow circle shows the area where the diffraction pattern in Fig. (7.6.b) was acquired. The electron diffraction shows that the resulting Al NW after heating is mono-crystalline. The diffraction pattern represented in Fig. (7.6.b) can be indexed as Al Face-Centered Cubic (FCC) with a lattice parameter a = 4.05 Å oriented along the [-112] zone axis (ZA).

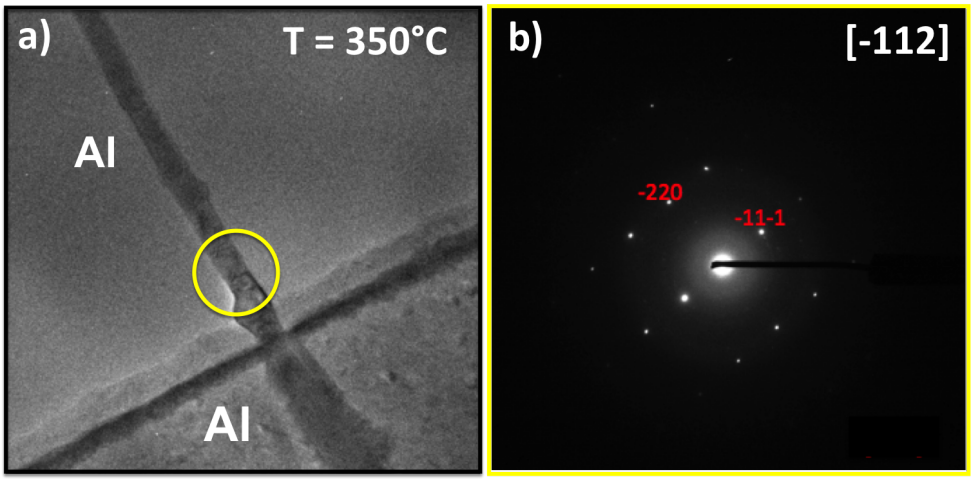

FIGURE 7.6: a) TEM image of a Ge NW completely transformed to Al after being heated in a furnace at 350°C. b) A diffraction pattern on the transformed NW indexed as an FCC Al crystal oriented along the [-112] ZA.

7.3.2 High Resolution Transmission Electron Microscopy

In the following, we present a high resolution TEM image accompanied with preliminary EDX results on two samples from the same batch heated in-situ H_a in an FEI Osiris microscope equipped with four Silicon Drift Detectors working at 120 kV and by rapid thermal annealing (RTA) in forming gas at 350°C for 240 sec. Fig. (7.7) summarizes the results obtained for both types of samples. Fig. (7.7.a) shows a HAADF-STEM image made at the Ge/Al interface. The contrast in HAADF-STEM depends both on the sample thickness and on its composition where the more heavy elements scatter more electrons on the annular detector, giving rise to a brighter contrast. Clearly a strong chemical contrast is present with a high intensity on the unreacted Ge part of the NW and a much lower intensity on the reacted part. Since the NW diameter does not change noticeably over the interface, this strong contrast change indicates the presence of heavy elements on the unreacted side, which would correspond to Ge (Z = 32) and a high Al content (Z = 13) that is a much lighter element on the reacted side. Fig. (7.7.b) shows a high resolution HRTEM micrograph of the respective Ge/Al NW heterojunction.

The interface appears to be very sharp and both partitions of the NW crystalline as atomic planes are visible in the HRTEM image Fig. (7.7.b). The Ge part of the NW was oriented on the [011] direction of observation and the corresponding reciprocal lattice peaks obtained from Fourier transformation (Fig.(7.7.c)) show the ⟨111⟩ growth direction of the Ge NW segment with diamond cubic structure and a lattice constant of 5.66 Å being in good agreement with tabulated values [87]. The Fourier

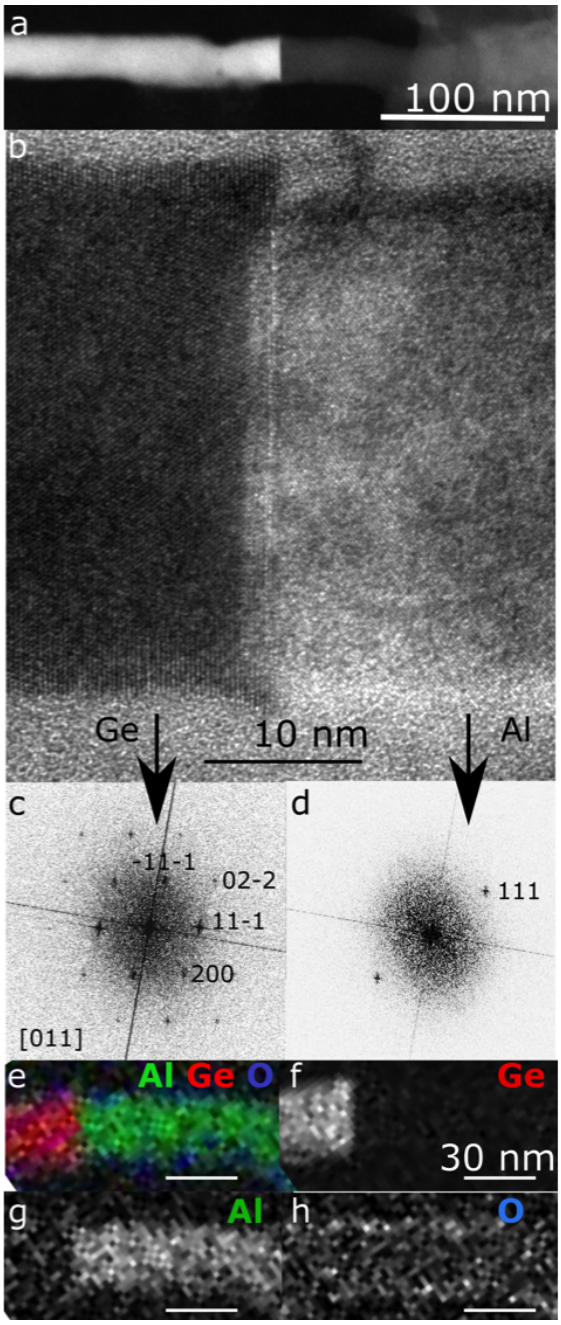

FIGURE 7.7: a) HAADF-STEM image the bright and darker sides corresponds to Ge and Al, respectively. b) HRTEM image of the Ge/Al interface and c) the respective indexed FFT patterns of the Ge and d) Al segments. (e-h) EDX mapping of the Al/Ge interface, presenting e) RGB elemental map of Ge, Al, and O and f) the Ge, g) the Al, and h) the O map, respectively. [14]

transformation in the reacted part shows only one family of planes, with a spacing of 2.34 Å, in good agreement with the theoretical interplanar spacing of 2.34 Å for ⟨111⟩ planes in face centered cubic (fcc) Al. In the HRTEM image (Fig. (7.7,b)) the interface appears to extend over a few atomic planes. This observation could be explained by a projection effect: the Al phase appears to be more advanced into the NW in the

center than on the surface of the NW, and in projection, the top and bottom surface of the NW could give this impression of a less than atomically sharp interface. To confirm the composition of the reacted part, energy dispersive X-ray analysis (EDX) was performed in-situ in the TEM directly after the propagation of the Al phase inside the Ge NW. The EDX maps in Fig. (7.7.e-h) show that the darker part in the HAADF-STEM image (Fig. (7.7.a)) of the NW consists of pure Al and the brighter part is pure Ge. Since the EDX analysis was performed directly after the formation of the heterostructure, no aging effects could occur, potentially modifying the results. The Al/Ge interface appears very sharp and might be atomically abrupt (Fig. (7.7a, b)).

7.4 Chemical Analysis of The Al-Ge System

To confirm these preliminary EDX results, we performed an ex-situ EDX analysis on reacted samples after in-situ TEM heating experiments using both H_a and H_b heating techniques. These analyses were performed in a FEI Osiris at 200 kV using an ultra-Narrow gap Fischione tomography sample holder, which allows a large angle for signal detection contrary to the DENSsolution sample holder where the 6 pins hide an important amount of the X-ray emitted signal (explaining the relatively poor signal to noise ratio in Fig. (7.7 e-h)).

7.4.1 EDX Quantification and Modeling

Fig. (7.8) represents the EDX hypermaps of a heated sample using H_a at $V_{heat} = 0.475V$ with the corresponding 3D cross-section reconstruction using the EDX model defined by Rueda et al [74]. This cross-section reproduces perfectly the experimental concentration profiles extracted directly from the EDX hypermaps. A cross-section of four imbricated hexagons is defined : a thick Al core thickness t = 17.5 nm surrounded by a shell of pure Ge with a thickness estimated ~ 2 nm, surrounded by an Al_2O_3 layer with a thickness estimated ~ 3 nm and covered by a Ge containing Al_2O_3 shell ~ 1 nm. Fig.(7.8) illustrates the distribution of these different layers forming the NW cross-section. The curves in Fig. (7.8) with symbols (--o--, --o--, --o--) are the atomic concentrations of Ge, Al and O respectively deduced directly from the net experimental X-ray intensities of each element using the zeta factor method [73] and the (—, —, —) curves are the calculated concentration profiles using the hexagonal

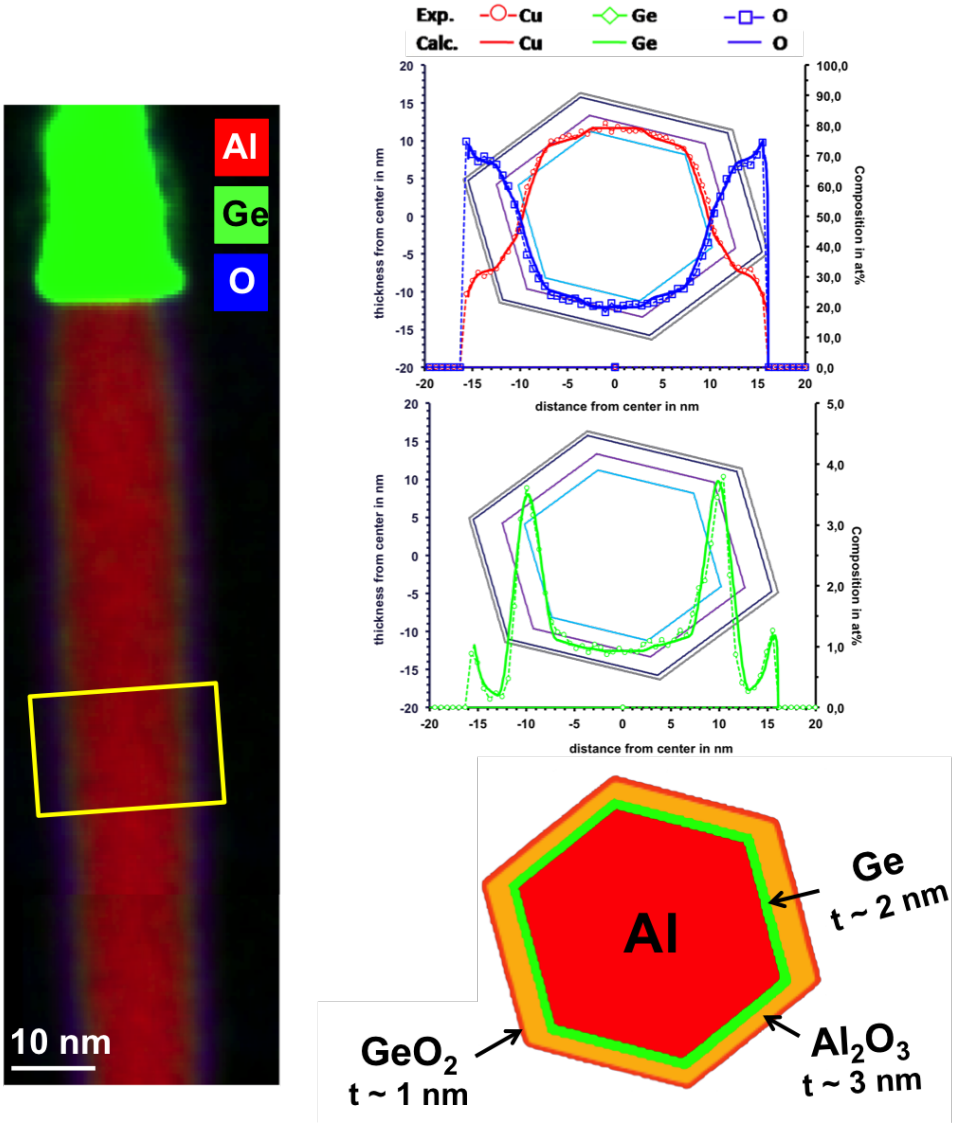

FIGURE 7.8: EDX quantification (line scan & hypermap) of different elements (O, Al, Ge) in the NW after a $H_a(V_{heat} = 0.575V)$ experiment.(left) EDX hypermap on the NW after a H_a heating experiment indicating the different elements (O, Al and Ge). (right) Line profiles obtained along the exchanged, lower, part of the NW. Average concentration (at%) and local thickness profiles along the NW cross-section as well as a schematic representing the NW cross-section using a quantitative 3D chemical reconstruction are shown.

model of the NW cross-section. This analysis confirms the hypothesis that Ge is entirely replaced by Al in the reacted part of the NW creating an Al/Ge heterostructure. The change in the NW diameter along the untransformed Ge segment is due to the beam damage during EDX acquisition.

To investigate the double interface found during the H_b heating experiment at 380°C (see Fig. (7.5)), we performed chemical analysis using EDX in a FEI Themis at 200kV.

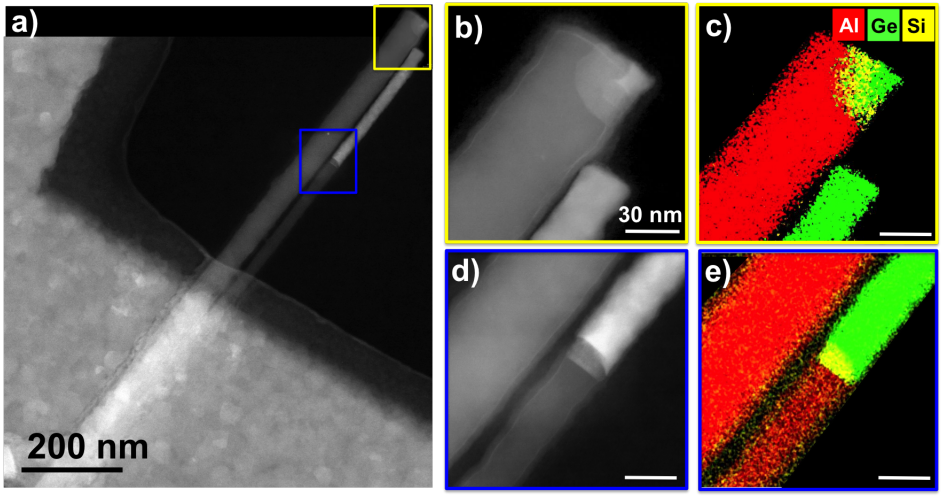

FIGURE 7.9: STEM image and EDX hypermaps at the interface of the formed heterostructure after H_b at 380°C. a) HAADF-STEM image of the contacted NW after the heating experiment. b) and d) HAADF-STEM zoom images of the fully exchanged NW and the double interface formed during the in-situ TEM H_b experiment. c) and e) EDX hypermaps of the corresponding regions where additional to the former detected entities Al and Ge present in the formed heterostructures, Si was found at the Al/Ge interface.

Fig. (7.9) represents HAADF-STEM images and EDX hypermaps taken on the double interface region. A change in the chemical contrast appears in those regions, which indicates a difference in their chemical nature. EDX hypermaps show clearly the presence of a third entity in addition to Ge and Al in the transformed segment. Therefore, a quantification of these presented hypermaps was performed using the Cliff-Lorimer quantification method. The darker segment in the STEM image, similar as observed before, was transformed to an Al core with a Ge shell (t ~ 2 nm), however, an intermediate section of Si_xGe_y appeared at the interface between Al and Ge. A similar observation is made in the thicker NW as shown in Fig. (7.9.b, c), where at the NW extremity an intermediate region with a Si_xGe_y solid solution is observed to separates the Al and Ge parts.

Unfortunately, we couldn't determine the exact composition of the Si_xGe_y solution, due to the presence of Si in the membrane.

As already mentioned above, the propagation was completely stopped after the appearance of these regions separating the Al and Ge sections. Furthermore, the EDX analysis was extended to the Al pads (see Fig. (7.10)), revealing the presence of Ge atoms, most likely formerly constituting the NW. This experiment also shows the favorable incorporation of Ge atoms in the Al pads (see hypermap with the respective EDX spectrum in Fig.(7.10),b).

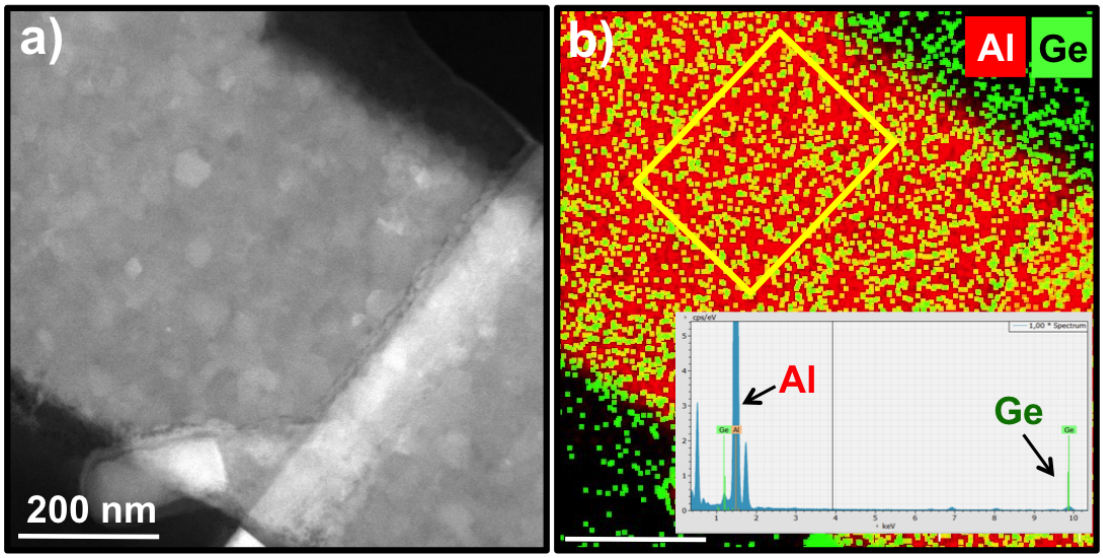

FIGURE 7.10: STEM image and EDX hypermap of Al and Ge elements present in Al metal after phase propagation using H_b heating technique at 380°C. The Ge atoms appeared to dissolved in the Al pad. An EDX spectrum integrated over the boxed region is shown in the inset, demonstrating both Al and Ge x-ray lines.

7.5 Electrical Measurements on the Al/Ge/Al System

As already mentioned, electrical measurements were previously achieved by Kral et al [14] on a Al/Ge/Al NW heterostructures where the exchange occurred at 350°C leaving an untransformed Ge region with a length L_{Ge} = 750 nm. In the following, we will show I-V measurements performed in an Al/Ge/Al NW heterostructure heated using H_a where biasing measurements were preformed in-situ in the TEM. To put these results in perspective, the end of this section also describes electrical measurements done on Al-Ge-Al and pure Al NW structures carried out in the team of Alois Lugstein. Two samples were dedicated for these in-situ TEM heating and biasing experiments in order to achieve Al/Ge/Al NW heterostructures with different unreacted Ge lengths. The sample in Fig. (7.11) is formed based on a Ge NW (L_{Ge} = 3.85 μm) contacted from both sides by Al pads (thickness = 120 nm). We start heating the Side1 and the Al-Ge reaction initiates at V_{heat} = 0.425 V then the heating voltage was increased progressively until V_{heat} = 0.525 V in order to increase the propagation speed. We stopped the propagation after forming an Al segment with a length L = 600 nm. A second heating was started in the opposite side (Side2) and the reaction was initiated as previously (at V_{heat} = 0.475 V). Similar we stopped the heating after forming an Al segment this time with a length (L = 1.46 μm). Unfortunately, the NW damaged after a 3rd heating to decrease the resulting Ge segment length.

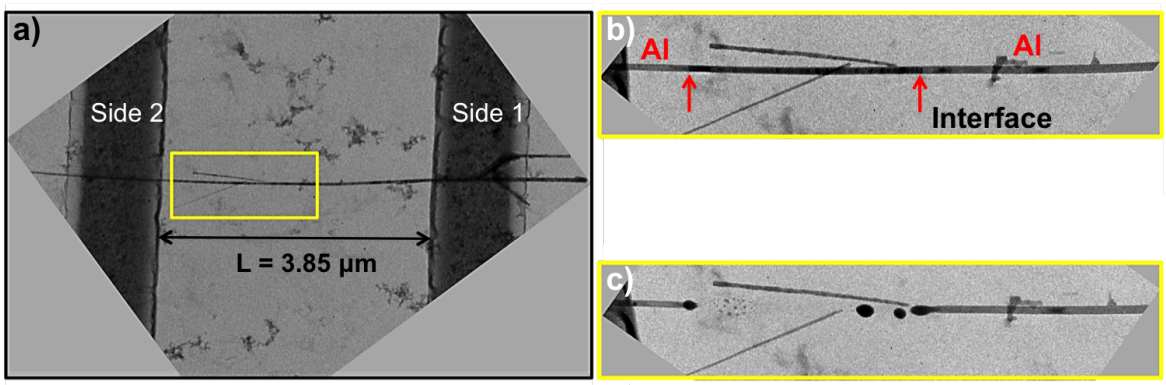

FIGURE 7.11: a) TEM image of a Ge NW contacted from both sides by an Al strip-lines. b) TEM image of the contacted NW after been heated using H_a technique from the both sides at $V_{heat} = 0.425 - 0.525V$ decreasing the length of the Ge segment to L = 1.46 μm. c) TEM image of the contacted NW after been damaged after a 3rd heating to decrease the resulting Ge segment length.

Thus, the second sample shown in Fig. (7.12.a) was heated and the reaction was initiated this time at a low V_{heat} = 0.375 V. The heating was increased progressively until a V_{heat} = 0.525 V and stopped when we reached an unreacted Ge segment of L_{Ge} = 1.32 μm. During this 1st heating (see Fig. (7.12.b)), we observed an Al intrusion in the opposite side where no current was flowing. This observation was limited only to this sample.

A first I-V performed on this formed Al/Ge/Al NW heterostructure revealed a resistance of the remaining Ge on the order of 10 GΩ, however, we didn't include the corresponding plot to the graph in Fig.(7.14) due to the small currents detected. A 2nd heating was started from the opposite side as shown in Fig. (7.12.c) and the propagation started similarly to the previous heating voltage (V_{heat} = 0.375 V). Then the heating was increased progressively until V_{heat} = 0.575 V and stopped at a Ge segment length L_{Ge} = 282 nm. Then, a 2nd I-V was performed and the corresponding data are shown in Fig. (7.14) with ■ where the resistance of the remaining Ge segment (L_{Ge} = 282 nm) decreased to 1.6 GΩ. Previous electrical measurements performed by Kral et al [14] on a similar heterostructure revealed that the Ge segment determines the overall electrical resistance of the Al/Ge/Al NW heterostructure. However, to decrease the Ge segment length below 100 nm scale, we started a 3rd and a 4th heating, flowing current through Strip 1 and later Strip 2, respectively. We succeeded to diminish the Ge unreacted segment to 225 nm and we performed a 3rd I-V measurement represented by ■ in Fig.(7.14), the resistance of the remaining Ge segment (L_{Ge} = 225 nm) decreased to 0.7 GΩ. In order to decrease the unreacted Ge segment below 100 nm, the heating was again started, when suddenly the NW melted as shown in

Fig.(7.13). The observed antisymmetric nonlinear current voltage relationship was

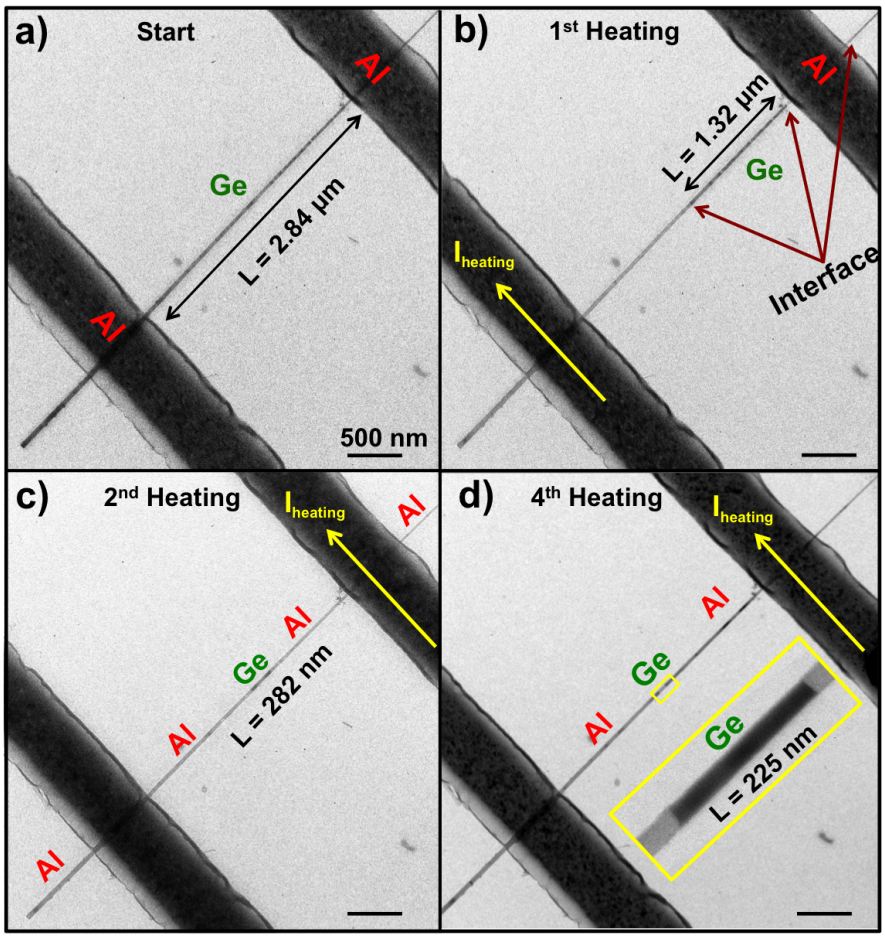

FIGURE 7.12: a) TEM image of a Ge NW contacted from both sides by an Al strip-lines. b) TEM image of the contacted NW after been heated using H_a technique from one side (showed with a yellow arrow) at $V_{heat} = 0.375 - 0.525V$ decreasing the length of the Ge segment to L = 1.32 μm. c) TEM image of the contacted NW after a 2nd heating from the opposite side at the same heating voltage to decrease the Ge segment length to L = 282 nm. d) TEM image of the contacted NW after been heated from both sides to decrease the Ge segment length to L = 225 nm.

observed previously in [14] and explained using two back-to-back Schottky diodes in series with the resistance of the NW, which is a model commonly addressed to explain non-linear I-V curves of semiconductor NW devices [88]. More advanced electrical characterization performed in [14] on Al/Ge/Al NW (with L_{Ge} = 750 nm) showed a Schottky barrier height (SBH) at the Al/Ge interface and determined to be 361 meV, a value calculated assuming a thermionic emission. However, this value is 160 meV above the theoretical value of 200 meV, which is shown in the band diagram in the inset in Fig.(7.14), but is in good agreement with other measurements [89], indicating a strong Fermi level pinning for Ge Schottky contacts around 400 meV [90]. In the experiments in [14], the electrical transfer characteristics of an Al/Ge/Al NW

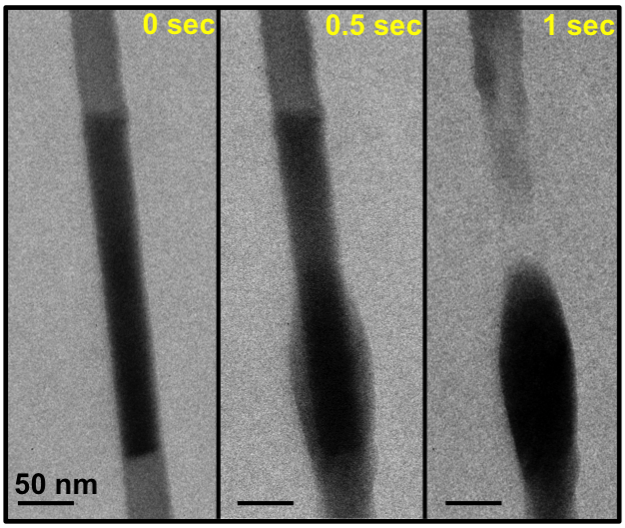

FIGURE 7.13: TEM image of Al and Ge, d_{NW} = 36.5 nm, melted during H_a heating experiment.

(L_{Ge} = 750 nm) FET device is similar to a p-channel transport mode of the transistor. The VLS synthesized NWs were not doped on purpose during growth, but apparently due to surface states and bulk impurities unintentional p-type doping of Ge NWs usually occurs [91, 92].

Furthermore, more than 20 NWs with diameters ranging from 20 to 50 nm fully exchanged to Al after a thermal treatment were electrically studied in [16] using 4-point measurements. They revealed a resistivity $\rho = (131 \pm 27) \times 10^{-9} \Omega.m$ which is approximately five times the resistivity of bulk Al [93]. The high resistivity values found in such nanostructures with dimensions approaching the mean free path of charge carriers are due to surface and grain boundary scattering [94]. In these formed Al NWs grain boundary scattering is excluded due to their monocrystallinity. However, an additional scattering appeared to result from the additional Ge shell [16]. These c-Al NWs revealed to tolerate high current densities $\sim 10^{12} A.m^{-2}$ and remain stable over 15h under this current density. These characteristics make them very interesting to be used for device interconnects.

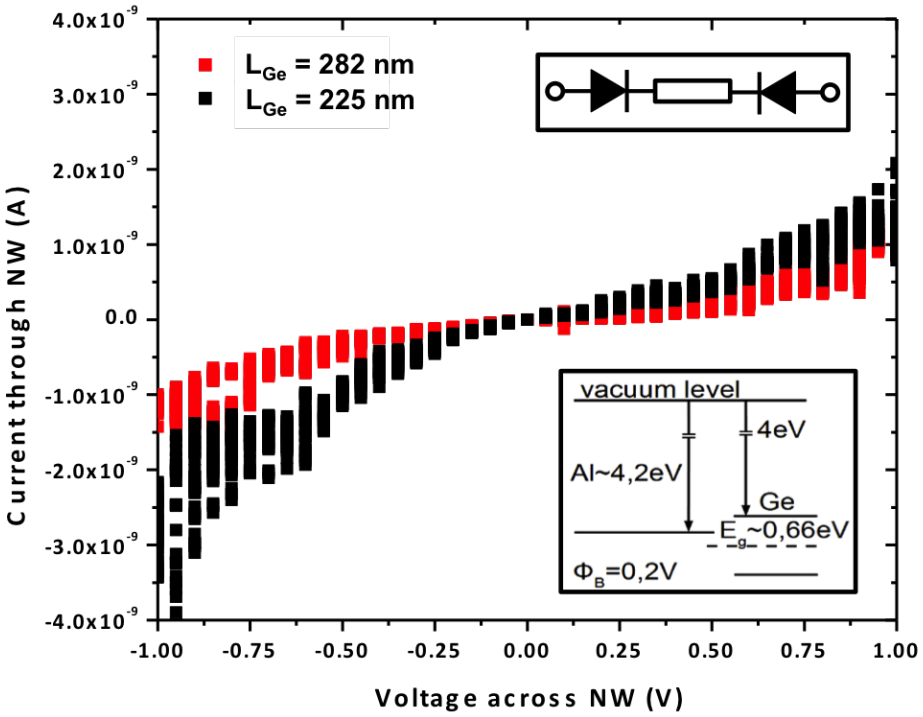

FIGURE 7.14: (a) I-V characteristics of Al/Ge/Al segment with a diameter $d_{Ge} = 37nm$ in a two-point configuration. The red plot correspond to a Ge segment length L = 282 nm and the black plot to a Ge segment length L = 225 nm.

7.6 Discussion and Modeling

In the following, we combine both kinetic and structural analysis results to get a better understanding of the Al intrusion through the Ge NW.

The Al pad/Ge NW interface appeared to influence the reaction initiation and the minimum annealing temperature required for the Al/Ge reaction initiation. As mentioned above, this phenomenon was manifested in two samples due to a change in the instrument used for the Al sputtering deposition. The deposition conditions were found to be similar in both machine. The only difference between the two machines is related to the purity of the crucible (5N and 3N) for deposition. Al-Ge exchange takes place at the lowest temperature in the sample where the deposition was performed in the machine with the crucible 3N. As no propagation is observed for Al deposited by e-beam evaporation, it appears that the energy of the Al particles arriving at the NW is an important parameter. Therefore, we speculate that either the purity of the target influences the reaction initiation, or the energy of Al particles in one machine is higher, either due to a target where Al is more easily extracted (for

sputtering it is known that even nominally identical targets from the same manufacturer can have a different extraction energy) or to features in the sputtering machine architecture that were unknown.

The kinetic data from Fig. (7.1, b,d,f) were fitted using eq.(2.17). Even though it appears that in general thinner NWs show a faster propagation rate (compare NW heated at T = 250°C with the much thicker NW at T = 330°C), this trend does not hold for all observed reactions (see e.g Fig. (7.1.d)) where the fastest propagation is observed for the intermediate NW diameter. However, this NW is highly stressed due to

TABLE 7.1: Summary of different experiments performed on Aluminum-germanium samples using both H_a and H_b heating techniques at low temperature. All the samples show a square root evolution of the reaction interface as a function of time.

Heating	Temperature	Number of NW	Diameter	Curve Behavior	Fit Coefficient (nm/sec $^{0.5}$)
H_b	330 °C	1 NWs	D_1 = 50 nm ; D_2 = 26 nm	square root	B_1 = 17.71 ; B_2 = can't be fit
H_b	250 °C	1 NW	D_1 = 33.5 nm ; D_2 =29.6 nm; D_3 =26.5 nm	square root	B_1 = 118 ; B_2 = 247 ; B_3 = 127
H_a	V_{heat} = 0,575 volt	1 NW	D_1 = 20.5 nm ; D_2 = 15-13 nm	square root	B_1 = 22,45 ; B_2 = 99

the curvature as can be seen in Fig. (7.1.c) and this factor can influence the growth rate of the formed heterostructure. Therefore, we can deduce that the heterostructure growth rate is independent, or at least not only influenced by, the NW diameter. We examine the Al-Ge phase diagram and consider the substantially different diffusion behaviors of Ge in Al and vice versa as already introduced in chapter 2. The binary Ge-Al phase diagram is of the simple eutectic type with no intermetallic phase formation. The melting points of Al and Ge are 660 and 938°C, respectively, and the eutectic point is located at a Ge composition of about 29.5 atom % with solid to liquid transition at 350°C. Al shows a solubility of 0.5 atom % in Ge, while Al can contain up to 1.5 atom % Ge. As listed in Table.(7.2), the diffusion constants for both, Ge and Al in Al at 330°C are considerable, i.e, 10^{12} times larger than in Ge. Thus, when the heating starts to provide enough energy, Ge atoms diffuse into the Al pads by surface diffusion on the formed Al segment, as observed by EDX, and we speculate that Al is supplied by self-diffusion, leading to an exchange of Al and Ge atoms, where Al atoms start to replace Ge atoms in the contacted NW. The Ge atoms continue to diffuse from the interface into to the Al pad, diffusing on the Al segment in a small shell of ~ 2 nm as determined by the EDX analysis. In contrast to the Kirkendall effect [95], which occurs when one element diffuses more quickly than the other and the lattice sites left behind are empty for that particular system, Al is effectively supplied via fast

TABLE 7.2: Activation energy and diffusion coefficients [18, 19] for Ge and Al, and resulting diffusion constant at the annealing temperature of 330°C

	Aluminium	Germanium	Aluminum	Germanium
in	Aluminium	Aluminum	Germanium	Germanium
E_a (kJ/mol)	123.5	121.3	332.8	303
D_0 (cm^2/s)	0.137	0.48	1000	24.8
D (cm^2/s)	$2.71\ 10^{-12}$	$1.47\ 10^{-11}$	$1.43\ 10^{-26}$	$1.36\ 10^{-25}$

self-diffusion and released to the Ge NW for the compensation of the Ge diffusion. All kinetic plots at these different low temperatures evidence a square root behavior (see Fig.(7.1. b,d,f)) and were well fitted using the parabolic growth law using eq.(2.17). This means that the rate limiting step of the reaction propagation is a diffusion process, however surface diffusion does not appear to be the rate limiting step since no obvious influence of NW diameter was observed. According to the model presented in [41], and our presented model in subsection 2.5.7, the growth rate is limited by a volume diffusion, therefore, we used eq.(2.30), to deduce the volume diffusion equation that can be written as :

$$L = \sqrt{Bt} = \sqrt{\frac{C_{res}}{N} 2D^{v}.t} = \sqrt{2D^{v}.t} \tag{7.1}$$

that we applied to the data shown in Table (7.1). We find the volume-diffusion coefficient of Al self-diffusion at different low temperatures summarized in Table (7.3). The diffusion coefficient found at 330 °C is comparable to the bulk Al self-diffusion

TABLE 7.3: Calculated Al self-diffusion coefficients

	Heating	Plasma (sec)	D(cm^2/s)
H_b	T = 330 °C	30	1.56×10^{-12}
H_b	T = 250 °C	—	1.51×10^{-10}

at 330 °C presented in Table.(7.2). The reaction appears therefore limited by Al self-diffusion. Ge surface diffusion also occurs but doesn't appear to influence the reaction rate. The diffusion coefficient at 250 °C that is a characteristic of the Al diffusion through the NW, is much higher compared to the Al self-diffusion from literature. We speculate that this high value is due to the NW curvature or to a size factor that starts to be significant at diameters < 40 nm.

From our observations, and what was reported in literature [24, 25, 41, 59], we speculate that the rate limiting step at high temperature, where stepwise growth was observed, is nucleation at the Al-Ge interface, as in this growth mode enormous material quantities are exchanged almost instantly and the other possible rate limiting steps (Al reservoir - Al NW interface or diffusion along the Al NW segment) appear even more unrealistic or are kinetically excluded. From Table (7.1), and similar to what was presented in chapter 6 for the Cu-Ge system, a better control of the Al propagation is provided by H_a with respect to H_b heating techniques, as lower propagation speeds were observed. As mentioned in the previous chapter, H_a experiments are not temperature calibrated. We expect that the temperature is systematically lower in H_a experiments.

It was demonstrated in [14] that, in accordance with the phase diagram, Ge substitution at the reaction interface continues as long as the concentration of Ge in the Al reservoir is below the solubility limit. They used very small Al pads ($1\times1\mu m^2$ with a thickness of 100 nm and observed that the exchange reaction, i.e. Ge replacement, comes to a standstill when the Ge concentration in Al surpasses the 1.5 atom % limit, regardless of further annealing. Accordingly, extended Al pads of several 100 × 100 μm^2 represent a huge reservoir for Ge, and the reaction is prolonged as long as the process temperature is high enough. Thus, by patterning adequate Al pads on both sides of the Ge NW we even accomplished full exchange of the Ge resulting in a pure Al NW, keeping the geometry of the former Ge NW. Such fully exchanged NWs appear to be single crystalline Al in the HRTEM micrographs taken near the Ge/Al NW interface, and energy dispersive TEM-EDX measurements revealed that they are free of Ge in the Al core in the detection limit of typically 0.5 atom %.

It should be noted that the exchange reaction also took place when the whole structure was covered by Al_2O_3, indicating that even with a shell on the Ge NW, Ge can still diffuse at the interface of Ge and Al_2O_3.

Remarkably, in the remaining Ge NW segment no Al contamination can be detected due to the extremely low diffusion coefficient of Al in Ge.

7.7 Outlook: Electrical potential of Al/Ge heterostructures

Furthermore, the electrical properties of Al/Ge/Al NW heterostructures showed very interesting characteristics for eventual applications as FETs. In [96] negative differential resistance (NDR) at room temperature was demonstrated in more than ten Al/Ge/Al NW heterostructures integrated in back-gated FETs. NDR was rarely ob-

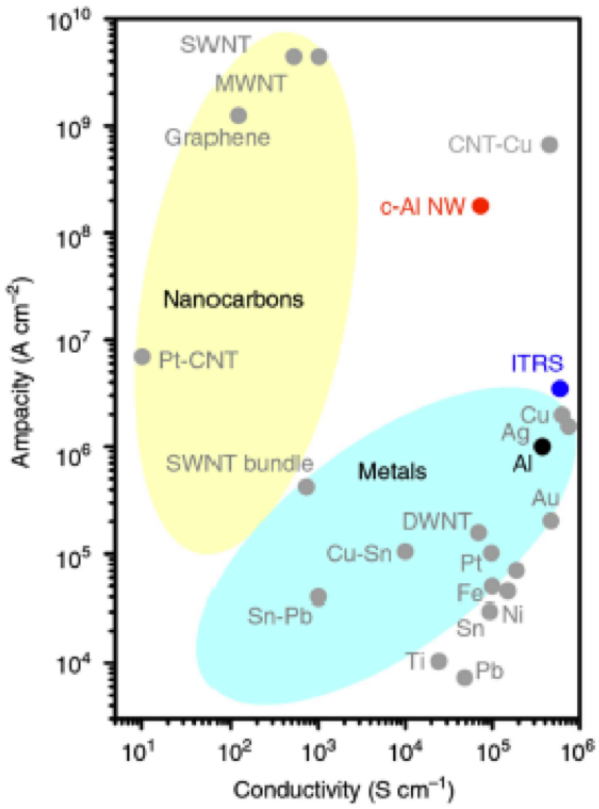

FIGURE 7.15: Comparison of failure current density (ampacity) and conductivity of common metals, nanocarbons, carbon nanotube-copper composites and c-Al NWs. Both carbon nanotube-copper composites and c-Al NWs clearly exceed the ampacity recom- mended for conductors by the ITRS. Figure adapted with permission from Subramaniam et al [15] copyright 2013. [16]

served at room temperature except for the Gunn effect in GaAs. This nonlinear electron transport phenomenon may enable fast switching logic circuits, static memory cells or high-frequency oscillators.

The Al/Ge/Al NW heterostructures present an additional application as can be deduced from the experiments shown in Fig. (7.9) where the Al appeared to pile up the Si atoms present in the NW (seen clearly in Al-Ge (M_3 - H_b - 330°C)) probably due to a contamination from the Si substrate or the germane gas precursor used for

the VLS process. Therefore, this heterostructure could be potentially used to pile up dopants (Phosphorous (P) or Boron (B) atoms) at the Al/Ge NW interface in order to improve their electrical quality, or create novel Al/SiGe/Al NW heterostructures. For example B shows, according to the Al-B phase diagram [97], a low solubility (0.055 atom% of B) in Al at temperatures under 650°C and the only intermetallic structures that appeared to form start from ~ 67 atom% of B. In addition, Si atoms at a certain % appeared to be a barrier for the Al propagation in a Ge NW.
The Al nanowire formed by the presented approach allows to fabricate single-crystal Al NWs with well controlled geometries. As was mentioned above from the electrical measurements performed by Brunbauer et al [16], c-Al NWs appeared to sustain high current densities where the failure current values detected during the different experiments are comparable to Au NWs. This remarkable high failure current density of c-Al NWs exceeds the level recommended by the International Technology Road-map for Semiconductors (ITRS) [15, 98] by orders of magnitude as represented in Fig.(7.15). Therefore, c-Al NWs can be defined as an attractive candidate for interconnects or high-performance electrodes in future device applications. Furthermore, superconductivity of the c-Al NWs was investigated in [16] by performing temperature dependent I-V measurements in an adiabatic demagnetization refrigerator (ADR). Thus, a transition to a superconducting state was found for a c-Al NW with a length of 2.95 μm and a diameter of 33 nm. A transition to the superconducting state was found to occur at a critical temperature of T_c = 1.46 K which is significantly higher than for Al bulk ($T_{c,bulk}$ = 1.19 K) [99]. This high T_c value depends both on NW size effects where the T_c increases for thinner Al NWs [100] and to the presence of impurities, the Ge dissolved in the shell around the Al NW (detected by EDX analysis).

7.8 Conclusion

In summary, this section presents a detailed TEM in-situ study of the formation of metal-semiconductor NW heterostructures via direct Joule heating [H_a] and controlled temperature [H_b] heating experiments, where [H_a] shows a better control of the reaction interface propagation speed. A distinct asymmetry in the diffusion behavior of Al and Ge enables the formation of metal/semiconductor NW heterostructures via thermal annealing. The kinetic results at low temperature revealed that the Al/Ge NW propagation is governed by the Al self-diffusion in the Al volume and the

Al pad/Ge NW interface seems to be a critical factor on the exchange reaction initiation. Ge diffuses through a surface channel to the Al reservoir, as observed by EDX, and does not noticeably influence the propagation rate. The formation of single crystalline Al NWs via these both thermal annealing techniques was confirmed by quantitative EDX analysis, revealing a double core-shell structure, with an Al core covered by a thin layer of Ge with an estimated thickness of 2 ± 0.2 nm, covered by an Al_2O_3 layer with another region of low Ge concentration at its surface with a thickness around 1 nm. The Al exchange with the Ge NW under heating appeared to take place in multiple nucleation sites underneath the Al pads.
Electrical measurements performed in Kral et al [14] and our experiments, revealed a decrease of the Ge NW resistance by decreasing the scale of Ge segment in the Al/Ge/Al NW heterostructure.

Direct Joule heating experiments appear to be a powerful tool to develop and control short channel metal oxide semiconductor transistors down to sub-10 nm length scales, independent of the spatial resolution of an lithography process.

Chapter 8

Conclusion

The goal of this thesis is to provide a better understanding of metal incorporation in semiconducting NWs by performing in-situ heating experiments in a Transmission electron microscope with the aim to achieve Ohmic, low resistivity contacts at the metal/semiconductor interface, with the ultimate aim to achieve a Field Effect Transistor (FET).

We performed in-situ heating experiments in a TEM to provide nm scale spatial resolution in order to follow all the phenomena that occur during a solid state reaction between a metal and a semiconducting nanowire (NW). A better understanding of the different phenomena occurring during the metal-semiconductor solid-state reaction and correlation of their electrical properties to their structural characteristics can allow improved device fabrication and performance.

We have studied two different metal-semiconductor NW couples : Cu-Ge and Al-Ge, due to the interesting electrical properties of their respective intermetallics in bulk, thin films and NWs systems. We also initiated a study on the Pt-Si system, however preliminary results were not promising, therefore this topic was abandoned.

To provide a better electrical contact between metal and semiconductor, we thermally activate a solid-state reaction using two different heating techniques:

1. A *direct* Joule heating technique, (H_a), initially demonstrated by Mongillo et al [75] from Silvano de Franceschi's group, where a current is passed through a metal stripline positioned over the NW extremity, leading to a very local heating. We have extended the use of this technique to structures fabricated on thin nitride membranes, allowing observation in the TEM.

2. A membrane-substrate Joule heating technique (H_b) where a current is passed through a buried Mo heating spiral in a Si_3N_4 membrane, leading to an uniform heat distribution in the entire sample. We have used commercial heater-chips from DENSsolutions, and fabricated contacted NWs on these chips.

For both material couples we have performed in-situ heating experiments in the TEM at low acceleration voltage to avoid an influence of the electron beam on the reaction. We have studied the reaction kinetics by following the location of the reaction interface during constant heating as a function of time. We found that using the H_a heating technique, due to the very local heating, a temperature gradient was present along the Ge NW, which was confirmed by finite element heat flow calculations.

Therefore, we have used the H_b heating technique to obtain kinetic data at constant temperature, which allows their interpretation. We have used different TEM-based characterization techniques (nano-beam diffraction (NBED), electron diffraction tomography (EDT) and energy dispersive x-ray analysis (EDX)) to study the structural and chemical properties of the obtained NW heterostructures. We have used diffusion models from literature to interpret the kinetic data, in combination with the structural and compositional results, to understand how these reactions proceed, and which rate limiting step influence the reaction interface propagation.

Below we present the conclusions obtained for each separate system.

8.1 The Cu-Ge system

In the Cu-Ge system we observed that kinetic results on the low temperature H_b heated samples were similar to the H_a samples (for short propagation distances). At low temperature, we expressed the location of the reaction interface as a function of time, and found these data are well fitted by a square root function. At high temperature H_b experiments, the kinetic data were described by a linear relation with time. The structural studies showed that at low temperature an orthorhombic Cu_3Ge phase, and at high temperature the hexagonal compact Cu_5Ge structure were formed, respectively. EDX analyses in combination with 3D model fitting demonstrated that around the Cu_3Ge core different shells were present being a shell of pure Cu, pure Ge and GeO_2, respectively. In addition, the protruded crystals during the

Cu-Ge NW solid-state reaction tend to comfort the Cu surface diffusion rate limiting step. They indicate the presence of a high Cu concentration at the NW surface. Thus, the Cu atoms at the surface start to react simultaneously with the Ge atoms at the surface and at the core of the Ge NW resulting on Cu_3Ge phase formation both in the protruded crystals and the NW core. However, these protruding crystals can be avoided by applying enough strain on the NW surface as was observed during an in-situ TEM H_a experiment. In this latter, a shell appeared to surround the NW (formed unintentionally) resulting after reaction to an absence of any protruded Cu_3Ge crystal on the surface of the transformed segment. Furthermore, we observed by EDX that Ge is diffusing into the grain boundaries in the Cu metal reservoir. Combining all these different observations at low temperature, the most likely hypothesis to explain the Cu-Ge NW solid state reaction is that the rate limiting step is Cu surface diffusion, and the reaction proceeds by both surface diffusion of Cu from the reservoir to the reaction interface, as well as surface diffusion of Ge from the reaction interface into the grain boundaries in the Cu reservoir, where Ge piles up on the germanide surface next to the contact metal, before entering the metal stripline. At high temperature the rate limiting step is the metal-NW interface. We observed that the reaction was never initiated in all contacted NWs. Changing the preparation protocol increases the yield of NWs were the reaction initiated, however, still some NWs remained where no reaction was observed, indicating that the quality of the metal-NW interface is both very important for reliable reaction initiation, as well as difficult to control perfectly. We find that using H_a experiments lower reaction speeds can be obtained with respect to the H_b experiments. As H_a experiments are not temperature calibrated, this seems to indicate that they occur at lower temperature. It appears therefore that the current present in the metal stripline on the NW in H_a experiments decreases the reaction initiation temperature, and propagation at lower temperature is possible than in H_b experiments.

8.2 The Al-Ge system

In the Al-Ge system we observed that kinetic results on the low temperature H_b heated samples were similar to the H_a samples, similar as observed in the latter. We expressed the location of the reaction interface as a function of time, and found these data are well fitted by a square root function at low temperature. At high temperature

H_b experiments, the kinetic data were described by a stepwise growth, where the interface would move very fast during a short time period, and remains static during other time periods. Interestingly, these steps were tens of nms in size. The structural studies showed that a crystalline pure Al NW was formed. EDX analyses in combination with 3D model fitting confirmed these results and demonstrated that around the Al core different shells were present being a shell of pure Ge, Al_2O_3 and a combination of Al_2O_3 and GeO_2, respectively. Furthermore, we observed by EDX that Ge is diffusing into the Al metal reservoir. Combining all these different observations at low temperature, the most likely hypothesis to explain the Al-Ge NW solid state reaction is that the rate limiting step is Al volume self-diffusion, and the reaction proceeds by both volume diffusion of Al from the reservoir to the reaction interface, as well as surface diffusion of Ge from the reaction interface into the Al reservoir. In addition, this explanation can be confirmed when comparing the resulted transformed segments in Al-Ge to the Cu-Ge segment after the solid-state reaction. If we observe all the different images presented in chapter 7 the diameter of the transformed segment remain almost unchanged also no protruded crystals were observed in the Al formed segment. Thus, the presence of both Al and Ge in the NW surface can be surely excluded. Whereas, the presence of Ge in the NW surface is certain (EDX analysis). According to the extended Deal and Grove model [57], a L-curve independent of the NW radius indicates a volume diffusion. So, the only explanation that could hold and combine all these observations is : when the Ge surface diffusion starts to occurs leaving an empty sites the Al supply is assured by a volume self-diffusion.
We speculate that at high temperature the rate limiting step is the reaction interface in the NW. We observed that the reaction was never initiated in all contacted NWs. Changing the preparation protocol increases the yield of NWs were the reaction initiated, however, still some NWs remained where no reaction was observed, indicating that the quality of the metal-NW interface is both very important for reliable reaction initiation, as well as difficult to control perfectly, similar to the Cu-Ge NW system. We find that using H_a experiments lower reaction speeds can be obtained with respect to the H_b experiments.
Unfortunately, we couldn't go further in the crystalline orientation of the Ge NW after been transformed to an Al NW and in the Al/Ge interface due to the beam damage that occurs in all these NWs after a long exposure time.

8.3 Outlook

Results presented in the previous samples are important to optimize the design of NW based devices. In particular, the H_a heating technique appears to give very precise control over the remaining Ge segment length, and is therefore a potentially powerful tool to fabricate highly controlled short channel FET devices, where the size of the channel does not depend on the resolution of a lithography technique. Unfortunately, preliminary results on fabricating in-situ a sub 100 nm Ge segment were not promising: the NW device was destroyed for sizes below 200 nm. Currently we are not sure if this is an intrinsic limitation of the H_a experiments, or due to current instabilities, electric discharge problems, grounding problems, or other issues related to the electrical setup.

For future studies, we should aim to improve the reliable preparation of the NW-metal interface, to avoid different reaction initiation temperatures for different NWs on the same sample. Furthermore, we need to investigate if the H_a heating method is really capable of forming these short channel devices, or indeed limited by other factors.

In future experiments we aim to focus more on the electrical properties of these samples, looking at the influence of dopants or low Si concentrations in the NWs to fabricate more complicated heterostructures.

Chapter 9

Résumé en Français

Dans ce dernier chapitre de thèse, l'ensemble des chapitres seront résumés en français. Cet exercise est indispensable en France pour tout doctorant rédigeant son manuscrit de thèse en anglais.

Le choix de travailler avec des nanofils de Si et Ge dans le cadre de cette thèse est dû au fait que l'industrie de silicium appliqué à la microélectronique est l'activité numéro un développée dans la région Grenobloise. Les nanofils de Si apparaissent comme une évolution logique dans la technologie électronique qui a pour but de miniaturiser la taille des transistors constituant les circuits intégrés augmentant ainsi leur rendement (Loi de Moore). Dans notre étude, on s'est également intéressé aux nanofils de Ge dont la mobilité des porteurs de charges assez élevée comparée au Si. Bien que l'inconvénient majeur du Ge est l'instabilité de son oxide, dernièrement l'interêt pour ce matériau revient en avant de scène pour être combiné avec le Si formant l'alliage SiGe dans les matériaux 2D et dans des nanofils SiGe coeur(Ge)-coquille(Si).

Le sujet de cette thèse a été proposé dans le but de réaliser des dispositifs à base de nanofils semi-conducteur présentant diverses applications dans nombreux domaines d'étude (électronique, spintroniques,...) in-situ dans un microscope électronique en transmission (MET). Le choix de réaliser ces expériences in-situ dans un MET a pour but de travailler avec une haute résolution spatiale qui permet de suivre l'ensemble des phénomènes qui se produisent durant la réaction entre le métal et

le Ge activé sous chauffage. De plus, réaliser des expériences à des résolutions spatiales de l'ordre du nanomètre permet de contrôler au mieux la propagation de la phase formée après réaction entre le métal et le nanofil de Ge au sein de ce dernier permettant de réduire la taille du segment de Ge à des tailles inférieures à 100 nm, formant des dispositifs pouvant être utilisés en nano-électronique (ex: comme transistors à effet de champ).

9.1 Plan Du Manuscrit

Le **premier chapitre** contextualise le travail de thèse incluant l'ensemble des raisons rappelées brièvement ci-dessus, qui nous ont motivés à travailler sur ce sujet (réactions à l'état solide entre un métal et un nanofil semi-conducteur).

Dans le **deuxième chapitre**, nous rappelons l'interêt et l'influence de la formation d'hétérostructures sur l'arrangement des bandes électroniques dans un contact entre un métal et un semi-conducteur. Nous répertorions l'ensemble des hétérostructures rapportées dans la littérature qui se forment lors de la réaction à l'état solide entre un métal et du Si et du Ge, en se focalisant sur les phases rapportées permettant d'améliorer la qualité du contacte électrique entre le métal et le semi-conducteur. Parmi l'ensemble des matériaux historiquement utilisés en bulk et couche mince, ainsi que ceux récemment utilisés, nous nous sommes focalisés sur trois métaux : Cu, Pt et Al utilisés comme contact avec des nanofils de Si et de Ge.
Des résultats préliminaires obtenus sur le système Pt-Si sont présentés et comparés avec des résultats déjà publiés dans la littérature sur le même système. Les résultats préliminaires obtenus sur Pt-Si n?étant pas encourageants, nous avons cessés l?étude de ce couple de matériaux.
La fin du chapitre présente l'ensemble des modèles de diffusion qui permettent d'expliquer la cinétique de la formation des différentes hétérostructures lors de la réaction entre les différents métaux utilisés et un nanofils semi-conducteurs.

Le **troisième chapitre** décrit le procédé de fabrication qui nous permet de réaliser les échantillons étudiés. Dans un premier temps, on rappelle la technique utilisée pour l'élaboration des nanofils de Si ou Ge. Nous décrivons ensuite en détails le protocol

suivis pour réaliser les échantillons étudiés in-situ au MET. Les différentes échantillons ont été élaborés en salle blanche en utilisant les techniques conventionnelles de lithographie. Des membranes de nitrures de silicium Si_3N_4 transparentes aux électrons ont été fabriquées dans le but de déposer des nanofils de Si ou Ge. Ces nanofils sont contactés individuellement des deux côtés par un métal (Cu, Pt ou Al), lui-même connecté électriquement à un dispositif externes par l'intermédiaire d'un porte-objet MET électrique.

Nous présentons dans le **quatrième chapitre** les différents instruments et techniques de la microscopie électronique en transmission utilisés lors de l'analyse des hétérostructures formées après réaction. L'objectif est de rappeler brièvement les caractéristiques des différentes techniques utilisées en microscopie électronique en transmission qui ont permis de collecter suffisamment d'information pour expliquer les différents phénomènes qui se déroulant lors de la formation des différentes hétérostructures. Nous présentons un model EDX permettant de reconstruire en 3D la partie transformée du nanofil en modélisant à la fois sa structure et sa composition.

Le **chapitre cinq**, on présente l'équipement électrique ainsi que le porte-objet utilisé pour pouvoir réaliser un chauffage par effet Joule in-situ dans un MET. Nous discutons brièvement du porte-objet MET ainsi que des différents équipement électrique permettant d'effectuer les deux types de chauffage à effet Joule H_a et H_b. La technique de chauffage intitulé H_a consiste à faire circuler un courant électrique le long du métal en contact directe avec le nanofil semi-conducteur permettant ainsi de réaliser un chauffage local au niveau du contact. A l'extrémité du contact métallique une différence de potentielle est appliquée avec une configuration bien particulière : un potentiel négatif d?un côté et positif de l?autre. Ceci permet d'annuler le potentiel électrique au point de contact entre le métal et le nanofil empêchant toute circulation du courant le long du nanofil. La deuxième technique de chauffage appelée H_b, consiste à faire circuler un courant électrique à travers une spirale de Pt ou Mo enterrée dans une membrane de nitrure de silicium permettant une distribution de chaleur homogène au niveau d'une large surface de la membrane. Ces dernières contrairement aux membranes utilisées dans le chauffage H_a sont calibrées en temperature, fabriquées et commercialisées par une entreprise néerlandaise DENSsolution. Nous présentons le montage dans chaque types de chauffage et comment et

reliés l'équipement électriques externe à l'échantillon au MET.

Le **sixième chapitre** regroupe l'ensemble des données expérimentales récoltées durant des expériences réalisées in-situ dans un MET sur le système Cu-Ge en utilisant les deux méthodes de chauffages par effet Joule H_a et H_b (décrites dans le **chapitre cinq**). Une étude cinétique et structurale a été réalisée afin de pouvoir expliquer le mécanisme de réaction et les phases résultantes après chauffage en utilisant les deux techniques. L'étude cinétique été réalisée en suivant l'évolution du front de la phase formée en fonction du temps et les différentes résultats obtenus sont expliqués par le modèle de diffusion présenté dans le **chapitre 2**. Les analyses structurales de la partie transformée du nanofil ont été réalisées par diffraction électronique et par analyse dispersive en énergie au rayon-X (EDX). Grâce à un modèle EDX, nous avons pu reconstruire chimiquement en 3D une coupe transversale de la partie transformée du nanofil. Les différentes reconstructions révèlent que les parties transformées du nanofil sont formées d'une double coeur-coquille, le coeur du nanofil est formé principalement de la phase Cu_3Ge, entouré de couches très fines de Cu (1 nm), Ge (0.35 nm) et GeO_2 (4.5 nm) respectivement. Ces observations expérimentaux révèlent une diffusion en surface qui se produit durant l'échange formant l'hétérostructure résultante. Durant l'ensemble la formation de ces hétérostructures dans le nanofil des cristaux poussent le long de la partie transformée. L'apparition de ces cristaux n'influencent pas l'évolution de la phase formée au sein du nanofil et peuvent être éliminés en entourant le nanofil de Ge avant réaction par une couche externe suffisamment épaisse. En combinant l'ensemble de ces résultats et en se basant sur le modèle de diffusion déjà présentés, nous proposons un mécanisme expliquant la formation des différentes hétérostructures présentes dans le nanofils après réaction à basse et haute température.

Finalement, le **chapitre sept**, on présente les résultats obtenus sur le troisième système à base de nanofil de Ge. Nous avons pu y suivre l'évolution in-situ dans un MET la réaction à l'état solide entre l'Al et le Ge en appliquant les deux techniques de chauffage H_a et H_b. Nous étudions l'évolution de la phase formée en fonction du temps et proposons d'expliquer l'ensemble des observations par le modèle de diffusion déjà présenté. Des analyses de diffraction électronique et d'imagerie à haute résolution (HRMET) montrent un échange complet entre le Ge présent dans le nanofil et l'Al dans le contacte métallique après chauffage par H_a ou H_b, formant un nanofil

d'Al après long chauffage. L'application du modèle EDX après caractérisation révèle la transformation du nanofil de Ge en coeur-coquille avec un coeur pure Al et une couche très fine qui l'entoure de Ge (~ 2 nm). En combinant l'ensemble de ces résultats et en se basant sur le modèle de diffusion présenté dans le **chapitre 2**, nous proposons un mécanisme démontrant l'échange qui se produit dans le nanofil après chauffage à basse et haute température. Enfin, nous présentons les différents résultats électriques très prometteurs obtenues sur ce système d'Al-Ge rapportés dans [14, 16].

Bibliography

[1] F. Leonard and A. A. Talin. Electrical contacts to one- and two-dimensional nanomaterials. *Nat Nano*, 6(12):773–783, 12 2011. URL http://dx.doi.org/10.1038/nnano.2011.196.

[2] R. W. Olesinski and G. J. Abbaschian. The Cu-Ge (Copper-Germanium) system. *Bulletin of Alloy Phase Diagrams*, 7(1):28–35, 1986. doi: 10.1007/BF02874979. URL http://dx.doi.org/10.1007/BF02874979.

[3] L. Krusin-Elbaum and M. O. Aboelfotoh. Unusually low resistivity of copper germanide thin films formed at low temperatures. *Applied Physics Letters*, 58(12):(1341–1343), 1991. doi: http://dx.doi.org/10.1063/1.104304. URL http://scitation.aip.org/content/aip/journal/apl/58/12/10.1063/1.104304.

[4] A. J. McAlister and J. L. Murray. The Al-Ge (Aluminum-Germanium) system. *Bulletin of Alloy Phase Diagrams*, 5(4):341–347, 1984. doi: 10.1007/BF02872948. URL http://dx.doi.org/10.1007/BF02872948.

[5] L. E Tanner and H. Okamoto. The Pt-Si (Platinum-Silicon) system. *Journal of Phase Equilibria*, 12(5):571–574, 1991. doi: 10.1007/BF02645072. URL http://dx.doi.org/10.1007/BF02645072.

[6] H. Ryll, M. Simson, M. Den Hertog, R. Dunin-Borkowski, K. El Hajraoui, R. Hartmann, M. Huth, S. Ihle, V. Migunov, J. Schmidt, H. Soltau, and L. Strider. Imaging at the timescale of micro- and milliseconds with the pnCCD (S)TEM camera. *Microscopy and Microanalysis*, 21:1585–1586, August 2015. doi: 10.1017/S1431927615008703.

[7] C. Hollauer. *Modeling of Thermal Oxidation and Stress Effects*. PhD thesis, eingereicht an der Technischen Universität Wien Fakultät für Elektrotechnik

und Informationstechnik, 2007. URL http://www.iue.tuwien.ac.at/phd/hollauer/node16.html.

[8] http://heterna.ief.u-psud.fr/?page-id=380, February 2012. URL http://heterna.ief.u-psud.fr/?page_id=380.

[9] URL http://www.ammrf.org.au/myscope/analysis/introduction/.

[10] http://microanalyst.mikroanalytik.de/info1.phtml. URL http://microanalyst.mikroanalytik.de/info1.phtml.

[11] N. Petkov. In situ real-time TEM reveals growth, transformation and function in one-dimensional nanoscale materials: From a nanotechnology perspective. *ISRN Nanotechnology*, 2013:21, 2013. URL http://dx.doi.org/10.1155/2013/893060%]893060.

[12] http://denssolutions.com/products/heating/, 2015. URL http://denssolutions.com/products/heating/.

[13] http://protochips.com/products/fusion/, 2016. URL http://protochips.com/products/fusion/.

[14] S. Kral, C. Zeiner, M. Stöger-Pollach, E. Bertagnolli, M. I. den Hertog, M. Lopez-Haro, E. Robin, K. El Hajraoui, and A. Lugstein. Abrupt Schottky junctions in Al/Ge nanowire heterostructures. *Nano Letters*, 15(7):4783–4787, 07 2015. doi: 10.1021/acs.nanolett.5b01748. URL http://dx.doi.org/10.1021/acs.nanolett.5b01748.

[15] C. Subramaniam, T. Yamada, K. Kobashi, A. Sekiguchi, D. N. Futaba, M. Yumura, and K. Hata. One hundred fold increase in current carrying capacity in a carbon nanotube-copper composite. *Nature communications*, 4, 2013.

[16] F. M. Brunbauer, E. Bertagnolli, J. Majer, and A. Lugstein. Electrical transport properties of single-crystal Al nanowires. *Nanotechnology*, 27(38):385704, 2016. URL http://stacks.iop.org/0957-4484/27/i=38/a=385704.

[17] Prof. K. Saraswat. Polycides, salicides and metals gates. *Department of Electrical Engineering Stanford University*, 2010.

[18] D. L. Beke, editor. *Landolt-Bronstein : Group III Condensed Matter*, volume 33A. Springer: Berlin Heidelberg, 1998.

[19] Terry C. Totemeier William F. Gale, editor. *Smithells Metals Reference Book*. Elsevier Science : Dordrecht, The Netherlands, 2003.

[20] M. Mongillo, P. Spathis, G. Katsaros, P. Gentile, M. Sanquer, and S. De Franceschi. Joule-assisted silicidation for short-channel silicon nanowire devices. *ACS Nano*, 5(9):7117–7123, 09 2011. doi: 10.1021/nn202524j. URL http://dx.doi.org/10.1021/nn202524j.

[21] Y. C. Chou, W. W. Wu, B. Y. Cheng, S. L.and Yoo, N. Myung, L. J. Chen, and K. N. Tu. In-situ TEM observation of repeating events of nucleation in epitaxial growth of nano $CoSi_2$ in nanowires of Si. *Nano Letters*, 8(8):2194–2199, 08 2008. doi: 10.1021/nl080624j. URL http://dx.doi.org/10.1021/nl080624j.

[22] V. C. Holmberg, K. A. Collier, and B. A. Korgel. Real-Time observation of impurity diffusion in silicon nanowires. *Nano Letters*, 11(9):3803–3808, 09 2011. doi: 10.1021/nl201879u. URL http://dx.doi.org/10.1021/nl201879u.

[23] Y. C. Lin, Y. Chen, and Y. Huang. The growth and applications of silicides for nanoscale devices. *Nanoscale*, 4(5):1412–1421, 2012. doi: 10.1039/C1NR10847F. URL http://dx.doi.org/10.1039/C1NR10847F.

[24] Y. E. Yaish, A. Katsman, G. M. Cohen, and M. Beregovsky. Kinetics of nickel silicide growth in silicon nanowires: From linear to square root growth. *Journal of Applied Physics*, 109(9):094303, 2011. doi: http://dx.doi.org/10.1063/1.3574650. URL http://scitation.aip.org/content/aip/journal/jap/109/9/10.1063/1.3574650.

[25] K. Ogata, E. Sutter, X. Zhu, and S. Hofmann. Ni-silicide growth kinetics in Si and Si/SiO_2 core/shell nanowires. *Nanotechnology*, 22(36):365305, 2011. URL http://stacks.iop.org/0957-4484/22/i=36/a=365305.

[26] Y. T. Wu, C. W. Huang, C. H. Chiu, C. F. Chang, J. Y. Chen, T. Y. Lin, Y. T. Huang, K. C. Lu, P. H. Yeh, and W. W. Wu. Nickel/Platinum dual silicide axial nanowire heterostructures with excellent photosensor applications. *Nano Letters*, 16(2):1086–1091, 02 2016. doi: 10.1021/acs.nanolett.5b04309. URL http://dx.doi.org/10.1021/acs.nanolett.5b04309.

[27] K. C. Lu, W. W. Wu, H. Ouyang, Y. C. Lin, Y. Huang, C. W. Wang, Z. W. Wu, C. W. Huang, L. J. Chen, and K. N. Tu. The influence of surface oxide on the growth of metal/semiconductor nanowires. *Nano Letters*, 11(7):2753–2758, 07 2011. doi: 10.1021/nl201037m. URL http://dx.doi.org/10.1021/nl201037m.

[28] N. S. Dellas. *Silicide and germanide contacts to silicon and germanium nanowires*. PhD thesis, The Pennsylvania State University, May 2011.

[29] C. H. Chiu, C. W. Huang, J. Y. Chen, Y. T. Huang, J. C. Hu, L. T. Chen, C. L. Hsin, and W. W. Wu. Copper silicide/silicon nanowire heterostructures: in situ TEM observation of growth behaviors and electron transport properties. *Nanoscale*, 5:5086–5092, 2013. doi: 10.1039/C3NR33302G. URL http://dx.doi.org/10.1039/C3NR33302G.

[30] S. C. Hsu, C. L. Hsin, C. W. Huang, S. Y. Yu, C. W. Wang, C. M. Lu, K. C. Lu, and W. W. Wu. Single-crystalline Ge nanowires and Cu_3Ge/Ge nano-heterostructures. *CrystEngComm*, 14:4570–4574, 2012. doi: 10.1039/C2CE25316J. URL http://dx.doi.org/10.1039/C2CE25316J.

[31] K. C. Lu, W. W. Wu, H. W. Wu, C. M. Tanner, J. P. Chang, L. J. Chen, and K. N. Tu. In situ control of atomic-scale Si layer with huge strain in the nanoheterostructure NiSi/Si/NiSi through point contact reaction. *Nano Letters*, 7(8):2389–2394, 08 2007. doi: 10.1021/nl071046u. URL http://dx.doi.org/10.1021/nl071046u.

[32] Y. Chen, Y. C. Lin, X. Zhong, H. C. Cheng, X. Duan, and Y. Huang. Kinetic manipulation of silicide phase formation in Si nanowire templates. *Nano Letters*, 13(8):3703–3708, 08 2013. doi: 10.1021/nl401593f. URL http://dx.doi.org/10.1021/nl401593f.

[33] H. Okino, I. Matsuda, R. Hobara, Y. Hosomura, S. Hasegawa, and P. A. Bennett. In situ resistance measurements of epitaxial cobalt silicide nanowires on Si (110). *Applied physics letters*, 86(23):233108–233108, 2005.

[34] T. Burchhart, A. Lugstein, Y. J. Hyun, G. Hochleitner, and E. Bertagnolli. Atomic scale alignment of copper-germanide contacts for Ge nanowire metal oxide field effect transistors. *Nano Letters*, 9(11):3739–3742, 11 2009. doi: 10.1021/nl9019243. URL http://dx.doi.org/10.1021/nl9019243.

[35] Y. Wu, J. Xiang, C. Yang, W. Lu, and C. M. Lieber. Single-crystal metallic nanowires and metal/semiconductor nanowire heterostructures. *Nature*, 430(6995):61–65, 07 2004. URL http://dx.doi.org/10.1038/nature02674.

[36] J. L. Lensch-Falk, E. R. Hemesath, and L. J. Lauhon. Syntaxial growth of Ge/Mn-Germanide nanowire heterostructures. *Nano Letters*, 8(9):2669–2673, 09 2008. doi: 10.1021/nl800933s. URL http://dx.doi.org/10.1021/nl800933s.

[37] J. Tang, C. Y. Wang, M. H. Hung, X. Jiang, L. T. Chang, L. He, P. H. Liu, H. J. Yang, H. Y. Tuan, L. J. Chen, and K. L. Wang. Ferromagnetic germanide in Ge nanowire transistors for spintronics application. *ACS Nano*, 6(6):5710–5717, 06 2012. doi: 10.1021/nn301956m. URL http://dx.doi.org/10.1021/nn301956m.

[38] Y. C. Lin, K. C. Lu, W. W. Wu, J. Bai, L. J. Chen, K. N. Tu, and Y. Huang. Single crystalline PtSi nanowires, PtSi/Si/PtSi nanowire heterostructures, and nanodevices. *Nano Letters*, 8(3):913–918, 03 2008. doi: 10.1021/nl073279r. URL http://dx.doi.org/10.1021/nl073279r.

[39] M. Tinani, A. Mueller, Y. Gao, E. A. Irene, Y. Z. Hu, and S. P. Tay. In situ real-time studies of nickel silicide phase formation. *Journal of Vacuum Science & Technology B*, 19(2):(376–383), 2001. doi: http://dx.doi.org/10.1116/1.1347046. URL http://scitation.aip.org/content/avs/journal/jvstb/19/2/10.1116/1.1347046.

[40] F. d'Heurle L. Miglio. Silicides : Fundamentals and applications. *World Scientific, 18 dec.*, 2000.

[41] W. Tang, B. M. Nguyen, R. Chen, and S. A. Dayeh. Solid-state reaction of nickel silicide and germanide contacts to semiconductor nanochannels. *Semiconductor Science and Technology*, 29(5):054004, 2014. URL http://stacks.iop.org/0268-1242/29/i=5/a=054004.

[42] S. M. Sze. *Semiconductor Devices - Physics and Technology*. Wiley, 1985.

[43] W. Tang, S. A. Dayeh, S. T. Picraux, J. Y. Huang, and K. N. Tu. Ultrashort channel silicon nanowire transistors with nickel silicide Source/Drain contacts. *Nano Letters*, 12(8):3979–3985, 08 2012. doi: 10.1021/nl3011676. URL http://dx.doi.org/10.1021/nl3011676.

[44] O. C. F. Aviles and A. I. Oliva. Physical properties of Au and Al thin films measured by resistive heating. *Surface Review and Letter*, 12:101–106, January 2005.

[45] Y. Maeda, N. Tsukamoto, Y. Yazawa, Y. Kanemitsu, and Y. Masumoto. Visible photoluminescence of Ge microcrystals embedded in SiO_2 glassy matrices. *Applied Physics Letters*, 59(24):(3168–3170), 1991. doi: http://dx.doi.org/10.1063/1.105773. URL http://scitation.aip.org/content/aip/journal/apl/59/24/10.1063/1.105773.

[46] H. Bracht. Copper related diffusion phenomena in germanium and silicon. *Materials science in semiconductor processing*, 7(3):113–124, 2004.

[47] R. N. Hall and J. H. Racette. Diffusion and solubility of copper in extrinsic and intrinsic germanium, silicon, and gallium arsenide. *Journal of Applied Physics*, 35(2):(379–397), 1964. doi: http://dx.doi.org/10.1063/1.1713322. URL http://scitation.aip.org/content/aip/journal/jap/35/2/10.1063/1.1713322.

[48] J. C. Severiens and C. S. Fuller. Mobility of impurity ions in germanium and silicon. *Phys. Rev.*, 92:1322–1323, Dec 1953. doi: 10.1103/PhysRev.92.1322. URL http://link.aps.org/doi/10.1103/PhysRev.92.1322.

[49] F. C. Frank and D. Turnbull. Mechanism of diffusion of copper in germanium. *Phys. Rev.*, 104:617–618, Nov 1956. doi: 10.1103/PhysRev.104.617. URL http://link.aps.org/doi/10.1103/PhysRev.104.617.

[50] H. M. Tawancy and M. O. Aboelfotoh. Effect of phase transitions in copper-germanium thin film alloys on their electrical resistivity. *Journal of Materials Science*, 30(23):6053–6064, 1995. doi: 10.1007/BF01151527. URL http://dx.doi.org/10.1007/BF01151527.

[51] A. Aubin. Analyse de la formation des phases du système cuivre-germanium par diffraction des rayons x sur des échantillons d'épaisseur nanoscopique. Master's thesis, Université de Montréal, Decembre 2013.

[52] F. M. d'Heurle and J. Gupta. Phase formations in the copper-germanium system: Reactions, structures and resistivities. *Applied Surface Science*, 73:(214 – 224), 1993. ISSN 0169-4332. doi: http://dx.doi.org/10.1016/0169-4332(93)90169-C. URL http://www.sciencedirect.com/science/article/pii/016943329390169C.

[53] M. Fritze, C. L. Chen, S. Calawa, D. Yost, B. Wheeler, P. Wyatt, C. L. Keast, J. Snyder, and J. Larson. High-speed Schottky-barrier pMOSFET with fT=280 GHz. *IEEE Electron Device Letters*, 25(4):220–222, April 2004. ISSN 0741-3106. doi: 10.1109/LED.2004.826294.

[54] J. Kedzierski, P. Xuan, E. H. Anderson, J. Bokor, Tsu-Jae King, and Chenming Hu. Complementary silicide source/drain thin-body MOSFETs for the 20 nm gate length regime. In *Electron Devices Meeting, 2000. IEDM '00. Technical Digest. International*, pages 57–60, Dec 2000. doi: 10.1109/IEDM.2000.904258.

[55] J. M. Larson and J. P. Snyder. Overview and status of metal S/D Schottky-barrier MOSFET technology. *IEEE Transactions on Electron Devices*, 53(5):1048–1058, May 2006. ISSN 0018-9383. doi: 10.1109/TED.2006.871842.

[56] H. Mehrer. *Diffusion in Solids*, volume 155. Springer-Verlag Berlin Heidelberg, 2007.

[57] B. E. Deal and A. S. Grove. General relationship for the thermal oxidation of silicon. *Journal of Applied Physics*, 36(12):3770–3778, 1965. doi: http://dx.doi.org/10.1063/1.1713945. URL http://scitation.aip.org/content/aip/journal/jap/36/12/10.1063/1.1713945.

[58] F. Nemouchi, D. Mangelinck, C. Bergman, P. Gas, and U. Smith. Differential scanning calorimetry analysis of the linear parabolic growth of nanometric Ni silicide thin films on a Si substrate. *Applied Physics Letters*, 86(4):041903, 2005. doi: http://dx.doi.org/10.1063/1.1852727. URL http://scitation.aip.org/content/aip/journal/apl/86/4/10.1063/1.1852727.

[59] Y. Chen, Y. C. Lin, C. W. Huang, C. W. Wang, L. J. Chen, W. W. Wu, and Y. Huang. Kinetic competition model and size-dependent phase selection in 1-D nanostructures. *Nano Letters*, 12(6):3115–3120, 06 2012. doi: 10.1021/nl300990q. URL http://dx.doi.org/10.1021/nl300990q.

[60] J. Appenzeller, J. Knoch, E. Tutuc, M. Reuter, and S. Guha. *Dual-gate silicon nanowire transistors with nickel silicide contacts*. International Electron Devices Meeting Technical Digest, 2006. ISBN 1424404398. doi: 10.1109/IEDM.2006.346842.

[61] A. Katsman, Y. Yaish, E. Rabkin, and M. Beregovsky. Surface diffusion controlled formation of nickel silicides in silicon nanowires. *Journal of Electronic Materials*, 39(4):365–370, 2010. doi: 10.1007/s11664-009-1071-1. URL http://dx.doi.org/10.1007/s11664-009-1071-1.

[62] R. S. Wagner and W. C. Ellis. Vapor-liquid-solid mechanism of single crystal growth. *Applied Physics Letters*, 4(5):89–90, 1964. doi: http://dx.doi.org/10.1063/1.1753975. URL http://scitation.aip.org/content/aip/journal/apl/4/5/10.1063/1.1753975.

[63] M. I. den Hertog, F. González-Posada, R. Songmuang, J. L. Rouviere, T. Fournier, B. Fernandez, and E. Monroy. Correlation of polarity and crystal structure with

optoelectronic and transport properties of GaN/AlN/GaN nanowire sensors. *Nano Letters*, 12(11):5691–5696, 11 2012. doi: 10.1021/nl302890f. URL http://dx.doi.org/10.1021/nl302890f.

[64] D. B. Williams and C. B. Carter. *Transmission Electron Microscopy*. Springer US, 2009.

[65] M. den Hertog. *Caractérisation de Nanofils de Silicium par Microscopie Electronique en Transmission*. PhD thesis, Ecole doctorale de physique - Université Joseph Fourier, Mai 2009.

[66] N. Stoddard, G. Duscher, W. Windl, and G. Rozgonyi. A new understanding of near-threshold damage for 200 keV irradiation in silicon. *Journal of Materials Science*, 40(14):3639–3650, 2005. doi: 10.1007/s10853-005-1059-z. URL http://dx.doi.org/10.1007/s10853-005-1059-z.

[67] D. Cooper, N. Bernier, and J. L. Rouviere. Combining 2 nm spatial resolution and 0.02% precision for deformation mapping of semiconductor specimens in a transmission electron microscope by precession electron diffraction. *Nano letters*, 15(8):5289–5294, 2015.

[68] D. Cooper, N. Bernier, and J.L. Rouviere. Field mapping of semiconductor devices in a transmission electron microscope with nanometre scale resolution by off-axis electron holography and precession electron diffraction. pages 777–780, 2015.

[69] J. E. Wood, D. B. Williams, and J. I. Goldstein. Experimental and theoretical determination of k_{AFe} factors for quantitative X-ray microanalysis in the analytical electron microscope. *Journal of Microscopy*, 133(3):255–274, 1984. doi: 10.1111/j.1365-2818.1984.tb00490.x. URL http://dx.doi.org/10.1111/j.1365-2818.1984.tb00490.x.

[70] P. J. Sheridan. Determination of experimental and theoretical k_{ASi} factors for a 200kV analytical electron microscope. *Journal of Electron Microscopy Technique*, 11(1):41–61, 1989. doi: 10.1002/jemt.1060110107. URL http://dx.doi.org/10.1002/jemt.1060110107.

[71] J. I. Goldstein, J. L. Costley, G. W. Lorimer, and Reed. R. J. B. Quantitative X-ray analysis in the electron microscope. *Scanning Electron Microscopy*, 1:315–324, 1977.

[72] P. Burdet, Z. Saghi, A. N. Filippin, A. Borrás, and P. A. Midgley. A novel 3D absorption correction method for quantitative EDX-STEM tomography. *Ultramicroscopy*, 160:118–129, 1 2016. doi: http://dx.doi.org/10.1016/j.ultramic.2015.09.012. URL //www.sciencedirect.com/science/article/pii/S0304399115300358.

[73] M. Watanabe and D. B. Willams. The quantitative analysis of thin specimens: a review of progress from the Cliff-Lorimer to the new zeta-factor methods. *Journal of Microscopy*, 221(2):89–109, 2006. ISSN 1365-2818. doi: 10.1111/j.1365-2818.2006.01549.x. URL http://dx.doi.org/10.1111/j.1365-2818.2006.01549.x.

[74] P. Rueda-Fonseca, E. Robin, E. Bellet-Amalric, M. Lopez-Haro, M. Den Hertog, Y. Genuist, R. André, A. Artioli, S. Tatarenko, D. Ferrand, and J. Cibert. Quantitative reconstructions of 3D chemical nanostructures in nanowires. *Nano Letters*, 16(3):1637–1642, 03 2016. doi: 10.1021/acs.nanolett.5b04489. URL http://dx.doi.org/10.1021/acs.nanolett.5b04489.

[75] M. Mongillo. *Transport properties and functional devices on CVD grown Silicon nanowires*. PhD thesis, Universite de Grenoble, 2010.

[76] M. Duchamp, Q. Xu, and R. E. Dunin-Borkowski. Convenient preparation of high-quality specimens for annealing experiments in the transmission electron microscope. *Microscopy and Microanalysis*, 20(06):1638–1645, 2014.

[77] L. Palatinus. PETS - program for analysis of electron diffraction data. *Institute of Physics, Prague, Czech*, 2011.

[78] https://www.comsol.fr/comsol-multiphysics. URL https://www.comsol.fr/comsol-multiphysics.

[79] M. C. Wingert, Z. C. Y. Chen, S. Kwon, J. Xiang, and R. Chen. Ultra-sensitive thermal conductance measurement of one-dimensional nanostructures enhanced by differential bridge. *Review of Scientific Instruments*, 83(2):024901, 2012. doi: http://dx.doi.org/10.1063/1.3681255. URL http://scitation.aip.org/content/aip/journal/rsi/83/2/10.1063/1.3681255.

[80] H. Ftouni, C. Blanc, D. Tainoff, A. D. Fefferman, M. Defoort, K. J. Lulla, J. Richard, E. Collin, and O. Bourgeois. Thermal conductivity of silicon nitride membranes is not sensitive to stress. *Physical Review B*, 92(12):125439–, 09 2015. URL http://link.aps.org/doi/10.1103/PhysRevB.92.125439.

[81] H. J. Yang and H. Y. Tuan. High-yield, high-throughput synthesis of germanium nanowires by metal-organic chemical vapor deposition and their functionalization and applications. *J. Mater. Chem.*, 22:2215–2225, 2012. doi: 10.1039/C1JM14875C. URL http://dx.doi.org/10.1039/C1JM14875C.

[82] Y. Hanaoka, K. Hinode, K. Takeda, and D. Kodama. Increase in electrical resistivity of copper and aluminum fine lines. *Materials Transactions*, 43(7):1621 – 1623, 2002.

[83] J. G. M. Becht, F. J. J. van Loo, and R. Metselaar. The solid state diffusion reaction of copper with germanium; a comparison between silicon and germanium. *Reactivity of Solids*, 6(1):61–73, 1988. doi: http://dx.doi.org/10.1016/0168-7336(88)80046-9. URL http://www.sciencedirect.com/science/article/pii/0168733688800469.

[84] M. Werner, H. Mehrer, and H. D. Hochheimer. Effect of hydrostatic pressure, temperature, and doping on self-diffusion in germanium. *Phys. Rev. B*, 32: 3930–3937, Sep 1985. doi: 10.1103/PhysRevB.32.3930. URL http://link.aps.org/doi/10.1103/PhysRevB.32.3930.

[85] A. Kuper, H. Letaw, L. Slifkin, E. Sonder, and C. T. Tomizuka. Self-diffusion in copper. *Phys. Rev.*, 96:1224–1225, Dec 1954. doi: 10.1103/PhysRev.96.1224. URL http://link.aps.org/doi/10.1103/PhysRev.96.1224.

[86] Y. C. Chou, W. W. Wu, C. Y. Lee, C. Y. Liu, L. J. Chen, and K. N. Tu. Heterogeneous and homogeneous nucleation of epitaxial $NiSi_2$ in [110] Si nanowires. *The Journal of Physical Chemistry C*, 115(2):397–401, 01 2011. doi: 10.1021/jp108686y. URL http://dx.doi.org/10.1021/jp108686y.

[87] J. D'Ans, E. Lax, and R. Blachnik. *Taschenbuch für Chemiker und Physiker/D'Ans*. Springer: Berlin Heidelberg, 1998.

[88] C. Y. Nam, D. Tham, and J. E. Fischer. Disorder effects in Focused-Ion-Beam-Deposited Pt contacts on GaN nanowires. *Nano Letters*, 5(10):2029–2033, 10 2005. doi: 10.1021/nl0515697. URL http://dx.doi.org/10.1021/nl0515697.

[89] A. Thanailakis and D. C. Northrop. Metal-germanium Schottky barriers. *Solid-State Electronics*, 16(12):1383–1389, 1973. doi: http://dx.doi.org/10.1016/0038-1101(73)90052-X. URL http://www.sciencedirect.com/science/article/pii/003811017390052X.

[90] T. Nishimura, K. Kita, and A. Toriumi. Evidence for strong Fermi-level pinning due to metal-induced gap states at metal/germanium interface. *Applied Physics Letters*, 91(12):123123, 2016/12/15 2007. doi: 10.1063/1.2789701. URL http://aip.scitation.org/doi/abs/10.1063/1.2789701.

[91] T. Hanrath and B. A. Korgel. Influence of surface states on electron transport through intrinsic Ge nanowires. *The Journal of Physical Chemistry B*, 109(12): 5518–5524, 03 2005. doi: 10.1021/jp044491b. URL http://dx.doi.org/10.1021/jp044491b.

[92] S. Zhang, E. R. Hemesath, D. E. Perea, E. Wijaya, J. L. Lensch-Falk, and L. J. Lauhon. Relative influence of surface states and bulk impurities on the electrical properties of Ge nanowires. *Nano Letters*, 9(9):3268–3274, 09 2009. doi: 10.1021/nl901548u. URL http://dx.doi.org/10.1021/nl901548u.

[93] J. D. Cutnell and K. W. Johnson. *Physics 3rd Edition*. New York: John Wiley & Sons Inc., 1995.

[94] C. Durkan and M. E. Welland. Size effects in the electrical resistivity of polycrystalline nanowires. *Phys. Rev. B*, 61:14215–14218, May 2000. doi: 10.1103/PhysRevB.61.14215. URL http://link.aps.org/doi/10.1103/PhysRevB.61.14215.

[95] E. Kirkendall. Diffusion of zinc in alpha brass. *Trans AIME*, 147:104–110, 1942.

[96] F. M. Brunbauer, E. Bertagnolli, and A. Lugstein. Gate -Tunable electron transport phenomena in Al–Ge(111)–Al nanowire heterostructures. *Nano Letters*, 15(11):7514–7518, 11 2015. doi: 10.1021/acs.nanolett.5b03169. URL http://dx.doi.org/10.1021/acs.nanolett.5b03169.

[97] V. T. Serebryanskii and V. A. Epel'baum. Phase diagram of the Aluminum-Boron system. *Journal of Structural Chemistry*, 2(6):692–694, 1961.

[98] Anon. Itrs international technology roadmap for semiconductors. 2015.

[99] V. V. Eremenko P. N. Chubov and Y. A. Pilipenko. Dependence of the critical temperature and energy gap on the thickness of superconducting Aluminum films. *SOVIET PHYSICS JETP*, 28(3):389–395, March 1969.

[100] A. A. Shanenko, M. D. Croitoru, M. Zgirski, F. M. Peeters, and K. Arutyunov. Size-dependent enhancement of superconductivity in Al and Sn nanowires:

Shape-resonance effect. *Phys. Rev. B*, 74:052502, Aug 2006. doi: 10.1103/PhysRevB.74.052502. URL http://link.aps.org/doi/10.1103/PhysRevB.74.052502.